

École doctorale n° 364 : Sciences Fondamentales et Appliquées

Doctorat ParisTech

THÈSE

pour obtenir le grade de docteur délivré par

l'École Nationale Supérieure des Mines de Paris

Spécialité doctorale “Science et Génie des Matériaux”

présentée et soutenue publiquement par

Ali SAAD

le xx septembre 2015

NUMERICAL MODELLING OF MACROSEGREGATION FORMED DURING SOLIDIFICATION WITH SHRINKAGE USING A LEVEL SET APPROACH

Directeurs de thèse: **Michel BELLET**
Charles-André GANDIN

Jury

M. Blablabla,	Professeur, MINES ParisTech	Rapporteur
M. Blablabla,	Professeur, Arts Et Métiers ParisTech	Rapporteur
M. Blablabla,	Chargé de recherche, ENS Cachan	Examinateur
M. Blablabla,	Danseuse, en freelance	Examinateur
M. Blablabla,	Ingénieur, MIT	Examinateur

T
H
E
S
S
E

MINES ParisTech
Centre de Mise en Forme des Matériaux (CEMEF)
UMR CNRS 7635, F-06904 Sophia Antipolis, France

Acknowledgement

Dedicated to humanity ...

Contents

1 General Introduction	1
1.1 Solidification notions	2
1.1.1 Solute partitioning	2
1.1.2 Dendritic growth	4
1.1.3 Mush permeability	6
1.2 Macrosegregation	7
1.2.1 Liquid thermosolutal convection	8
1.2.2 Solidification shrinkage	9
1.2.3 Movement of equiaxed grains	9
1.2.4 Solid deformation	9
1.3 Other defects	9
1.4 Industrial Worries	11
1.5 Project context and objectives	12
1.5.1 Context	12
1.5.2 Objectives and outline	14
2 Energy balance with thermodynamic tabulations	19
2.1 State of the art	20
2.2 Thermodynamic considerations	21
2.2.1 Volume averaging	21
2.2.2 The temperature-enthalpy relationship	22
2.2.3 Tabulation of properties	22
2.3 Numerical method	24
2.3.1 Enthalpy-based approach	28
2.3.2 Temperature-based approach	28
2.3.3 Convergence	29
2.4 Validation	30
2.5 Application: multicomponent alloy solidification	33

Contents

2.5.1	Tabulations	35
2.5.2	Discussion	37
2.6	Limitations	42
3	Macrosegregation with liquid metal motion	45
3.1	Introduction	47
3.2	Formulation stability	47
3.2.1	Stable mixed finite elements	47
3.2.2	Variational multiscale (VMS)	48
3.3	Navier-Stokes solver	49
3.3.1	Strong and weak formulations	49
3.3.2	Stabilisation parameters	53
3.3.3	Implementation	54
3.4	Application to multicomponent alloys	55
3.4.1	<i>Tsolver</i> validation with fluid flow	55
3.4.2	Results	58
3.5	Macroscopic prediction of channel segregates	63
3.5.1	Introduction	63
3.5.2	Experimental work	64
3.5.3	Macroscopic scale simulations	64
3.6	Meso-Macro prediction of channel segregates	74
3.6.1	Numerical method	74
3.6.2	Configuration	75
3.6.3	Effect of vertical temperature gradient	79
3.6.4	Effect of cooling rate	81
3.6.5	Effect of lateral temperature gradient	83
3.6.6	Mono-grain freckles	84
Bibliography		87

List of Acronyms

Acronym	Standing for
ALE	Arbitrary Lagrangian-Eulerian
BTR	Brittle temperature range
CAFD	Cellular Automata Finite Difference
CAFE	Cellular Automata Finite Element
CBB	Circumventing Babuška-Brezzi
CCEMLCC	Chill Cooling for the Electro-Magnetic Levitator in relation with Continuous Casting of steel
CEMEF	Centre de Mise en Forme des Matériaux
CFL	Courant–Friedrichs–Lewy
C.FL	Computing and FLuids
CSF	Continuum Surface Force
DLR	Deutsches Zentrum für Luft- und Raumfahrt
DSPG	Darcy-Stabilising/Petrov-Galerkin
EML	Electromagnetic levitation
ESA	European Space Agency
FEM	Finite Element Method
FVM	Finite Volume Method
GMAW	Gas Metal Arc Welding
ISS	International Space Station
IWT	Institut für Werkstofftechnik
LHS	Left-hand side
LSIC	Least squares on incompressibility constraint
LSM	Level set method
MAC	Marker-and-cell
PF	Phase field
PSPG	Pressure-Stabilising/Petrov-Galerkin
RHS	Right-hand side
RUB	Ruhr Universität Bochum
RVE	Representative Elementary Volume
SBB	Satisfying Babuška-Brezzi
SUPG	Streamline-Upwind/Petrov-Galerkin
VMS	Variational MultiScale
VOF	Volume Of Fluid

Contents

Chapter 1

General Introduction

Casting is one of the earliest production techniques created by human civilisation since the Bronze Age, dated to circa 5000 years ago. From ancient swords to nowadays Swiss Army Knives, the need for alloys has never decreased. The key phenomenon behind this technique is solidification, or the transformation of matter from liquid to solid state. With this phase change, many phenomena, not visible to the naked eye, take place with a very complex interaction, in order to form a solid. However, the combination of heat transfer (e.g. release of latent heat) and mass transfer (e.g. redistribution of chemical elements and phases), often lead to defects. *Segregation* is type of defect which can lead to uncontrolled properties of cast parts. The Latin origin of this word, *segregatus*, has the social meaning of "separating a group from the dominant majority", while in metallurgy it means a non uniform distribution of chemical species. Depending on the scale, we may speak of *microsegregation* when the heterogeneity spans some few hundred microns, whereas the term *macrosegregation* refers to a much coarser length scale, ranging from some millimetres to some meters! The solidified structure has intrinsic thermophysical and thermomechanical properties directly influenced by the segregation pattern.

In casting processes, such as continuous casting ([fig. 1.7](#)) and ingot casting, it is crucial to apprehend the intricate phenomena leading to macrosegregation. Its influence on intermediate processing steps (e.g. forging, coating, welding,...) to reach a manufactured product, also needs to be understood. In this introductory chapter, we give a quick overview of solidification phenomena and microstructure, then present the factors which promote segregation, on both microscopic and macroscopic scales. Aside from macrosegregation, other defects are also briefly presented.

In a continuous casting process ([fig. 1.1a](#)), the partially solidified slab is carried through a series of rolls that exert contact forces to straighten it. When a slab enters through

Chapter 1. General Introduction

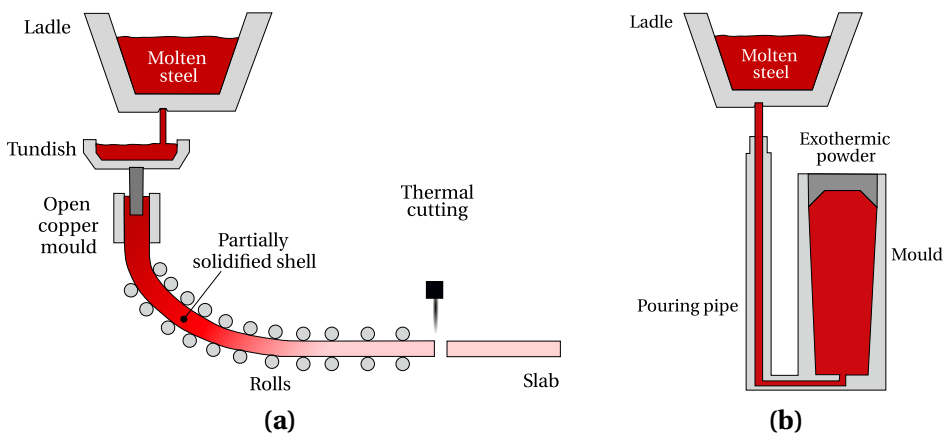


Fig. 1.1 – Schematics of the main steelmaking processes by (a) continuous casting and (b) ingot casting.

these rolls after exiting the open copper mold, it consists of a thin solid shell made of a mixture of solid and liquid phases known as the mushy zone, whose core is still fully liquid. as the slab edges solidify earlier than the centre, the enriched liquid accumulates halfway in thickness, forming a centreline macrosegregation as shown in fig. 1.2.

Other types of segregation patterns can be encountered while casting heavy ingots, as schematised in ??:

- a negative segregation cone promoted by the sedimentation of equiaxed crystals and settling of dendrite fragments, often seen at the bottom part of the ingot,
- positive segregation channels, known as A-segregates, form along the columnar dendritic zones, close to the vertical contact with the mould,
- positive V-segregates can be identified in the centre of the ingot,
- a positive "hot-top" macrosegregation in the upper zone where the last rich liquid solidifies, caused by thermosolutal buoyancy forces.

Combeau et al. [2009] state that A-segregates and V-segregates formation is mainly attributed to local flow phenomena. As such, their scale is finer than macrosegregation, hence called "mesosegregates".

1.1 Solidification notions

1.1.1 Solute partitioning

The simplest definition of this phenomenon is an uneven distribution of solute between the liquid and the growing solid, at the microscopic scale of the interface sep-

1.1. Solidification notions

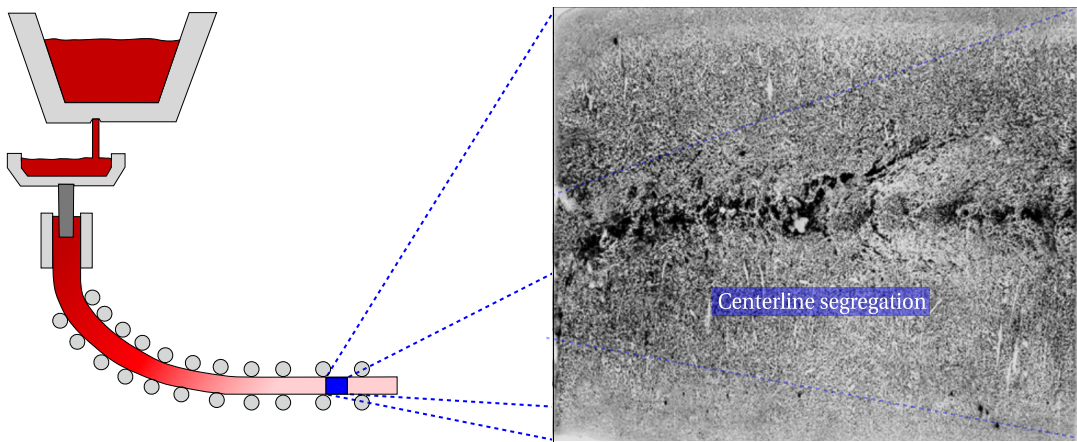


Fig. 1.2 – Zoom on a sulphur print of a continuously cast high carbon steel billet at a longitudinal section, showing high positive centreline segregation [Choudhary and Ganguly 2007].

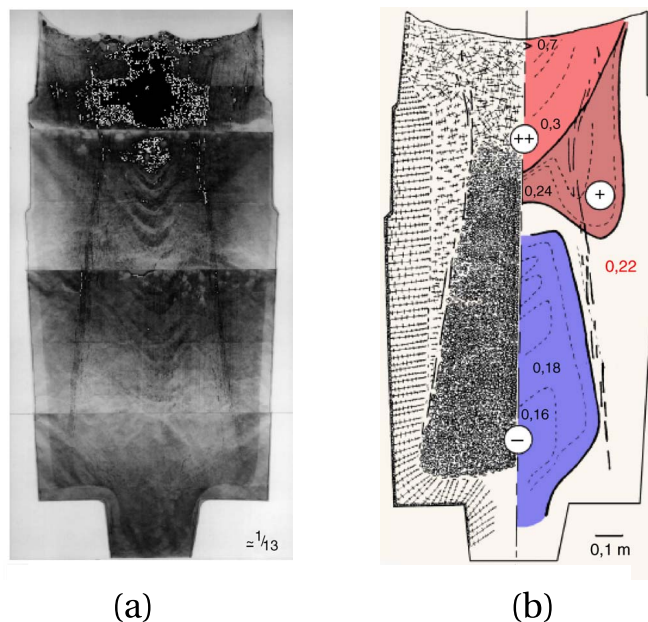


Fig. 1.3 – (a) Sulphur print of a 65-ton steel ingot showing (b) various macrosegregation patterns and levels as well as solidification structures [Lesoult 2005].

Chapter 1. General Introduction

arating these phases. If we consider a binary alloy, then the solubility limit is the key factor that dictates the composition at which a primary solid phase exists at equilibrium. The segregation (or partition) coefficient k determines the extent of solute rejection into the liquid during solidification:

$$k = \frac{w^{s^*}}{w^{l^*}} \quad (1.1)$$

where w^{s^*} and w^{l^*} are the solute compositions at the interface, of the solid and liquid phases respectively. When the segregation coefficient is less than unity (such is the case for most alloys during dendritic solidification), the first solid forms at the liquidus temperature, T_L , with a composition $w^{s^*} = kw^{l^*}$ less than the surrounding liquid composition, the latter being initially at the nominal composition, w_0 . [Figure 1.4](#) illustrates a typical binary phase diagram where the real solidus and liquidus are represented by solid lines, while the possible linear approximations are in grey dashed lines. For most binary alloys, this linearisation simplifies derivation of microsegregation models, as k becomes independent of temperature.

For each phase, the relationship between the composition at the interface and that in the bulk depends on the chemical homogenisation of the phase by solute transport. The more homogeneous a phase, the closer the concentrations between the interface and the bulk, hence closer to equilibrium. It is thus essential to study the effect of homogenisation on the segregation behaviour and the subsequent effect on solidification, which is seen by a non-uniform composition through the cast product on a microscopic scale, better known as microsegregation. This phenomenon is essential in a casting process inasmuch as it affects the microstructure and grain morphology, hence the final mechanical properties of the alloy.

1.1.2 Dendritic growth

In a casting process, the vicinity of the chill surface where the contact between the molten alloy and the cold moulds, is the first area to solidify. Thermal gradient, \vec{G} , and cooling rate, R_c , are two crucial process parameters that define the solid-liquid interface velocity, v^* , which in turn affects the initial microstructure. Although it may not be easy to control them, their role in solidification is well established.

The solid-liquid interface fluctuates when solidifying, thus perturbations may appear on the front, locally destabilizing it. Two outcome scenarios are possible. The first scenario is characterized by low values of v^* where the interface maintains a planar shape, hence we speak of *planar growth*. With this kind of growth, a random protuberance

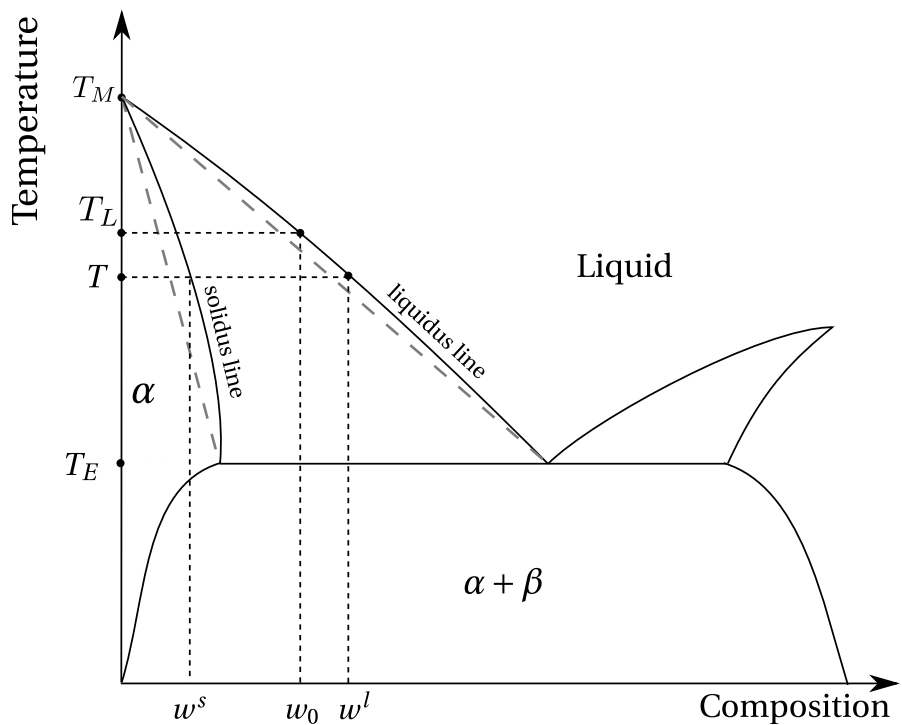


Fig. 1.4 – Typical eutectic phase diagram of a binary alloy showing the real solidus and liquidus at full equilibrium, with the corresponding linear approximations (grey dashed lines). T_M and T_E are respectively the melting point of the solvent and the eutectic temperature.

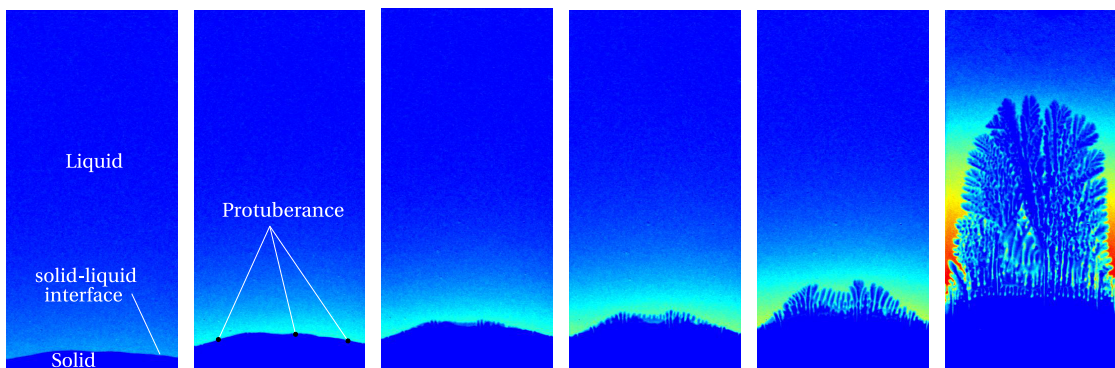


Fig. 1.5 – Time evolution of a solidifying Al-4 wt.% Cu sample, showing interface destabilisation and subsequent dendritic solidification [Buffet et al. 2010]. The liquid far from the interface and having a blue color is at nominal composition, while the one near the dendritic structure with the yellow and red colors, is richer in solute.

appearing at the interface, has a low tip velocity (low driving force of solidification). As such, the rest of the interface catches up, maintaining the planar geometry. In another scenario more representative of a real casting, the interface velocity leads to its instability. The protuberance tip will grow into a liquid less rich in solute, as shown in the time frames of [fig. 1.5](#). The zone ahead of the solid-liquid interface is constitutionally undercooled, giving a greater driving force for the protuberance to grow in the direction of the thermal gradient. An expression for the critical velocity is given by [Tiller et al. \[1953\]](#). As the solid-liquid interface adopts a tree-like shape, we speak of *dendritic growth*. Near the chill surface, dendrites are columnar, with a favourable growth in the $<100>$ direction for alloys with cubic lattices, but different orientations are also reported in the literature [see [Dantzig and Rappaz 2009](#), p. 289].

Far from mould walls, a similar dendritic growth phenomenon occurs where temperature is uniform, but with an equiaxed morphology. [Figure 1.6](#) shows both columnar and equiaxed morphologies. Columnar dendrites are characterised by a primary spacing, λ_1 , between the main trunks, and a secondary spacing, λ_2 , for the arms that are perpendicular to the trunks. It should be noted that λ_1 and λ_2 , together with the grain size, are three important microstructural parameters in the as-cast microstructure [[Easton et al. 2011](#)]. Further branching may occur but will not be discussed here.

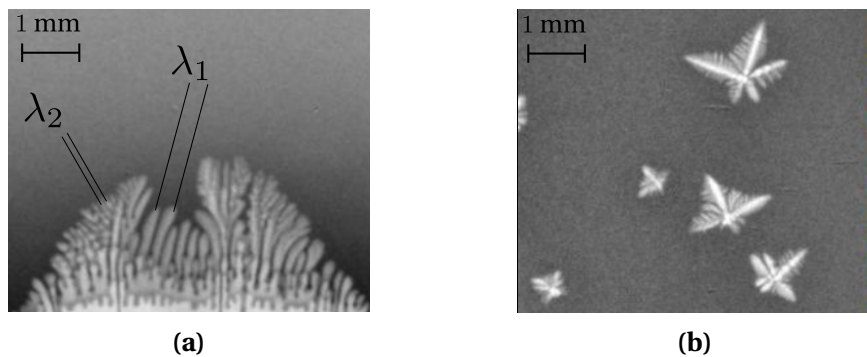


Fig. 1.6 – In situ observation by X-ray radiography of the (a) columnar microstructure for Al-4 wt.% Cu alloy [[Buffet et al. 2010](#)] and (b) equiaxed microstructure during solidification of Al-10 wt.% Cu alloy [[Bogno et al. 2013](#)].

1.1.3 Mush permeability

The dendritic geometry is crucial in solidification theory as it exhibits lower solid fraction compared to a microstructure formed by planar growth. This fact has consequences on the fluid-structure interaction in the mushy zone, namely the liquid flow through dendrites. At the chill surface, the solid grows gradually from dispersed growing nuclei to a permeable solid skeleton, until grains have fully grown at the end of

phase change. In the intermediate state, the liquid flow in and out of the mushy zone through the network of dendrites is a key phenomenon from various perspectives, especially the rheological perspective. The flow through the interdendritic liquid is damped by primary trunks and secondary dendrite arms, resulting in momentum dissipation just like in saturated porous media. The famous [Darcy \[1856\]](#) law relates the pressure gradient ($\vec{\nabla}p$) to the fluid velocity \vec{v} (assuming the solid phase is fixed), through the following equation [[Rappaz et al. 2003](#)]:

$$\vec{v} = \frac{\mathbb{K}}{\mu^l} \vec{\nabla}p \quad (1.2)$$

where μ^l is the liquid dynamic viscosity and \mathbb{K} is the permeability tensor. The latter parameter has been the subject of numerous studies that aimed to predict it from various microstructural or morphological parameters. Some of these studies have started even before the first attempts to model macrosegregation by [Flemings and Nereo \[1967\]](#), [Flemings et al. \[1968\]](#), and [Flemings and Nereo \[1968\]](#).

Basically, all models include the solid fraction, g^s , as input to predict mush permeability along with empirical data. An instance of such models is the work of [Xu and Li \[1991\]](#). Some models rely additionally on the primary dendrite arm spacing λ_1 like Blake-Kozeny [[Ramirez and Beckermann 2003](#)], or the secondary dendrite arm spacing λ_2 like Carman-Kozeny, as a meaningful parameter to determine an isotropic permeability. Other models like [Poirier \[1987\]](#) and [Felicelli et al. \[1991\]](#) derive an anisotropic permeability based on both λ_1 and λ_2 .

The present work uses Carman-Kozeny as a constitutive model for the isotropic permeability scalar (zero order tensor):

$$\mathbb{K} = \frac{\lambda_2^2 g^l 3}{180 (1 - g^l)^2} \quad (1.3)$$

1.2 Macrosegregation

Macrosegregation generally stems from a solubility difference between a liquid phase and one or more solid phases, along with a relative velocity between these phases. While the former is responsible for local solute enrichment or depletion, the latter will propagate the composition heterogeneity on a scale much larger than just a few dendrites. This is why macrosegregation could be observed on the scale of a casting, up to several meters in length. Microsegregation may be healed by heat treatments to speed up the diffusion process and allow homogenization. However, heterogeneities spanning on larger distances cannot be heat treated after solidification. Macrosegre-

Chapter 1. General Introduction

gation is thus an irreversible defect. Failure to prevent it, may lead to a substantial decline in the alloy's mechanical behaviour and its serviceability. Experimental investigations of macrosegregation in steels were the subject of numerous studies in the past and until now, like the work of [Suzuki and Miyamoto \[1973\]](#), [Shah and Moore \[1989\]](#), and [Lesoult \[2005\]](#). They were mainly motivated by industrial research that aimed at reducing defective production caused by macrosegregation. However, steels were not the only alloys that were investigated for segregation defects. Many studies relied on other metallic alloys as a replacement recourse, for their low melting points and well-known physical and mechanical properties. Examples are aluminium-based alloys (aluminium-copper or aluminium-silicon) [[Lesoult et al. 2001](#); [Ferreira et al. 2004](#); [Ferreira et al. 2009](#)] and lead-tin/tin-lead alloys [[Hebditch and Hunt 1974](#); [Prescott et al. 1994](#); [Hachani et al. 2012](#)]. Investigating macrosegregation is also common in organic compounds like the well-known sodium chloride [[Wanqi and Yaohe 1989](#); [Sarazin and Hellawell 1992](#); [Ludwig et al. 2012](#)], which have the advantage of being transparent.

Four main factors can (simultaneously) cause fluid flow leading to macrosegregation: thermosolutal convection in the liquid, solidification shrinkage, solutal and thermal contraction, movement and sedimentation of equiaxed crystals and finally solid deformation.

1.2.1 Liquid thermosolutal convection

During solidification, the liquid density undergoes changes due to temperature gradients. Generally for steels, an increasing temperature results in a lighter liquid phase and vice-versa. These variations create a driving force of thermal convection in the melt, during which chemical species are redistributed by convective transport. While a uniform composition could be maintained throughout the liquid bulk where convective transport is dominant, solute gradients may appear in zones where thermal convection currents are not sufficient to homogenise the liquid solution. Similarly to thermal gradient, a solute gradient is behind liquid density variations. Nevertheless, the link between the liquid's composition and its density varies from one alloy to another. For some alloys, a positive solute gradient creates a positive density gradient, while for others the opposite is true, due to a lighter solute effect in the melt density. Whether convection is solute or temperature dominated, convection currents are important in the formation of macrosegregation, especially that the liquid phase density varies considerably upon cooling the superheated alloy to room temperature.

1.2.2 Solidification shrinkage

Solids generally have a greater density than the liquid phase ($\langle \rho \rangle^s > \langle \rho \rangle^l$), thus occupy less volume, with some exceptions such as silicon, for which the opposite is true. Upon solidification, the liquid therefore moves towards the solidification front to compensate for the volume difference caused by the phase change, as well as the phases contraction mainly due to temperature gradient. When macrosegregation is triggered by solidification shrinkage, we speak of *inverse segregation*: while one would expect negative macrosegregation near the contact with the chill due to diffusion, shrinkage-induced flow promotes the opposite phenomenon, by bringing solute-richer liquid towards the solidifying areas, thus raising their solute content, and resulting in a positively segregated region. In contrast to liquid thermosolutal convection, shrinkage flow may cause macrosegregation even without gravity.

1.2.3 Movement of equiaxed grains

Globular and equiaxed dendritic grains nucleate and grow in the liquid bulk where thermal gradients are weak, or in the presence of inoculants. They are transported by the flow and can float or sediment, depending on their density [Beckermann 2002]. During their movement, the nearby liquid is driven away before the grains finally settle in the end of solidification. When the solute-rich liquid is expelled, a negative macrosegregation zone (often referred to as *negative segregation cone* in cast ingots) is detected where the grains have finally settled.

1.2.4 Solid deformation

Stresses of thermal and mechanical nature are always found in casting processes (e.g. bulging between rolls in continuous casting). Deformation of the semi-solid region located in the mushy zone causes a relative solid-liquid flow in the inward (tensile stresses) or outward (compressive stresses) direction, leading to macrosegregation.

1.3 Other defects

Apart from macrosegregation, other defects are also encountered in industrial processes. In the casting industry, defects like pores and cracks can be disastrous causing the cast product to be rejected. If possible, the product is reheated, remelted and then cast again. Otherwise it is scrapped. From an economic point view, these operations are very expensive.

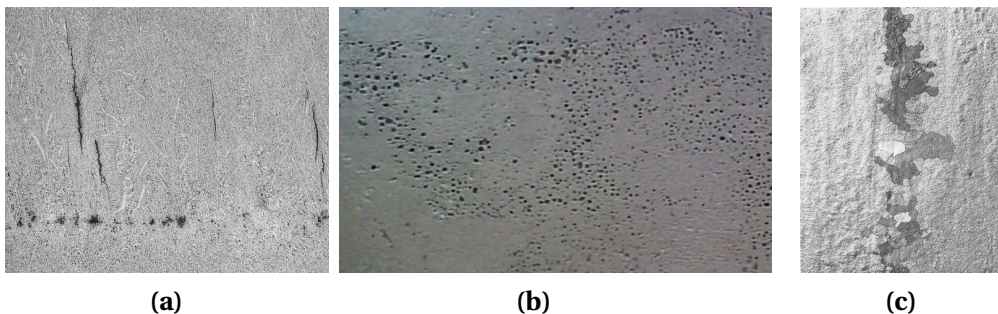


Fig. 1.7 – Three instances of solidification-related defects found in cast products: (a) internal crack in continuous casting [Arcelormittal] (b) surface cavities in ingot casting [Carlson et al. 2002] and (c) freckle in the form of a chain of equiaxed crystals in Ni-base superalloy investment casting [Giamei and Kear 1970].

Hot tearing

Hot tearing, also denoted solidification cracking or hot cracking, occurs in the mushy zone at high solid fractions when a failure or crack appears in the cast part. They refer to liquid regions enclosed in the solid, where feeding stops. Preferential sites for crack initiation are localised in regions where liquid feeding is difficult. The volume change combined with thermal stresses or external strains, may lead to cracks as shown in [fig. 1.7a](#). The temperature range in which the steel is vulnerable to hot tearing is known as the brittle temperature range (BTR), where the solid fraction is typically greater than 90%.

Porosity

Porosity is a void defect formed inside the casting or at the outer surface. It may be attributed to two different factors. Firstly, we speak of *shrinkage porosity*, when a void forms as a result of density differences between the liquid and its surrounding dendritic solid network, the latter being generally denser than the former. After solidification is complete, the casting surface may look like [fig. 1.7b](#). The second factor is the presence of dissolved gaseous phases in the melt, and is referred to as *gas porosity*. According to [Dantzig and Rappaz \[2009\]](#), these gases may be initially in the melt, or created by the reaction between the metal and water found in the air or trapped in grooves at the moulds surface. Providing sufficient cooling and pressure drop in the liquid, the latter becomes supersaturated. The nucleation of a gaseous phase is then triggered.

Freckles or segregated channels

The origin of this defect, shown in [fig. 1.7c](#), is a combined effect of microsegregation, buoyancy forces and fragmentation of the dendritic network. For a solute species that preferentially segregates into the liquid (partition coefficient less than unity) and locally reduce the liquid density, a solutal driving force is created inside the mushy zone, generating convection currents, with "plume" shapes as often reported in the literature [[Sarazin and Hellawell 1992](#); [Schneider et al. 1997](#); [Saad et al. 2015](#)]. Temperature gradient is often an additional force of convection as the liquid density is also temperature-dependent, the resulting driving force being thus qualified as "thermosolutal".

Equiaxed grains shown in [fig. 1.7c](#), are the growth result from free floating dendrite fragments in the solute-rich liquid channel. As solute accumulates in these areas, the thermosolutal convection is sustained, hence the channel solidification is delayed. This leads to the formation of a distinct crystal chain pattern, the so-called *freckle*, once the segregated channel completely solidifies.

1.4 Industrial Worries

Steel production has continuously increased over the years to meet the industrial needs. [Figure 1.8](#) shows this increase between 1980 and 2013 with a clear rise of the Chinese production. Quality constraints have also increased where specific grades of steel are needed in critical applications such as mega-structures in construction and heavy machinery. Other domains like the nuclear, are good examples showing the relevance of macrosegregation studies in developing nuclear components for the new generation Evolutionary Power Reactor, manufactured by Areva. Therefore, alloys with defects are considered vulnerable and should be avoided as much as possible during the casting process. As such, steelmakers have been investing in research, with the aim of understanding better the phenomena leading to casting problems, and improve the processes when possible.

Simulation software dedicated to alloy casting is one of the main research investments undertaken by steelmakers. These tools originating from academic research, are actively used to optimize the process. However, few are the tools that take into account the casting environment. For instance, the continuous casting process, in [fig. 1.7](#), is a chain process where the last steps involve rolling, heat treatments, forging, etc. The continuous casting machine itself not only consists of an open mould where solidification starts, but also includes rolls, water sprays and other components. A dedicated

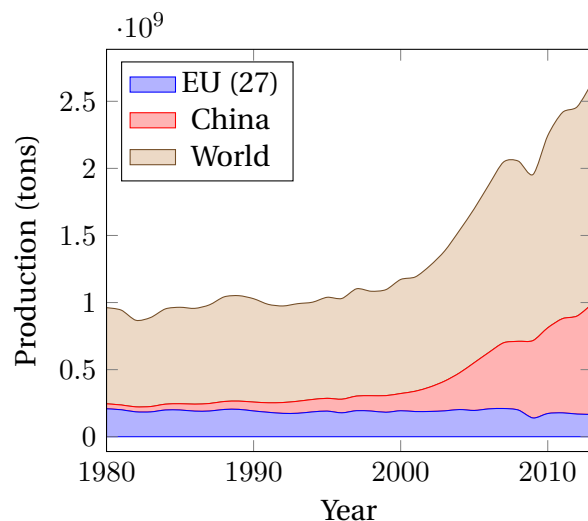


Fig. 1.8 – Evolution curves of crude steel worldwide production from 1980 to 2013 [WSA 2014].

software is one that can provide the geometric requirements with suitable meshing capabilities, as well as respond to metallurgical and mechanical requirements, mainly by handling:

- moulds and their interaction with the alloy (thermal resistances ...)
- alloy filling and predicting velocity in the liquid and mushy zone
- thermomechanical stresses in the solid
- multicomponent alloys and predicting macrosegregation
- microstructure and phases
- finite solute diffusion in solid phases
- real alloy properties (not just constant thermophysical/thermomechanical properties)
- ..., etc

1.5 Project context and objectives

1.5.1 Context

The European Space Agency (ESA) has been actively committed, since its foundation in 1975, to research. It covers not only exclusive space applications, but also fundamental science like solidification. This thesis takes part in the ESA project entitled **CCEMLCC**, abbreviating "Chill Cooling for the Electro-Magnetic Levitator in relation

1.5. Project context and objectives

with Continuous Casting of steel". The three-year project from late 2011 to late 2014 denoted *CCEMLCC II*, was preceded by an initial project phase, *CCEMLCC I*, from 2007 to 2009. The main focus is studying containerless solidification of steel under microgravity conditions. A chill plate is used to extract heat from the alloy, simulating the contact effect with a mould in continuous casting or ingot casting. A partnership of 7 industrial and academic entities was formed in *CCEMLCC II*. Here is a brief summary of each partner's commitment:

Academic partners

- Center for Material Forming (CEMEF) - France: numerical modelling of microgravity chill cooling experiments
- Deutsches Zentrum für Luft- und Raumfahrt (DLR or German Aerospace Centre) and Ruhr Universität Bochum (RUB) university - Germany: preparation of a chill cooling device for electromagnetic levitation (EML), microgravity testing and investigation of growth kinetics in chill-cooled and undercooled steel alloys
- University of Alberta - Canada: impulse atomization and spray deposition of the D2 tool steel
- University of Bremen - Institut für Werkstofftechnik (IWT) institute - Germany: study of D2 tool steel melt solidification in atomization processing

Industrial partners

- ARCELORMITTAL (France): elaboration of a series of steel grades used in microgravity and ground-based studies and characterisations.
- METSO Minerals Inc. (Finland): material production with D2 tool steel for spray forming
- TRANSVALOR (France): development and marketing of the casting simulation software *THERCAST®*

CEMEF, as an academic partner, contributed to the work by proposing numerical models in view of predicting the chill cooling of steel droplets. A first model was developed by [Rivaux \[2011\]](#). The experimental work by DLR considered various facilities and environments to set a droplet of molten alloy in levitation: EML ([fig. 1.9](#)) for ground-based experiments, microgravity during parabolic flight or sounding rockets and last, microgravity condition on-board the International Space Station (ISS).

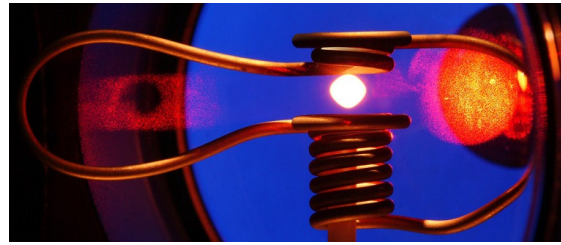


Fig. 1.9 – Electromagnetic levitation [DLR 2014].

1.5.2 Objectives and outline

The main focus of the present thesis is predicting macrosegregation with liquid dynamics assuming a fixed solid phase, i.e. no account of solid transport (e.g. equiaxed crystals sedimentation) and no account of solid deformation. At CEMEF, this scope has been adopted in previous studies by Gouttebroze [2005], Liu [2005], Mosbah [2008], Rivaux [2011], and Carozzani [2012]. Nevertheless, many modelling features evolved with time such as going from two-dimensional to three-dimensional modelling, resolution schemes for each of the conservation equations: energy, chemical species and liquid momentum, Eulerian or Lagrangian descriptions, modelling of grain structure and others. In this thesis, we propose a numerical model that takes into account i) the energy conservation in a temperature formulation based on a thermodynamic database mapping, ii) the liquid momentum conservation with thermosolutal convection and solidification shrinkage as driving forces, iii) solute mass conservation with solidification shrinkage to predict inverse segregation and iv) solidification paths at full equilibrium for multicomponent alloys. Moreover, all equations are formulated in a pure Eulerian description while using the level set method to keep implicitly track of the interface between the alloy and the surrounding gas.

To the author's knowledge, this work combining macrosegregation prediction using the level set methodology to track the metal-air interface during shrinkage has no precedent in casting and solidification literature. The model couples in a weak fashion, all four conservation equations presented in [fig. 1.10](#), showing on the one hand, that microsegregation is an essential common link between these equations, while on the other hand, the level set interacts with conservations equations by giving the interface position.

Numerical tools

The current thesis developments are done using C++ language as a part of the in-house code, known as *CimLib* [Digonnet et al. 2007; Mesri et al. 2009]. It's a finite element

library with an object-oriented hierarchy consisting of global finite element solvers for physical differential equations, also point-wise and element-wise solvers for preprocessing and postprocessing the finite element solution. It is also highly parallelised with MPICH2, which makes it possible to handle large meshes with heavy operations like mesh partitioning and adaptation. Side utilities for plotting and analysis are also developed, using python language.

Content outline

This manuscript consists of 5 chapters. In **chapter 2**, a short review introduces the state-of-art in the literature of macroscopic modelling of solidification with transport of energy, species, mass and momentum. **Chapter 3** provides details of the energy conservation equation and introduces a new temperature-based solver compatible with thermodynamic databases, **Chapter 4** focuses on the mass and momentum conservation equations and their derivation in the context of a single metallic domain (i.e. without the level set method) where the solid is assumed a fixed and rigid body. As an application, this chapter shows a breakthrough comparison between purely macroscopic and mesoscopic-macroscopic approaches in predicting the hydrodynamic instabilities that lead to channel segregation. The derived energy, mass and momentum equations for the monodomain model are revisited in **chapter 5** in the context of the level set method to take into account solidification shrinkage. The influence of shrinkage on macrosegregation is then studied in two different applications.

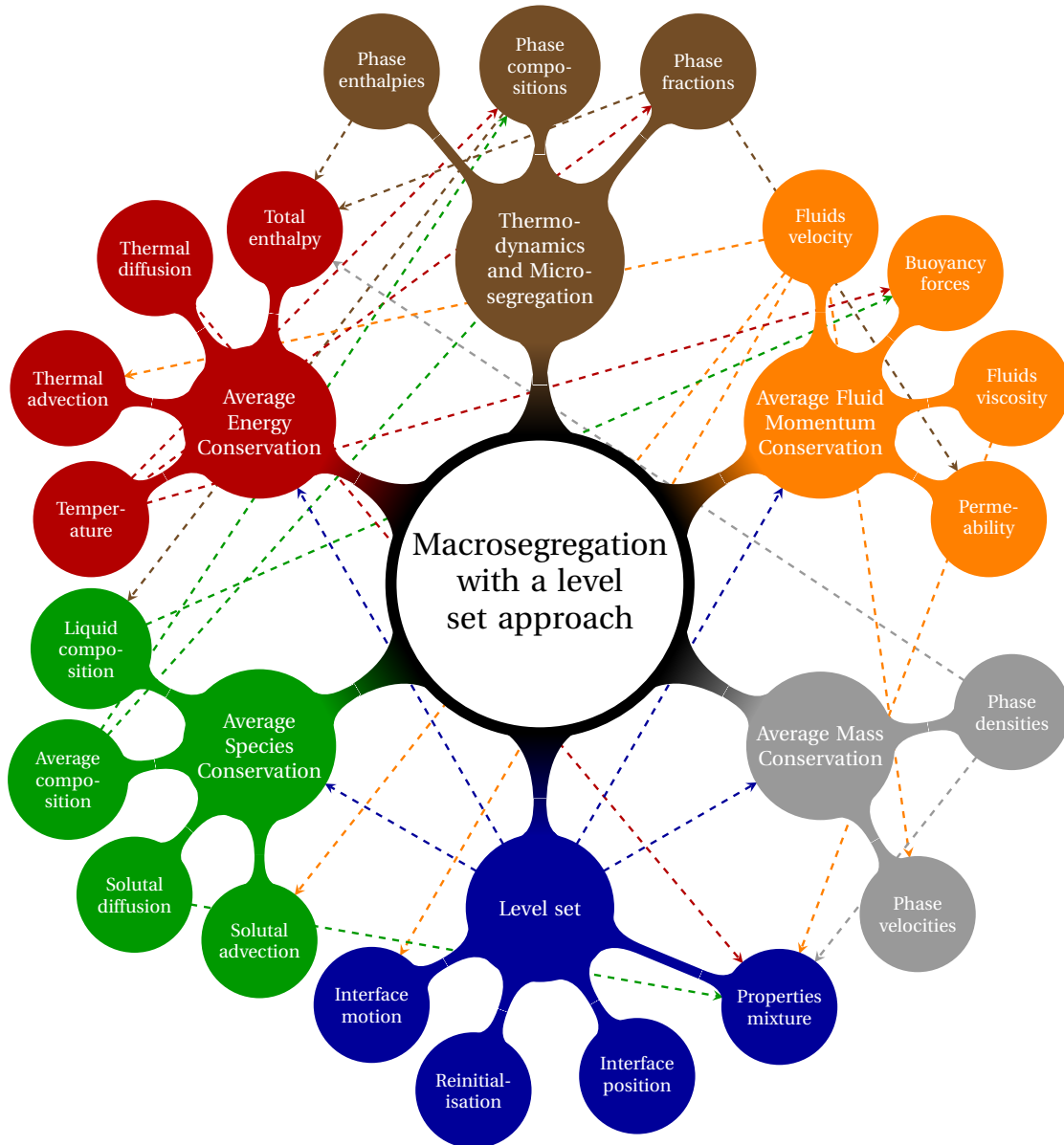


Fig. 1.10 – A graphical representation of the main elements of the numerical approach, for a macrosegregation model with the level set methodology, when no solid deformation or movement are considered. The dashed lines represent the interactions between the various components.

Résumé chapitre 1

Dans ce premier chapitre d'introduction, on introduit les notions de base en solidification. On s'intéresse particulièrement aux notions de ségrégation se produisant à l'échelle des structures de solidification et que l'on appelle *microségrégation*. Ce phénomène est directement lié à la différence de solubilité des espèces chimiques aux interfaces séparant les phases présentes dans l'alliage subissant la transformation.

Plusieurs facteurs, qu'ils soient relatifs au procédé de solidification ou inhérents au phénomène de changements de phase, peuvent les phases en mouvement. Ainsi, toute vitesse relative entre ces phases est à l'origine d'un transport des espèces chimiques et donc une redistribution à l'échelle des pièces coulées. On parle alors de *macroségrégation*.

Les ségrégations à l'échelle miroscopique peuvent être homogénéisées par le biais des traitements thermiques favorisant le transport par diffusion chimique. Cependant, la macroségrégation est souvent irréversible et donc la cause de rebut de pièces produites. Ce défaut, rencontré dans des procédés de coulé continue ou coulée en lingot, est appréhendé par les sidérurgistes qui investissent dans la recherche afin de mieux contrôler leur production. La présente thèse s'inscrit dans le cadre de l'étude de la macroségrégation, notamment quand la cause en est le mouvement de la phase liquide par convection thermosolutale et/ou par retrait à la solidification, tout en supposant que les différentes phases solides sont fixes et rigides.

Dans le **chapitre 2**, nous présentons un modèle de solidification basé sur la résolution des équations de conservation moyennées sur l'ensemble des phases, en utilisant la prise de moyenne sur des volumes élémentaires représentatifs. Ces équations comportent la conservation de la masse, l'énergie, la masse des espèces chimiques et la quantité de transport dans la phase liquide. Ce modèle est enrichi dans le **chapitre 3**, en proposant une nouvelle méthode de résolution de l'équation de la conservation d'énergie, avec la température comme variable principale. Cette méthode utilise des propriétés à l'équilibre thermodynamique tabulées à partir d'une base de données dédiée, donnant accès à des valeurs qui évoluent selon la composition de l'alliage. Dans le **chapitre 4**, on emploie cette méthode pour l'énergie, avec les autres équations de conservation, pour prédire la ségrégation en canaux produite par convection thermosolutale, sans aucun changement de volume à la solidification. Comme cela nécessite d'avoir un suivi d'interface métal-air, une méthode implicite de suivi d'interface est intégrée au modèle de solidification dans le **chapitre 5**. Le modèle final permet donc de prédire la macroségrégation produite par retrait à la solidification et par convection thermosolutale avec suivi de front métal.

Chapter 1. General Introduction

Chapter 2

Energy balance with thermodynamic tabulations

Contents

2.1 State of the art	20
2.2 Thermodynamic considerations	21
2.2.1 Volume averaging	21
2.2.2 The temperature-enthalpy relationship	22
2.2.3 Tabulation of properties	22
2.3 Numerical method	24
2.3.1 Enthalpy-based approach	28
2.3.2 Temperature-based approach	28
2.3.3 Convergence	29
2.4 Validation	30
2.5 Application: multicomponent alloy solidification	33
2.5.1 Tabulations	35
2.5.2 Discussion	37
2.6 Limitations	42

2.1 State of the art

To model macrosegregation during solidification, a minimum of four conservation equations are necessary: conservation of mass, momentum, chemical species and energy. The phase change literature contains a wealth of numerical methods to solve energy conservation in solidifying alloys. A comprehensive overview of these methods is given by [Swaminathan and Voller \[1993\]](#).

The corresponding equation associates the total average enthalpy to the temperature via intrinsic alloy properties, such as the heat capacity of the phases and the latent heat associated with the phase transformations. However, in the course of solidification and while macrosegregation is taking place, these properties change because the average composition may vary significantly: the transformation paths are thus modified, as well as the phases' composition and heat capacity. Similarly, the latent heat of phase transformations is not a mere constant that could be distributed as a function of the phase fractions assuming only temperature-dependent phases' properties, as often found in the literature [\[Bellet et al. 2009\]](#). It is thus impossible to establish a priori the dependence of the enthalpy with respect to temperature when macrosegregation alters the average composition, even in the case of full thermodynamic equilibrium between phases.

In this chapter, we discuss a suitable numerical scheme based on an enthalpy method, already used in the literature to alleviate this macrosegregation-related problem [\[Swaminathan and Voller 1993; Carozzani et al. 2013\]](#). Later on, we introduce a modified formulation, using the effective heat capacity method that increases the original scheme's efficiency.

This chapter introduces an enthalpy method that makes use of a temperature-based solver. It uses tabulated thermodynamic quantities (solidification paths, phases' enthalpy and composition) in a range of average compositions and temperatures as found in the literature [\[Doré et al. 2000; Thuinet and Combeau 2004; Du et al. 2007\]](#), with the aim of evaluating the total average enthalpy as well as the effective heat capacity. The novelty of the modified method resides in the use of thermodynamic tabulations without losing the advantages of the previous method, thus yielding faster computation times while maintaining a good accuracy.

2.2 Thermodynamic considerations

2.2.1 Volume averaging

The volume averaging technique, presented in ??, is considered when solving the energy equation in the presence of macrosegregation. The reason is that phase properties and distributions varying with the average composition, have a great impact on the average thermal properties, and hence on the overall heat transfer in the system. We recall the basic expression of the volume averaged value of a field ψ , by writing:

$$\langle \psi \rangle = \sum_{\phi} g^{\phi} \langle \psi \rangle^{\phi} \quad (2.1)$$

where g^{ϕ} denotes the volume fraction of phase ϕ in the RVE, and $\langle \psi \rangle^{\phi}$ is the intrinsic average of the quantity ψ in the RVE. It should be emphasized that the averaging technique applies to virtually all thermodynamic volumetric variables (enthalpy, density ...). Among these variables, the temperature is also considered to be uniform in the RVE.

Applying the volume averaging technique to the energy conservation equation along with interfacial balances between the phases, results in the following averaged equation [Rappaz et al. 2003]:

$$\frac{\partial \langle \rho h \rangle}{\partial t} + \nabla \cdot \langle \rho h \vec{v} \rangle = \nabla \cdot (\langle \kappa \rangle \vec{\nabla} T) + \langle \dot{Q}_V \rangle \quad (2.2)$$

where ρ stands for the density, h the mass enthalpy, \vec{v} the velocity field, κ the thermal conductivity, T the temperature and \dot{Q}_V a possible volumetric heat source. Equation (2.2) is the standard averaged form of the energy conservation equation used in non-stationary phase change problems.

It is clear that the nature of the temperature-enthalpy relationship plays a central role when formulating the resolution strategy of this nonlinear equation. Generally, it is admitted that, depending on the resolution strategy, it is necessary to express enthalpy as a function of temperature or vice-versa, together with associated partial derivatives, $\frac{\partial \langle \rho h \rangle}{\partial T}$ or $\frac{\partial T}{\partial \langle \rho h \rangle}$.

It is noted that in the FEM context, the RVE is represented by a node in a finite element, so for instance the temperature in a RVE is denoted T_j henceforth, where j represents the index of the node localising the RVE.

2.2.2 The temperature-enthalpy relationship

In solidification problems, additional variables are involved in [eq. \(2.1\)](#) and [eq. \(2.2\)](#), like the transformation path that defines the history of the phase fractions, as well as the average chemical composition $\langle w_i \rangle$, i being the index of the chemical species (only the solutes are considered). The temperature-enthalpy relation averaged over the phases in a given RVE writes:

$$\langle \rho h \rangle = \sum_{\phi} g^{\phi}_{(T, \langle w_i \rangle \dots)} \langle \rho \rangle^{\phi}_{(T, \langle w_i \rangle^{\phi} \dots)} \langle h \rangle^{\phi}_{(T, \langle w_i \rangle^{\phi} \dots)} \quad (2.3)$$

Note that the volume average enthalpy is approximated by the product $\langle \rho h \rangle^{\phi} = \langle h \rangle^{\phi} \langle \rho \rangle^{\phi}$ in the current work. As stated in the introduction, it becomes clear from [eq. \(2.3\)](#) that phase properties, i.e. average phase density, $\langle \rho \rangle^{\phi}$ and enthalpy, $\langle h \rangle^{\phi}$, are temperature and composition dependent. This equation is the key to convert the average volume enthalpy to temperature (through a procedure named *H2T*) or vice-versa (*T2H*). The values of the different phase fractions g^{ϕ} (solidification path) and phase enthalpies $\langle \rho h \rangle^{\phi}$ are thus needed to close the relation.

2.2.3 Tabulation of properties

The complexity of performing a thermodynamic conversion is directly linked to the simplicity of determining the alloy properties, namely the phase fractions and both phase densities and enthalpies. In the case of binary alloys and with several assumptions with respect to the system (e.g., linear monovariant lines in temperature-composition relationships of the phase diagram, constant heat capacity of phases and constant latent heat of transformations, equilibrium approximations between phases) analytical calculations are often used to determine the phase fractions and phase compositions. Nevertheless, analytical relations are more complex or even impossible to derive in the case of multicomponent alloys ($i > 1$), or even for binary alloys with multiple phase transformations (e.g. peritectic and eutectic reactions) with a nonlinear phase diagram.

To overcome this problem, one can resort to thermodynamic databases and phase equilibrium calculations to tabulate the transformation paths and the phase densities and enthalpies for a given range of temperatures and average compositions. It is a handy solution for two main reasons: first, the conversion is merely a binary search in a table; secondly, it is a simple solution for coupling with macrosegregation. In this way, phase fractions g^{ϕ} are tabulated as functions of temperature and average composition, while for each phase ϕ the mass enthalpy, $\langle h \rangle^{\phi}$, and the density, $\langle \rho \rangle^{\phi}$, are

2.2. Thermodynamic considerations

tabulated as functions of temperature and phase intrinsic average compositions $\langle w_i \rangle^\phi$, as well as other possible parameters.

Table 2.1 summarizes the steps in order to perform a temperature-to-enthalpy ($T2H$) conversion using the predefined tabulation approach. In step 1, the transformation path is acquired for each average composition, $\langle w_i \rangle$, and temperature, T , to determine the list of phases, their volume fractions g^ϕ and their intrinsic compositions $\langle w_i \rangle^\phi$, assuming full equilibrium. In step 2, the phase enthalpy $\langle h \rangle^\phi$ and density $\langle \rho \rangle^\phi$ are determined by searching for the temperature and the already known phase composition $\langle w_i \rangle^\phi$. In step 3, the average volume enthalpy is computed from the volume fraction, density and mass enthalpy of phases using [eq. \(2.3\)](#). A flowchart explaining $T2H$ conversion steps is given in [fig. 2.1](#).

Table 2.1 – Tabulation processing for a $T2H$ procedure

Step Number	1	2	3
Inputs	$T, \langle w_i \rangle$	$T, \langle w_i \rangle^\phi$	$g^\phi, \langle \rho \rangle^\phi \langle h \rangle^\phi$
Outputs	$g^\phi, \langle w_i \rangle^\phi$	$\langle \rho \rangle^\phi, \langle h \rangle^\phi$	$\langle ph \rangle$ (eq. (2.3))

The methodology to build the tabulations is straightforward. It is based on two main scans. On the one hand, intervals for the variation of the average composition $\langle w_i \rangle$ are chosen from the known alloy composition. These variations have to cover the extreme values adopted during the simulation, which are not known a priori. An interval is also selected for the variation of temperature. The latter is easier to determine as it usually starts from the initial melt temperature and goes down to the room temperature in a standard casting simulation. For each mapping of composition and temperature, a thermodynamic equilibrium state is computed. The outputs are the number of phases encountered, together with their fraction and intrinsic compositions. On the other hand, for each phase, a scan of the intrinsic composition and temperature is made to compute the intrinsic properties. The same temperature interval and step as defined earlier are used.

Regarding the enthalpy-to-temperature conversion ($H2T$) shown in the flowchart in [fig. 2.2](#), a backward iterative $T2H$ search is performed. For a known composition $\langle w_i \rangle$, denoting (τ) the iteration index to convert the enthalpy H_{input} , we start with an initial guess for temperature $T^{(\tau=0)}$ then convert it to an enthalpy $H^{(\tau=0)}$ with the $T2H$ conversion. Using an appropriate nonlinear algorithm (Brent is the most versatile in our case), we aim at minimizing the following scalar residual: $R_H = |H_{\text{input}} - H^{(\tau)}|$. Once the algorithm has converged, the temperature $T^{(\tau)}$ is the result of the $H2T$ conversion. It is inferred that the first conversion ($T2H$) is a direct one whereas the latter ($H2T$) is

Chapter 2. Energy balance with thermodynamic tabulations

indirect and requires a series of iterative steps; each step being a single $T2H$ resolution. In other words, a $H2T$ conversion is a backward search for a temperature, hence it is slower. It is important to realise that this conversion's speed lag is exacerbated when tabulations increase in size (e.g. large number of temperature and composition steps) and complexity (e.g., multicomponent industrial alloys used in casting), since the search gets more complicated with the increasing number of input columns (one column for each alloying element).

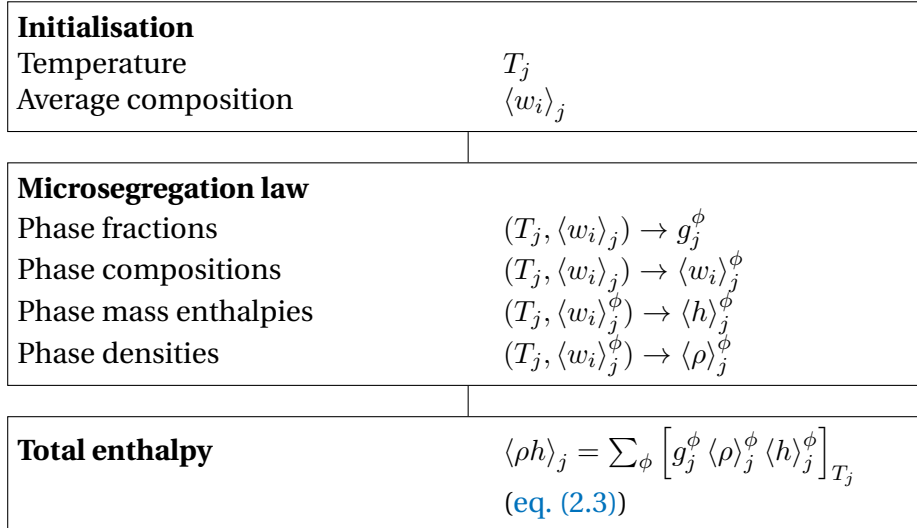


Fig. 2.1 – Algorithm for a single temperature to enthalpy ($T2H$) conversion at node j .

2.3 Numerical method

The finite element method is used to solve the energy conservation as expressed by [eq. \(2.2\)](#). A test function \mathcal{W} belonging to the Hilbertian Sobolev space $\mathcal{H}^1(\Omega_E)$ of continuous integrable test functions is used to formulate the integral variational form of [eq. \(2.2\)](#) [[Süli 2000](#)]. A Fourier boundary condition is considered on the domain boundary $\partial\Omega_E$. The domain Ω is discretised using first-order linear simplexes, Ω_E , defined by their number of local nodes, NbLoc: triangles in 2D with NbLoc=3 and tetrahedra in 3D with NbLoc=4. The outcome is a residual that we aim to minimize so that the conservation principle is satisfied. Therefore, the weak form writes:

$$\begin{aligned} \forall \mathcal{W} \in M = \{u \in \mathcal{H}^1(\Omega_E)\} \\ \int_{\Omega_E} \mathcal{W} \frac{\partial H}{\partial t} dV + \int_{\Omega_E} \mathcal{W} \left\langle \vec{v}^l \right\rangle \cdot \vec{\nabla} \langle \rho h \rangle^l dV - \int_{\Omega_E} \mathcal{W} \nabla \cdot (\langle \kappa \rangle \vec{\nabla} T) dV - \int_{\Omega_E} \mathcal{W} \left\langle \dot{Q}_V \right\rangle dV = 0 \end{aligned} \quad (2.4)$$

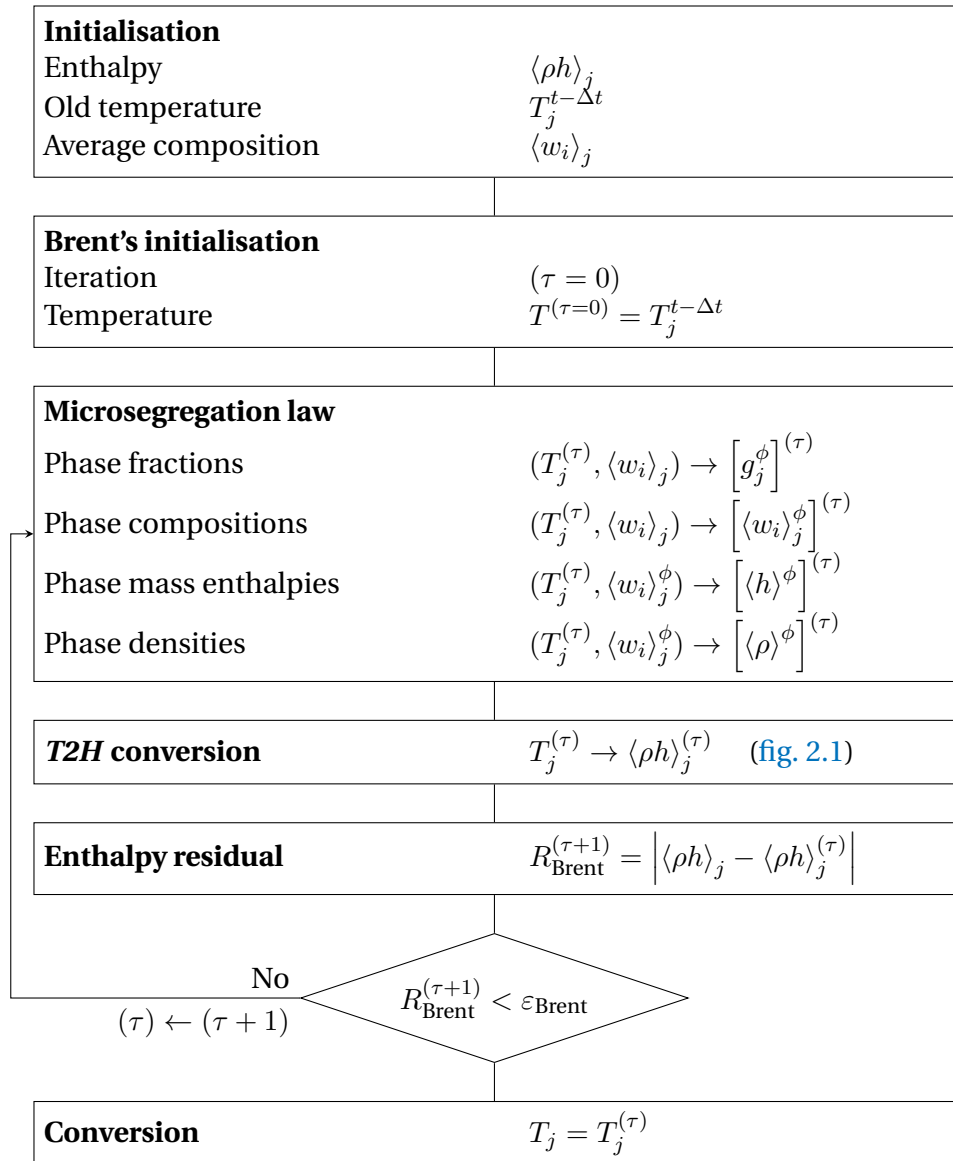


Fig. 2.2 – Algorithm for a single enthalpy to temperature ($H2T$) conversion at node j .

Chapter 2. Energy balance with thermodynamic tabulations

where $H = \rho h$ is the volumetric enthalpy, introduced to simplify notations in the following. Furthermore, we assume a static solid phase and an incompressible liquid phase, which allows recasting the second term of [eq. \(2.2\)](#) into $\langle \vec{v}^l \rangle \cdot \vec{\nabla} \langle \rho h \rangle^l$. $\langle \rho h \rangle^l = \langle \rho \rangle^l \langle h \rangle^l$ is not main variable of the energy conservation equation's weak form, [eq. \(2.4\)](#). Therefore we express it as a function of temperature, which is related to the main variable via the enthalpy-temperature relation:

$$\vec{\nabla} \langle \rho h \rangle^l = \vec{\nabla} (\langle \rho \rangle^l \langle h \rangle^l) = \langle \rho \rangle^l C_p^l \vec{\nabla} T \quad (2.5)$$

where C_p^l is the mass heat capacity of the liquid phase. Ideally, this value should be taken directly from the thermodynamic database if it is available. Otherwise, it can be derived by differentiation of the tabulated liquid mass enthalpy with respect to temperature. In this work, C_p^l is considered constant, equal to the alloy's initial mass heat capacity. The steps for discretising in time and space [eq. \(2.4\)](#) are well detailed in some text books like [Rappaz et al. \[2003\]](#). As for enthalpy and temperature, they are spatially discretised in each simplex using interpolations functions \mathcal{P} , thus defining the nodal values H_j and T_j , respectively:

$$H = \sum_{j=1}^{\text{NbLoc}} \mathcal{P}_j H_j \quad (2.6)$$

$$T = \sum_{j=1}^{\text{NbLoc}} \mathcal{P}_j T_j \quad (2.7)$$

The Galerkin formulation gives the expression for the residual contribution at a mesh node i (here i is not the usual solute index) for time step t in a local element Ω_E :

$$(R_i^E)^t = \mathcal{M}_{ij}^E (H_j^t - H_j^{t-\Delta t}) + \mathcal{A}_{ij}^E T_j^t + (\mathcal{K1}_{ij}^E + \mathcal{K2}_{ij}^E) T_j^t - \mathcal{F}_i^E - \mathcal{Q}_i^E = 0 \quad (2.8)$$

$i, j : 1 \rightarrow \text{NbLoc}$

where the volumetric contributions are detailed as follows:

$$\text{transient term: } \mathcal{M}_{ij}^E = \int_{\Omega_E} \frac{1}{\Delta t} \mathcal{P}_i \mathcal{P}_j \, dV \quad (2.9)$$

$$\text{advection term: } \mathcal{A}_{ij}^E = \int_{\Omega_E} \langle \rho \rangle^l C_p^l \mathcal{P}_i \langle \vec{v}^l \rangle \cdot \vec{\nabla} \mathcal{P}_j \, dV \quad (2.10)$$

$$\text{diffusion term: } \mathcal{K1}_{ij}^E = \int_{\Omega_E} \langle \kappa \rangle \vec{\nabla} \mathcal{P}_i \vec{\nabla} \mathcal{P}_j \, dV \quad (2.11)$$

$$\text{source term: } \mathcal{Q}_i^E = \int_{\Omega_E} \mathcal{P}_i \langle \dot{Q}_V \rangle \, dV \quad (2.12)$$

while the surface boundary contributions are given by:

$$\text{boundary condition term 1: } \mathcal{K}2_{ij}^E = \int_{\partial\Omega_E} h_{\text{ext}} \mathcal{P}_i \mathcal{P}_j \, dS \quad (2.13)$$

$$\text{boundary condition term 2: } \mathcal{F}_i^E = \int_{\partial\Omega_E} h_{\text{ext}} T_{\text{ext}} \mathcal{P}_i \, dS \quad (2.14)$$

The surface integrals $\mathcal{K}2_{ij}^E$ and \mathcal{F}_i^E are related to a Fourier-type boundary condition, with h_{ext} as a coefficient of heat exchange and T_{ext} as the external temperature far from the boundary. The energy conservation principle is satisfied when the sum of the residual contributions coming from all the mesh elements is zero. In other words, the following global residual defined by the assembly of these contributions, should be minimized:

$$(R_i)^t = \mathcal{M}_{ij} \left(H_j^t - H_j^{t-\Delta t} \right) + \mathcal{A}_{ij} T_j^t + (\mathcal{K}1_{ij} + \mathcal{K}2_{ij}) T_j^t - \mathcal{F}_i - \mathcal{Q}_i = 0 \quad (2.16)$$

$i, j : 1 \rightarrow \text{NbGlob}$

where the global tensors \mathcal{M}_{ij} , \mathcal{A}_{ij} , $\mathcal{K}1_{ij}$, $\mathcal{K}2_{ij}$, \mathcal{F}_i and \mathcal{Q}_i contain respectively, after an assembly step, the contributions of the local matrices \mathcal{M}_{ij}^E , \mathcal{A}_{ij}^E , $\mathcal{K}1_{ij}^E$, $\mathcal{K}2_{ij}^E$, \mathcal{F}_i^E and \mathcal{Q}_i^E from each discretised element in the domain Ω . Accordingly, the indices i and j refer to global node numbers, where the total number of nodes is denoted by "NbGlob".

It is clear that the global residual inherits the dependence between volumetric enthalpy and temperature. This is shown in eq. (2.16) where the average volume enthalpy is a function of the temperature. It infers that this residual is a non-linear function; therefore minimizing it requires an iterative non-linear algorithm.

Our choice settles on the Newton-Raphson method, known for its quadratic convergence speed. A solidification problem can induce severe non-linearities from the release of the latent heat (which itself is temperature and composition dependent) and the variations of the average thermophysical properties of the alloy with respect to temperature, phase fraction and average composition. This algorithm could thus treat such variations. Considering the link between the properties and temperature, eq. (2.16) may be solved either for the average volumetric enthalpy or for the temperature as the nodal unknown, hence both formulations are presented hereafter.

2.3.1 Enthalpy-based approach

The residual is re-written using a Taylor series expansion to the first order for a non-linear iteration (ν) :

$$(R_i)^{(\nu+1)} = (R_i)^{(\nu)} + \left(\frac{\partial R}{\partial H} \right)_{ij}^{(\nu)} \Delta H_j^{(\nu)} + \mathcal{O}(H_j^2) \quad (2.17)$$

Neglecting the second order terms, the suggested correction at each iteration in view of cancelling the residual and giving the new value $H_j^{(\nu)}$, is given by the linear system in eq. (2.18) relative to what we call the *Hsolver*:

$$\left(\frac{\partial R}{\partial H} \right)_{ij}^{(\nu)} (H_j^{(\nu+1)} - H_j^{(\nu)}) = -R_i^{(\nu)} \quad (2.18)$$

where $\frac{\partial R}{\partial H}$ is a global tangent matrix yielding the variations of the residual with respect to the volumetric enthalpy in the previous iteration, $H_j^{(\nu)}$. The detailed flow chart for the *Hsolver* is given in fig. 2.3. If eq. (2.8) is considered, then the contribution of an element Ω_E writes:

$$\left(\frac{\partial R^E}{\partial H} \right)_{ij}^{(\nu)} = \underbrace{\mathcal{M}_{ij}^E + \mathcal{A}_{ij}^E \left(\frac{\partial T}{\partial H} \right)_j^{(\nu)}}_{\text{no sum on } j} + \underbrace{(\mathcal{K}1_{ij}^E + \mathcal{K}2_{ij}^E) \left(\frac{\partial T}{\partial H} \right)_j^{(\nu)}}_{\text{no sum on } j} \quad (2.19)$$

Equation (2.19) is the core of the enthalpy-based solver. The resolution of eq. (2.18) then yields a new estimate of the vector of nodal volumetric enthalpies $H^{(\nu+1)}$, which are the only unknowns to be solved for. Once determined at iteration (ν), convergence tests are performed.

2.3.2 Temperature-based approach

Similarly to the *Hsolver*, the local residual is recast for a nonlinear iteration (ν), leading this time to an iterative temperature correction:

$$\left(\frac{\partial R}{\partial T} \right)_{ij}^{(\nu)} (T_j^{(\nu+1)} - T_j^{(\nu)}) = -R_i^{(\nu)} \quad (2.20)$$

where $\frac{\partial R}{\partial T}$ is a global tangent matrix yielding the variations of the residual with respect to temperature $T_j^{(\nu)}$ at the previous iteration. This solver will be referred to as the *Tsolver*. The corresponding flow chart is given in fig. 2.4. The contribution of an

element Ω_E to this tangent matrix is evaluated as:

$$\left(\frac{\partial R^E}{\partial T} \right)_{ij}^{(\nu)} = \underbrace{\mathcal{M}_{ij}^E \left(\frac{\partial H}{\partial T} \right)_j^{(\nu)}}_{\text{no sum on } j} + \mathcal{A}_{ij}^E + (\mathcal{K}1_{ij}^E + \mathcal{K}2_{ij}^E) \quad (2.21)$$

In contrast to the previous solver, eq. (2.21) is the core of the temperature-based solver. The resolution of eq. (2.20) then yields a new estimate of the vector of nodal temperatures $T^{(\nu+1)}$, which are the only unknowns to be solved for. Once updated for iteration (ν) , convergence tests are performed.

2.3.3 Convergence

The previous two sections described the iterative resolution of the same discretised energy conservation by both *Tsolver* and *Hsolver*. However, in eqs. (2.19) and (2.21), an important term emerges from the tangent matrix evaluation describing the variations between enthalpy and temperature: $\frac{\partial T}{\partial H}$ and $\frac{\partial H}{\partial T}$.

This term invokes the previously mentioned temperature-enthalpy tabulations which depend on the alloy composition. Consequently, $\frac{\partial T}{\partial H}$ (respectively $\frac{\partial H}{\partial T}$) has a great influence on the convergence of the *Hsolver* (respectively the *Tsolver*). When eq. (2.18) or eq. (2.20) is solved at iteration (ν) , this term is written using a finite difference:

$$\mathbf{Hsolver} \quad \left(\frac{\partial T}{\partial H} \right)_j^{(\nu+1)} = \frac{T_j^{(\nu+1)} - T_j^{(\nu)}}{\langle \rho h \rangle_j^{(\nu+1)} - \langle \rho h \rangle_j^{(\nu)}} \quad (2.22)$$

$$\mathbf{Tsolver} \quad \left(\frac{\partial H}{\partial T} \right)_j^{(\nu+1)} = \frac{\langle \rho h \rangle_j^{(\nu+1)} - \langle \rho h \rangle_j^{(\nu)}}{T_j^{(\nu+1)} - T_j^{(\nu)}} \quad (2.23)$$

For the *Tsolver*, the enthalpy $\langle \rho h \rangle_j^{(\nu)}$ is needed to evaluate eq. (2.23). In contrast, the *Hsolver* requires the value of $T_j^{(\nu)}$ to evaluate the corresponding eq. (2.22). In both cases, the unknown is determined by the tabulations. The indices next to the mentioned unknowns indicate that this relation is used for each iteration (ν) at each mesh node j , hence affecting the global resolution time between the two solvers. The *Hsolver* needs a $H2T$ to evaluate $\frac{\partial T}{\partial H}$, whereas the *Tsolver* needs a $T2H$ to evaluate $\frac{\partial H}{\partial T}$. It can be seen that *Tsolver* uses solely $T2H$ procedure (flowchart in fig. 2.1) and the thermodynamic tabulations to determine the volumetric enthalpy, hence the term $\frac{\partial H}{\partial T}$. On the other hand, *Hsolver* repeats the same procedure a finite number of times in order to determine a temperature output through $H2T$ (flowchart in fig. 2.2) and use it to compute $\frac{\partial T}{\partial H}$. This algorithmic difference leverages the *Tsolver* in terms of computa-

tion time providing the same numerical accuracy while conserving the total system energy.

Convergence tests are necessary at the end of each iteration of the energy solver to determine the convergence status of the algorithm. In the context of the *Tsolver* for instance, the residual is re-evaluated with the newly determined temperature $T_j^{(\nu+1)}$ and enthalpy $H_j^{(\nu+1)}$ so [eq. \(2.16\)](#) rewrites:

$$(R_i)^{(\nu+1)} = \mathcal{M}_{ij} \left(H_j^{(\nu+1)} - H_j^{t-\Delta t} \right) + \mathcal{A}_{ij} T_j^{(\nu+1)} + (\mathcal{K}1_{ij} + \mathcal{K}2_{ij}) T_j^{(\nu+1)} - \mathcal{F}_i - \mathcal{Q}_i$$

$$i, j : 1 \rightarrow \text{NbGlob}$$
(2.24)

The norm of the current residual, $\|R^{(\nu+1)}\|$, is compared to a fixed small value $\varepsilon_R \approx [10^{-5}; 10^{-4}]$. The resulting temperature variation, $|T_j^{(\nu)} - T_j^{(\nu-1)}|$, should also respond to similar criterion between two consecutive iterations. For that purpose, we compare it to another fixed value $\varepsilon_T \approx [10^{-3}; 10^{-2}]$. Convergence is ultimately achieved when the following criteria are simultaneously met:

$$\begin{cases} \|R^{(\nu+1)}\| < \varepsilon_R \\ \text{Max}_{j:1 \rightarrow \text{NbGlob}} |T_j^{(\nu+1)} - T_j^{(\nu)}| < \varepsilon_T \end{cases} \quad (2.25)$$

A comparison of both solver formulations is done in the hereafter test cases section.

2.4 Validation

The two solvers are tested in a purely diffusive case for a one-dimensional solidification configuration. Predictions with a 1D front tracking model [[Gandin 2000](#)] are used as a benchmark. They provides solutions for the temperature and solid fraction during directional solidification of a 10 cm long ingot. The nominal composition, w_0 , is Al-7 wt. % Si. The melt having a uniform initial temperature, T_0 , is cooled with a heat exchange coefficient, h_{ext} , with a fixed external temperature, T_{ext} (assuming a Fourier boundary condition) from one side, the other side being adiabatic. The initial conditions, boundary conditions and alloy properties are all listed in [table 2.2](#).

For this simple test case, we use linear temperature dependence of the intrinsic phase enthalpies, that is $\langle \rho h \rangle^s = \rho C_p T$ and $\langle \rho h \rangle^l = \rho(C_p T + L)$, where ρ is the alloy density, C_p is the heat capacity per unit mass and L is the latent heat per unit mass. Values for ρ , C_p and L , as well as for the thermal conductivities, $\kappa = \langle \kappa \rangle^l = \langle \kappa \rangle^s$, are taken constant.

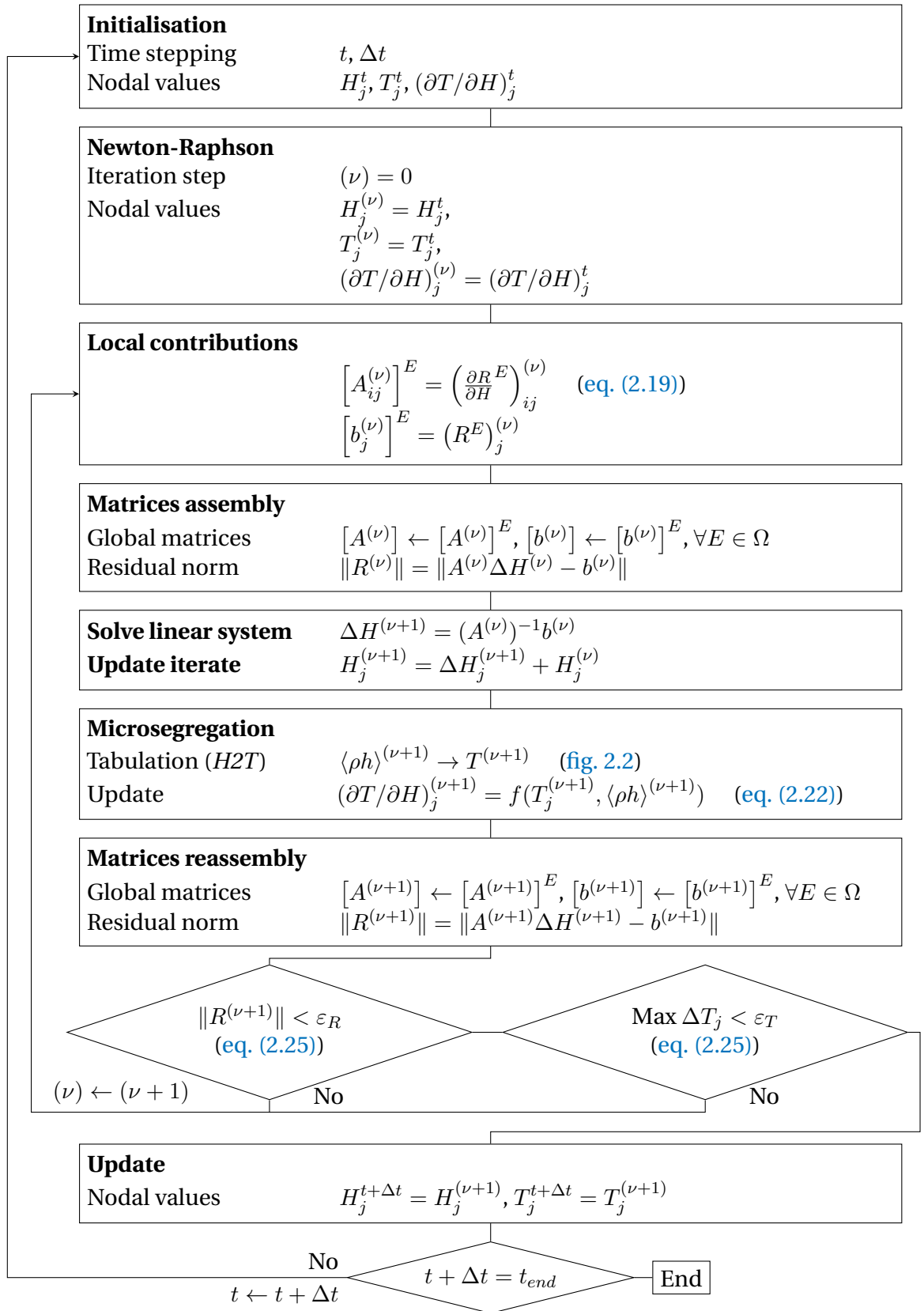


Fig. 2.3 – Resolution algorithm of the enthalpy-based solver.

Chapter 2. Energy balance with thermodynamic tabulations

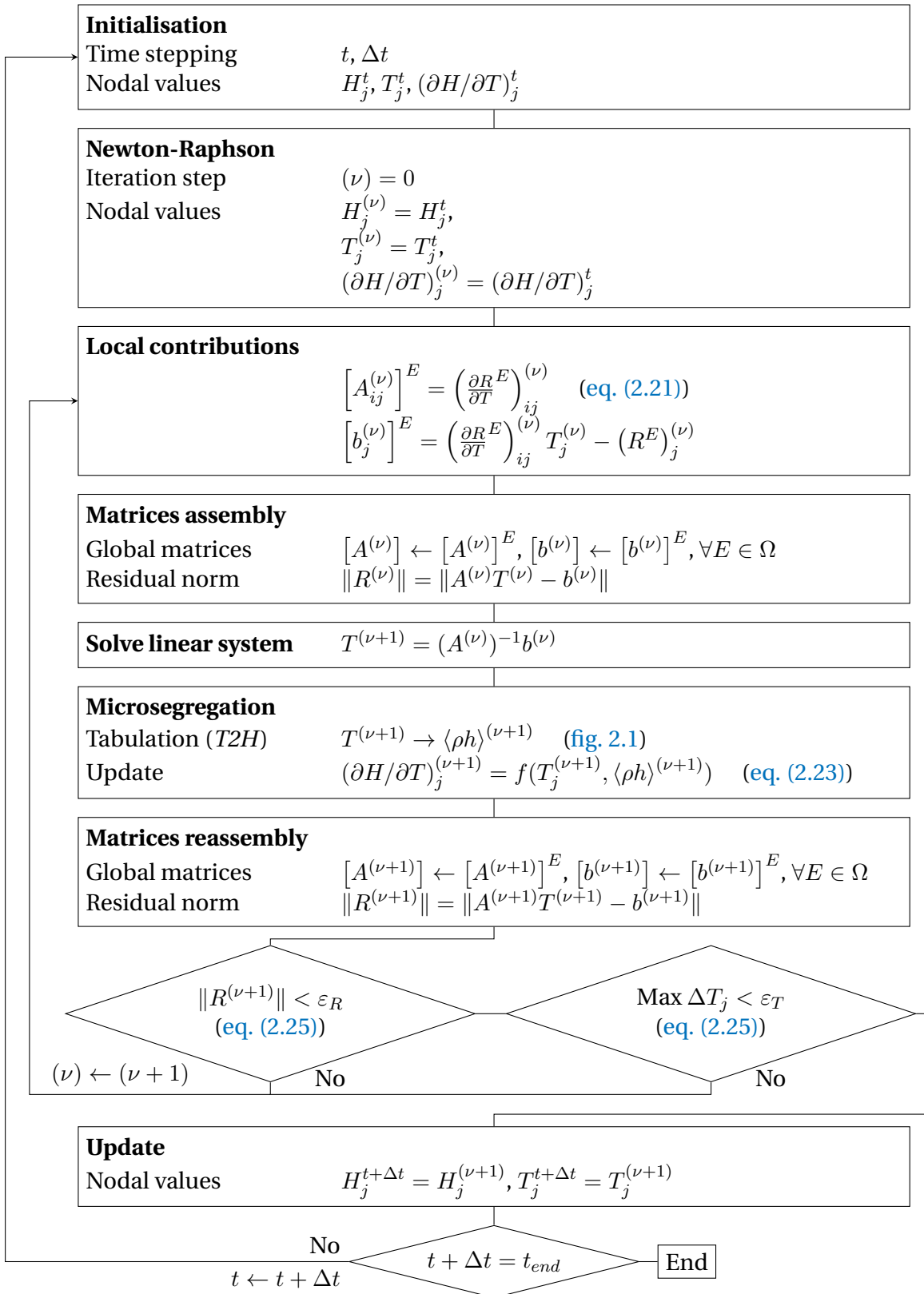


Fig. 2.4 – Resolution algorithm of the temperature-based solver.

2.5. Application: multicomponent alloy solidification

A Gulliver-Scheil approximation is used to compute a single relationship between temperature and volume solid fraction, g^s , in the absence of macrosegregation. This is done assuming a linear binary phase diagram and thus requires using the properties listed in [table 2.2](#), i.e. the segregation coefficient, k , the liquidus slope, m_L , the liquidus temperature, T_L , and the eutectic temperature, T_E . [Figure 2.5](#) show the comparison with the *Hsolver* and *Tsolver*. The cooling curves and liquid fraction results are found superimposed to the front tracking solution, thus giving validation of the implementation as well as the iterative schemes presented above to solve the energy conservation

Table 2.2 – Parameters for the pure diffusion test case with an Al-7 wt.% Si alloy presented in [fig. 2.5](#)

Parameter	Symbol	Value	Unit
Nominal composition	w_0	7	wt.%
Liquidus temperature	T_L	618	°C
Eutectic temperature	T_E	577	°C
Segregation coefficient	k	0.13	–
Liquidus slope	m_L	-6.5	K wt.% ⁻¹
Density	ρ	2600	kg m ⁻³
Liquid heat capacity	C_p	1000	J kg ⁻¹ K ⁻¹
Enthalpy of fusion	L	365 384	J kg ⁻¹
Thermal conductivity	κ	70	W m ⁻¹ K ⁻¹
Heat transfer coefficient	h_{ext}	500	W m ⁻² K ⁻¹
External temperature	T_{ext}	100	°C
Initial temperature	T_0	800	°C
Ingot length		0.1	m
FE mesh size		10^{-3}	m
Time step	Δt	0.1	s
Convergence criterion (residual)	ε_R	10^{-6}	–
Convergence criterion (temperature)	ε_T	10^{-2}	K

2.5 Application: multicomponent alloy solidification

We have shown that the efficiency of the temperature-based resolution resides in its performance when combined with thermodynamic tabulations. A multicomponent alloy consists of at least two solute elements, and therefore the tabulation size increases, hence the number of search operations also increases. To demonstrate the

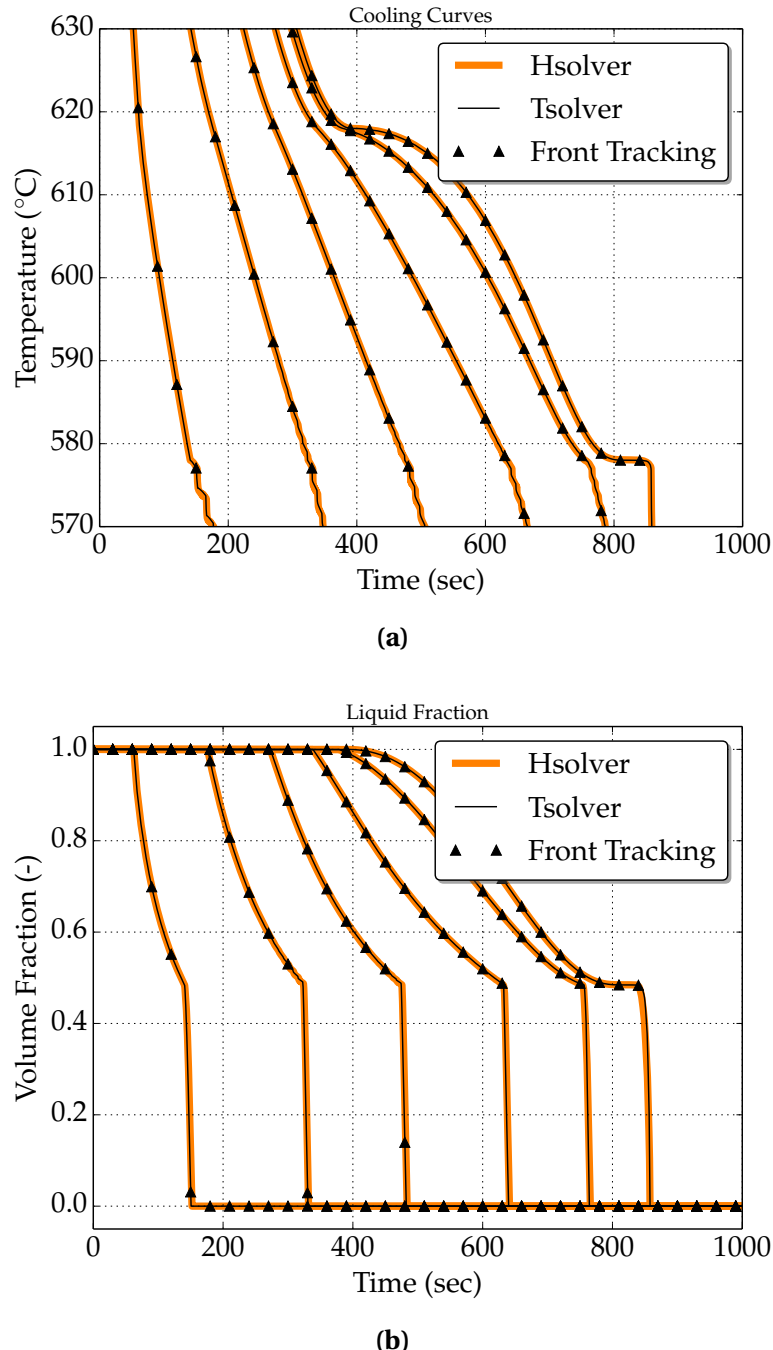


Fig. 2.5 – Computed unidirectional heat diffusion during solidification of an Al-7 wt.% Si alloy using (orange) the enthalpy method and (black) the temperature method, comparison being made for (a) cooling curves and (b) the liquid fraction history. Each curve corresponds to a position along the sample, from 0 cm (cooling side) to 10 cm (insulated side), with 2 cm spacing between the positions. The reference solution by the Front Tracking method (values in shown by the triangular markers).

speed-up ability of the temperature-based approach while predicting all phase transformations during macrosegregation caused solely by mass diffusion, we consider the solidification of a ternary alloy, Fe-2 wt.% C-30 wt.% Cr. In order to neglect fluid flow resolution, we assume that solidification in this case is so slow that no forces are generated inside the melt, while additionally all buoyancy forces are also neglected, so no momentum conservation is solved in this section.

As illustrated in [fig. 2.6a](#), the alloy domain has a cylinder shape close to 3-inch height \times 1-inch diameter. Exact values are reported in [table 2.3](#) with all material properties, initial and boundary conditions, as well as numerical parameters for the simulations. The steel melt is initially at 1395 °C. The temperature of the bottom surface is imposed with a constant decreasing rate of 0.1 K s⁻¹ starting with 1380 °C as shown in [fig. 2.6b](#), i.e. 40 °C higher than the nominal liquidus temperature as shown in [fig. 2.7](#). The other surfaces are kept adiabatic.

The cylinder is held in a vertical position parallel to the gravity vector, the latter pointing downwards. [fig. 2.7](#) also provides the transformation path of the alloy at nominal composition, i.e. assuming no macrosegregation and full thermodynamic equilibrium as computed with ThermoCalc and the TCFE6 database [[TCFE6 2010](#); [Andersson et al. 2002](#)]. A total of 5 phases need to be handled, the characteristic temperature for their formation being reported in [fig. 2.6b](#).

2.5.1 Tabulations

Full thermodynamic equilibrium is considered in the present case. Due to macrosegregation, the average composition is expected to continuously vary in time and space during casting. Transformation paths are thus determined a priori for a set of average compositions around the nominal value. Hence, carbon content varies in the interval [1.8 wt.%, 2.2 wt.%] while chromium content variation is in the interval [27 wt.%, 33 wt.%]. The offset of $\pm 10\%$ with respect to the nominal composition value allows tabulating relatively small composition steps to ensure a fairly accurate mapping when compared to the corresponding ternary phase diagram.

The average composition step is 0.04 wt.% for carbon and 0.6 wt.% for chromium, thus representing 2% intervals with respect to the nominal composition. The temperature varies in the interval [100 °C, 1600 °C] by 5 °C steps. For each triplet (carbon content in wt.% C, w_{C0} , chromium content in wt.% Cr, w_{Cr0} , temperature in K) corresponds a phase fraction g^ϕ and a pair of intrinsic phase composition ($\langle w_C \rangle^\phi, \langle w_{Cr} \rangle^\phi$), ϕ representing a phase. For the 5 phases listed in [fig. 2.7](#) (LIQ≡liquid, BCC≡ferrite, FCC≡austenite, M₇C₃≡carbide, CEM≡cementite), the enthalpy $\langle h \rangle^\phi$ and density $\langle \rho \rangle^\phi$, are tabulated as functions of temperature and phase intrinsic composition. If this lat-

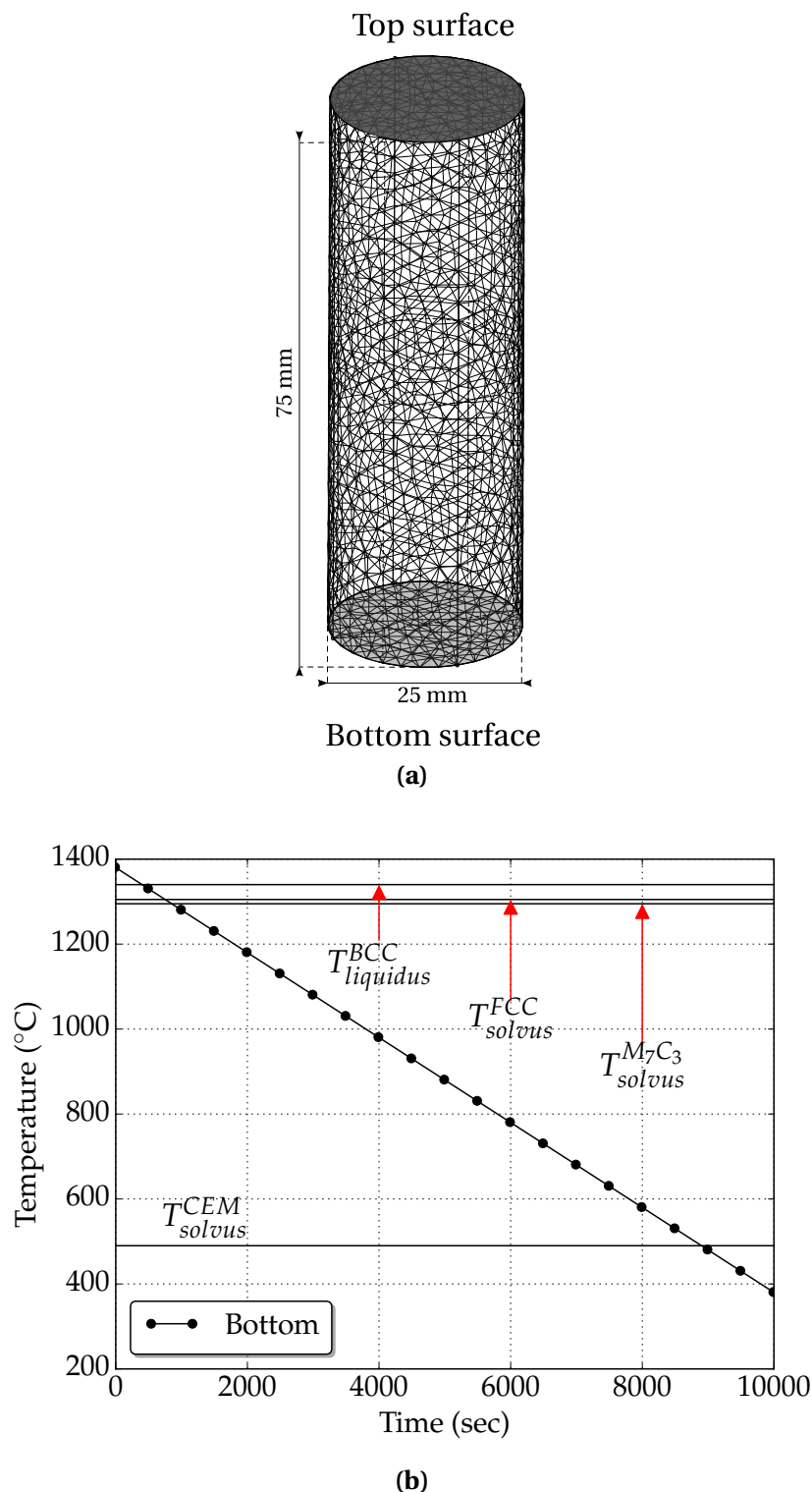


Fig. 2.6 – Configurations for upward directional casting of (a) a 1-inch diameter × 3-inches height cylindrical domain for which (b) temperature-time conditions are imposed at its bottom surface.

2.5. Application: multicomponent alloy solidification

ter input lies between two tabulated values, a linear interpolation is performed to determine the output, i.e. phase enthalpy and density. With the advancement of solidification, the liquid is enriched or depleted with solute by macrosegregation, which enables new solidification paths. It means that the primary solidifying phase is not necessarily the same as when considering the nominal composition. For this reason, the tabulation approach is interesting inasmuch as it provides phase transformation paths and values of phase properties that are compatible with the system's actual composition.

[Figure 2.8](#) summarises the tabulated thermodynamic data for two sets of average composition for the considered ternary system. Note that in the present test case, phase densities are taken constant ($\langle \rho \rangle^s = \langle \rho \rangle^l = 6725 \text{ kg m}^{-3}$). Therefore they are not tabulated. With this assumption, no shrinkage occurs upon phase change.

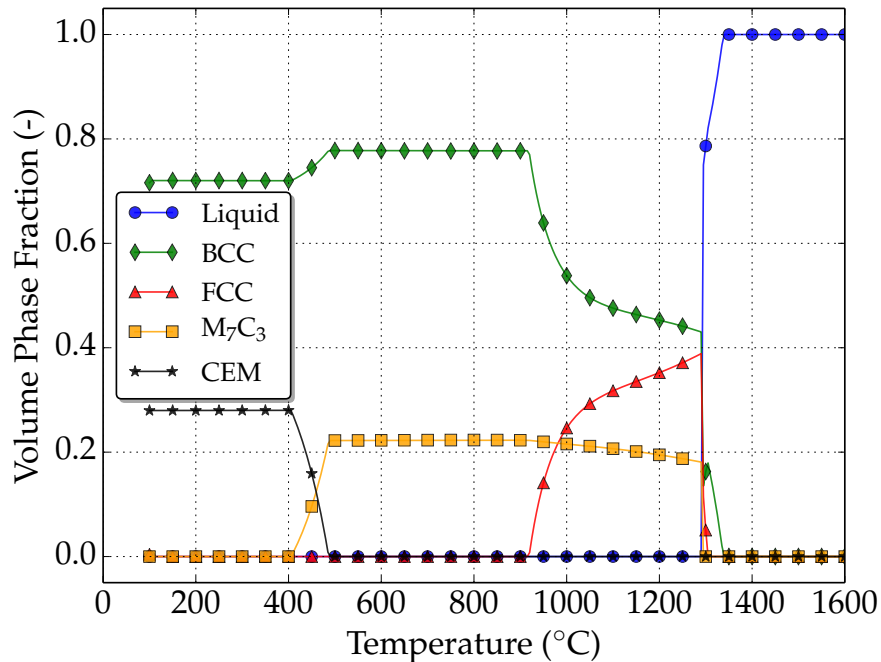


Fig. 2.7 – Thermodynamic mapping [TCFE6 2010; Andersson et al. 2002] of the transformation path for the Fe-2 wt.% C-30 wt.% Cr at nominal composition.

2.5.2 Discussion

A first case is considered without macrosegregation, that is, all mechanical driving forces are bypassed, leading to a static melt. This is achieved by nullifying the thermal and solutal expansion coefficients, which is equivalent to a constant density in space and time, i.e. no Boussinesq force is considered. This way, the average composition

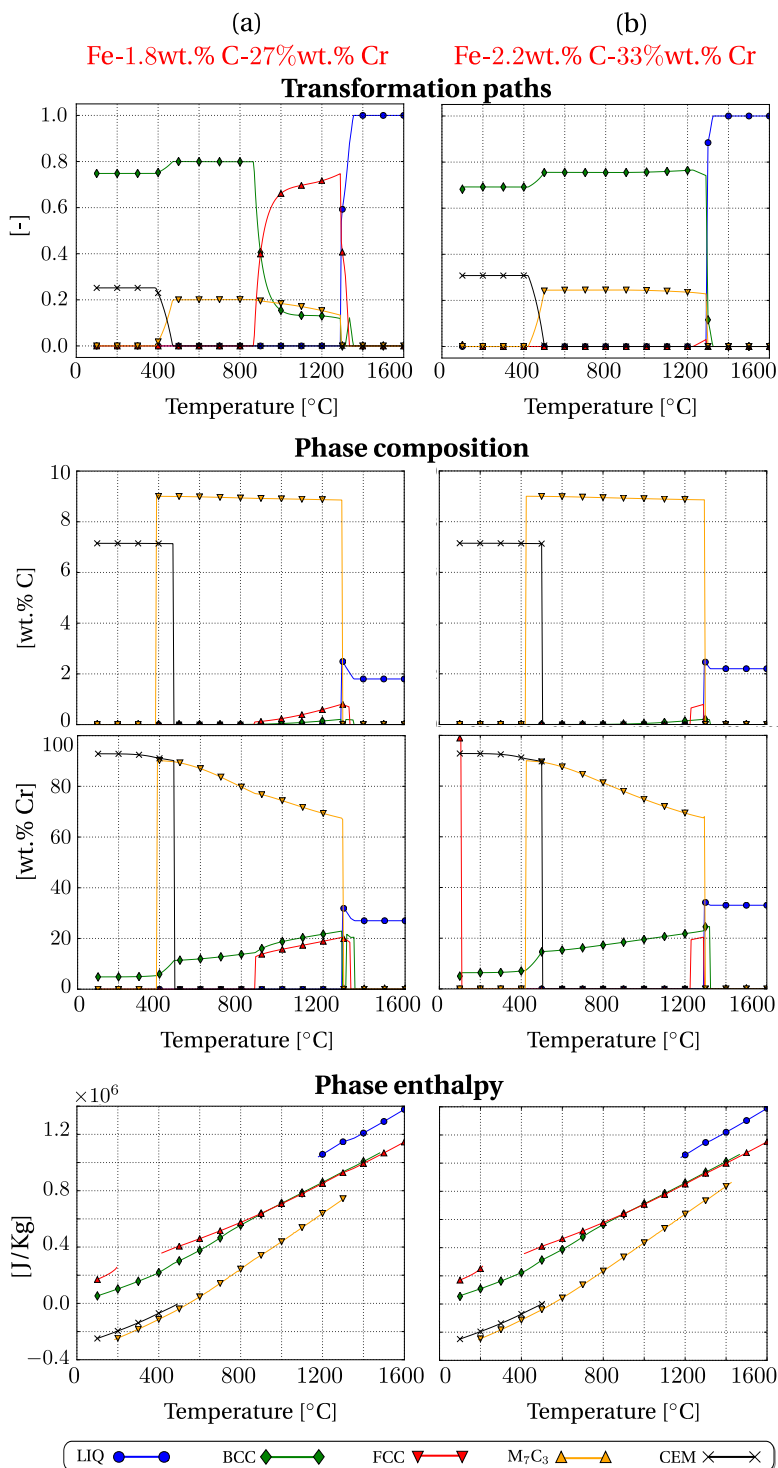


Fig. 2.8 – Tabulated thermodynamic data for the ternary system Fe-Cr alloy with software Thermo-Calc [Andersson et al. 2002] with database TCFE6 [TCFE6 2010]. The two columns represent two values of average composition, for a) low carbon and chromium content and b) high carbon and chromium content. The effect of their variation on transformation paths, phase compositions and phase enthalpies is shown in the corresponding graphs.

2.5. Application: multicomponent alloy solidification

may only vary due to diffusion in the liquid phase.

Diffusion is significantly small in the present case and can be neglected too. The composition distribution thus maintains a homogeneous aspect throughout the sample during the entire cooling sequence. The phase transformations then are necessarily expected to follow the unique path shown in [fig. 2.7](#). After 407 s of cooling, the liquidus isotherm enters the bottom surface of the geometry and starts its upward propagation, marking the solidification onset.

[Figure 2.9](#) presents the simulation results at 3 successive times for the distribution of the solute species and the temperature, as well as for the fraction of phases listed in [fig. 2.7](#). At 600 s, a fully liquid region is still largely present while the mushy zone is made of liquid plus the primary solid phase (ferrite). At 10 560 s, the sample is fully solid, with fractions of ferrite and cementite that corresponds to the values read in [fig. 2.7](#) at low temperature. At the selected intermediate time, the presence of 4 phases is found. The solid region at the bottom of the cylinder is made of ferrite, austenite plus carbide, the temperature being still too high to permit the cementite to form. The mushy zone above the solid region is characterized by the presence of 3 phases due to a peritectic reaction taking place that progressively transforms ferrite into austenite in the presence of liquid.

It can be noticed that the phase fraction isovales in [fig. 2.9](#) (at 600 s) are horizontal, owing this to two factors: the first is the temperature field, which varies unidirectionally from bottom to top, controlled by thermal diffusion, while the second is the uniform average composition throughout the sample due to the absence of convection. In fact both factors are consequences of the flow absence, which would transport heat and solute by advection, thus inevitably changing the phase distribution. The succeeding phase change is a solid-state transformation where α -ferrite and the carbide M_7C_3 react to form cementite after cooling below 490 °C, as shown in [fig. 2.6b](#). The reaction is relatively slow, ending with 28% of cementite and 72% of α -ferrite.

Chapter 2. Energy balance with thermodynamic tabulations

Table 2.3 – Solidification parameters for the Fe-2 wt.% C-30 wt.% Cr alloy.

Parameter	Symbol	Value	Unit
Nominal composition	w_{C0}	2	wt.%
	w_{Cr0}	30	wt.%
Characteristic temperatures	T_{bottom}	fig. 2.6b	°C
Phase fraction	g^ϕ	Tabulations fig. 2.8	–
Phase enthalpy	$\langle h \rangle^\phi$	Tabulations fig. 2.8	–
Phase composition	$\langle w_C \rangle^\phi$	Tabulations fig. 2.8	wt.%
Phase composition	$\langle w_{Cr} \rangle^\phi$	Tabulations fig. 2.8	wt.%
Diffusion coefficients	$\langle D_C \rangle^l$	15×10^{-10}	$\text{m}^2 \text{s}^{-1}$
	$\langle D_{Cr} \rangle^l$	15×10^{-10}	$\text{m}^2 \text{s}^{-1}$
Dynamic viscosity	μ^l	2×10^{-3}	Pa s
Thermal expansion coefficient	β_T	8.96×10^{-5}	K^{-1}
Solutal expansion coefficient	$\beta_{\langle w_C \rangle^l}$	1.54×10^{-3}	wt.\%^{-1}
	$\beta_{\langle w_{Cr} \rangle^l}$	1.72×10^{-2}	wt.\%^{-1}
Thermal conductivity in the solid	$\langle \kappa \rangle^s$	40	$\text{W m}^{-1} \text{K}^{-1}$
Thermal conductivity in the liquid	$\langle \kappa \rangle^l$	28	$\text{W m}^{-1} \text{K}^{-1}$
Dendrite arm spacing	λ	60×10^{-6}	m
Density	ρ_0^l	6725	kg m^{-3}
Reference composition (carbon)	$\langle w_C \rangle_{\text{ref}}^l$	2	wt.%
Reference composition (chromium)	$\langle w_{Cr} \rangle_{\text{ref}}^l$	30	wt.%
Reference temperature	$\langle w_C \rangle_{\text{ref}}^l$	1377	°C
Initial temperature	T_0	1395	°C
Ingot diameter		25×10^{-3}	m
Ingot length		75×10^{-3}	m
FE mesh size		10^{-3}	m
Time step	Δt	0.1	s
Convergence criterion (residual)	ε_R	10^{-6}	–
Convergence criterion (temperature)	ε_T	10^{-2}	K

2.5. Application: multicomponent alloy solidification

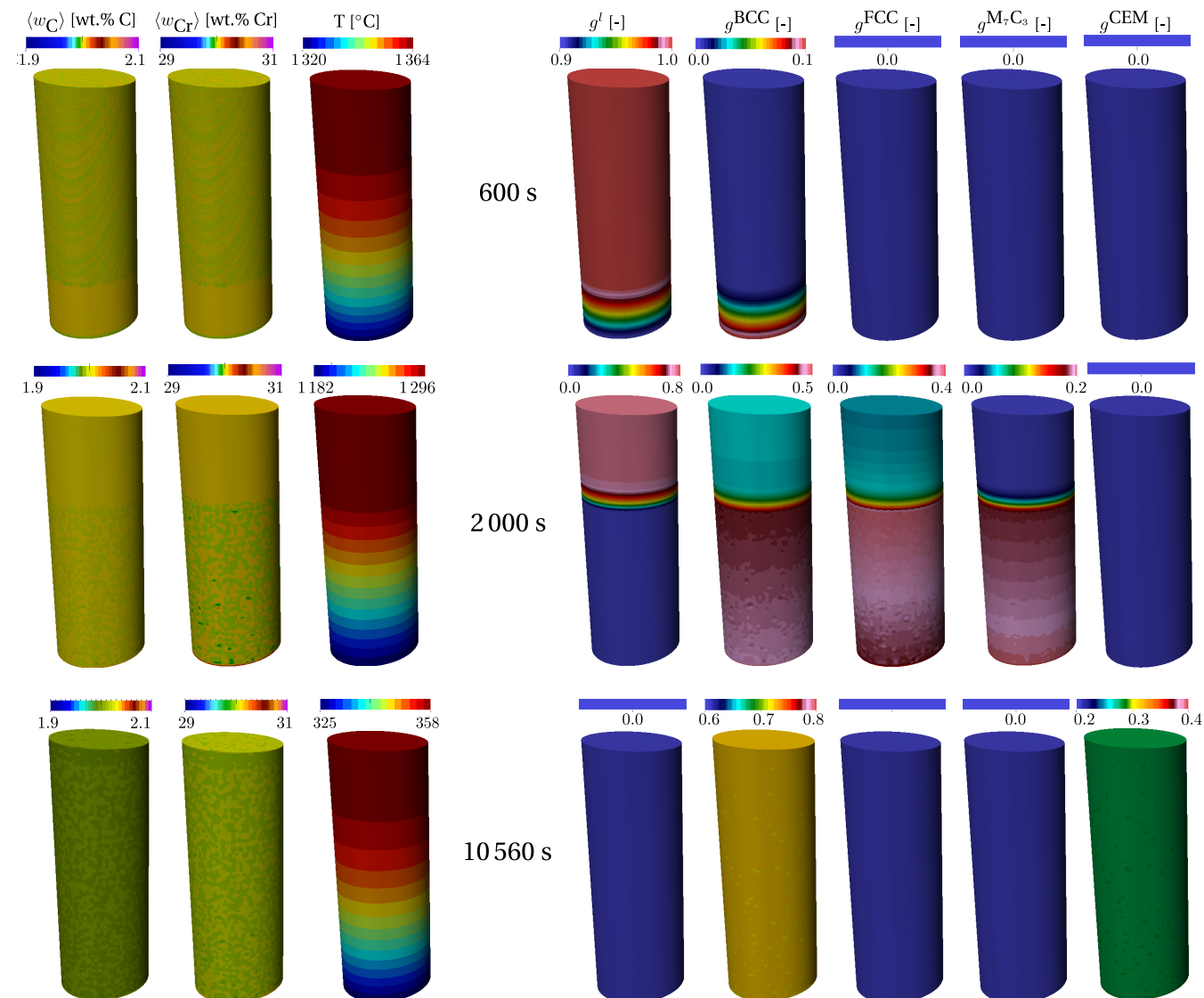


Fig. 2.9 – Upward solidification of a cylinder rod with a static liquid at 3 stages in a Fe-2 wt.% C-30 wt.% Cr. The left columns show the average composition and temperature distribution, while the right columns show the phase fractions.

2.6 Limitations

The *Tsolver* method is well suited for solidification problems with macrosegregation. In this chapter, only pure diffusion cases were simulated. The next chapter discusses the details of solving Navier-Stokes equations while predicting macrosegregation, showing thus the advantage of using the thermodynamic tabulation approach with the *Tsolver*. However, some limitations are still present and need to be explained.

First, we address the technical difficulties inherent to the solver. The previously shown algorithm in [fig. 2.4](#), showed that the Newton-Raphson method is used to linearise the energy equation then iterate on the value of the nonlinear term $\frac{\partial H}{\partial T}$. The initial value of this term is crucial to achieve a good convergence rate, and therefore it is only manually set equal to initial phases volume heat capacity. This should evolve into an automatic initialisation based on a first evaluation given by the tabulation, making the approach more general.

The second point is the number of iterations needed by the method to converge. Although the Newton-Raphson algorithm is known for its quadratic convergence speed, imposing low convergence thresholds ([eq. \(2.25\)](#)) may easily raise the number of iterations to an average of 5 iterations before convergence can be achieved. In situations without phase change but only variable slope of enthalpy versus temperature, from 1 to 2 iterations are needed to converge. A possible solution is to implement a line search method which is called at each iteration, whenever the residual of the non-linear system increases insteading of steadily decreasing. Moreover, since $\frac{\partial H}{\partial T}$ is a derivative which is based on ratio of finite differences for averaged volumetric enthalpy and temperature, [continue...](#)

Regarding the thermodynamic tabulations, they are only obtained by assuming full equilibrium for macrosegregation calculations. For many binary alloys, little differences are usually seen when the macrosegregation is induced by a full equilibrium and a non equilibrium solidification. It is clear however that this approximation remains limiting for multicomponent alloys. For steels, a third type of approximation is even required, named partial equilibrium, that considers equal chemical potential of interstitial elements in all phases (e.g., C), while substitutional species in the solid phases (e.g., Cr) are frozen [[Koshikawa et al. 2014](#)].

Résumé chapitre 3

Ce chapitre reprend les détails du solveur pour la conservation d'énergie avec changement de phase utilisé au CEMEF. Celui-ci est basé sur une méthode enthalpique, dénommée *Hsolver*, dont la variable principale est l'enthalpie moyenne volumique du système, $\langle \rho h \rangle$. Ce solveur est aussi compatible avec des données tabulées provenant de bases de données thermodynamiques, fournissant des valeurs précises pour chaque phase ϕ présente au moment de la transformation: fraction g^ϕ , composition intrinsèque $\langle w_i \rangle^\phi$, enthalpie massique $\langle h \rangle^\phi$ et densité $\langle \rho \rangle^\phi$. Avec ces données, l'équation de conservation de l'énergie est résolue dans son état nonlinéaire provenant de la dépendance de ρh par rapport aux propriétés citées précédemment, sachant que celles-ci varient aussi en fonction de la composition moyenne du volume élémentaire représentatif.

Cependant, la résolution *Hsolver* nécessite une lourde recherche itérative à chaque pas de temps, consistant à convertir $\langle \rho h \rangle$ en température T pour évaluer le résidu du système nonlinéaire. Cette conversion est dénommée *H2T* et elle est compliquée du fait que les bases thermodynamiques fournissent la température comme donnée d'entrée, ce qui nous oblige de faire la recherche inverse itérative.

Dans ce chapitre, on propose de remplacer la conversion *H2T* par une autre, *T2H*. Comme son nom l'indique, on part de l'idée que la température soit la variable principale du système et on devrait alors trouver l'enthalpie moyenne volumique à chaque pas de temps. Avec ce changement, on propose donc une nouvelle formulation éléments finis, *Tsolver*, mettant en évidence les principales différences algorithmiques des deux résolutions.

Nous validons la formulation *Tsolver* dans un cas purement diffusif et comparé à des calculs faits avec la méthode *Hsolver*, ainsi qu'une comparaison avec une solution numérique obtenue par une méthode de suivi de front [Gandin 2000]. Ensuite, nous montrons une application de solidification dirigée d'un système ternaire, Fe-0.2 wt.% C-30 wt.% Cr, en régime diffusif. Enfin, les limitations et les voies d'évolutions de la méthode *Tsolver* avec les tabulations sont détaillées.

Chapter 3

Macrosegregation with liquid metal motion

Contents

3.1	Introduction	47
3.2	Formulation stability	47
3.2.1	Stable mixed finite elements	47
3.2.2	Variational multiscale (VMS)	48
3.3	Navier-Stokes solver	49
3.3.1	Strong and weak formulations	49
3.3.2	Stabilisation parameters	53
3.3.3	Implementation	54
3.4	Application to multicomponent alloys	55
3.4.1	<i>Tsolver</i> validation with fluid flow	55
3.4.2	Results	58
3.5	Macroscopic prediction of channel segregates	63
3.5.1	Introduction	63
3.5.2	Experimental work	64
3.5.3	Macroscopic scale simulations	64
3.6	Meso-Macro prediction of channel segregates	74
3.6.1	Numerical method	74
3.6.2	Configuration	75
3.6.3	Effect of vertical temperature gradient	79
3.6.4	Effect of cooling rate	81
3.6.5	Effect of lateral temperature gradient	83

Chapter 3. Macrosegregation with liquid metal motion

3.6.6 Mono-grain freckles	84
-------------------------------------	----

3.1 Introduction

Fluid flow is an important part in understanding the evolution of an alloy system undergoing phase change. It is attributed to the convective transport in fluids where the time scale is much smaller than other transport mechanisms (e.g. diffusive transport). To understand how fluid motion contributes to the heat and mass transfer, we have swiftly presented the momentum conservation equation in a solidifying liquid, ?? . In this chapter, we will first give quick overview of the numerical treatment of this system of Navier-Stokes equations, then comment on some computational aspects such as the choice of a suitable time step and the conditions that impose minimum and maximum bounds on both time step and mesh size. Then, we shall present solidification applications where macrosegregation is mainly induced by thermosolutal convection.

3.2 Formulation stability

A wide array of numerical methods can be used to solve systems like ?? . When speaking about Navier-Stokes equations, the choice can be narrowed to two famous approaches with some similarities: stable mixed finite element method and Variational MultiScale (VMS) method. When two finite element spaces are introduced (e.g. one for velocity and another for pressure), the essential *inf-sup* condition (also known as stability condition) determined by Babuška [1971] and Brezzi [1974] should be fulfilled. It states that the formulation is ill-posed if the both spaces have the same interpolation order. For instance, a P1/P1 element (i.e. P1 for velocity / P1 for pressure) cannot guarantee the stability of the Navier-Stokes solution since velocity and pressure are both linearly interpolated at the simplex vertices. However, the major difference between the previously mentioned formulations is the way in which the inf-sup condition is accounted for. Stable mixed finite elements are stable because they directly respond to the stability condition by enriching the velocity space, hence they fall under the category of Satisfying Babuška-Brezzi (SBB) methods. In contrast, methods like VMS belong to the Circumventing Babuška-Brezzi (CBB) category [Barbosa and Hughes 1991]. CBB methods rely on equal-order interpolations with additional stabilisation that circumvents the need to satisfy the stability condition. Further details about both formulation types are given in the next subsections.

3.2.1 Stable mixed finite elements

First introduced by Arnold et al. [1984], the MINI element is the key ingredient of this approach. This type of element introduces an additional degree of freedom for the

velocity field while keeping a linear interpolation for the pressure field, thus satisfying the Babuška-Brezzi condition with a richer velocity space. The additional degree, known as the *bubble* function, vanishes on the element's boundary. We may therefore speak of a P1+/P1 finite element in a velocity-pressure formulation. This stable formulation has been the de facto standard for solving fluid and solid mechanics for many years at CEMEF.

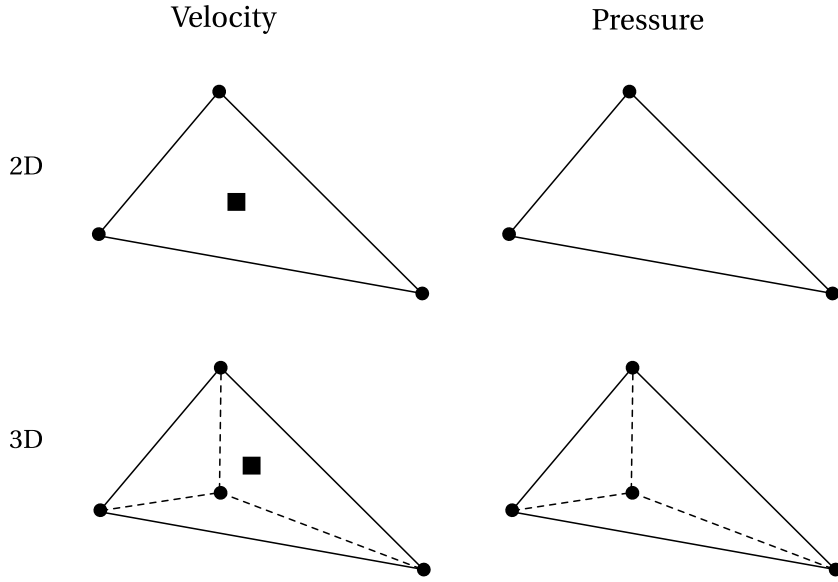


Fig. 3.1 – Schematic of 2D and 3D stable P1+/P1 finite elements, respectively triangle and tetrahedron, with velocity and pressure fields interpolation order. The dots represent the nodes while the squares represent the additional degrees, the *bubbles*.

3.2.2 Variational multiscale (VMS)

As the name indicates, this approach considers two scales of phenomena: the coarse and fine scales. Applied to a velocity-pressure formulation, these fields are decomposed according to these scales as follows:

$$\langle \vec{v}^l \rangle = \langle \vec{v}^l \rangle_h + \tilde{\vec{v}}^l \quad (3.1)$$

$$p = p_h + \tilde{p} \quad (3.2)$$

where $\langle \vec{v}^l \rangle_h$ and p_h are the coarse scale velocity and pressure discretised on the finite element mesh (hence the subscript h), while the remaining terms represent the fine scale velocity and pressure that cannot be captured at the scale of the FE grid. Instead of defining a finer grid to model the effect of these terms, one can solve the fine scale equations obtained once [eqs. \(3.1\) and \(3.2\)](#) are injected in ?? then use the output

in the coarse scale equations. Further technical details about the method and the equations are found in the PhD work of [Hachem \[2009\]](#).

The added value of the VMS method is the time gain that we get by incorporating the effect of the fine scale into the coarse scale physics without discretising on a finer grid, while maintaining the ability to predict localised fluid motion such as small vortices.

3.3 Navier-Stokes solver

In the present thesis, we chose to solve the fluid momentum conservation using a stabilised P1/P1 formulation with additional element-level integrals to add stability for convection-dominated terms, transient-dominated terms and pressure terms. The stabilisation techniques include the streamline upwind/Petrov-Galerkin (SUPG), pressure stabilising/Petrov-Galerkin (PSPG) and the least-squares on incompressibility constraint (LSIC) as a stabilisation framework introduced by [Tezduyar et al. \[1992\]](#). The global approach, more commonly known as SUPG-PSPG-LSIC, prevents the classical formulation instability coming from the linear equal-order interpolation functions.

It is important to note that the P1/P1 SUPG-PSPG-LSIC approach is slightly different than a VMS approach as the derivation of stabilising terms in the latter comes from a physical interpretation of two different length scales, a resolved coarse scale and an unresolved fine scale. The incorporation of the fine-scale equation within the coarse-scale one results in additional stabilising terms, while in the current approach these terms come from a mathematical analysis based on limiting cases of diffusion or advection. The final stabilising scheme is however very similar. The Navier-Stokes solver developed by [Hachem et al. \[2010\]](#) and [Rivaux \[2011\]](#) is a convenience choice to solve a stabilised Navier-Stokes system with Darcy terms.

3.3.1 Strong and weak formulations

The strong form of the fluid mechanics problem has been previously established in chapter 2 (??), where we obtained the following system of mass and liquid momentum

conservation equations:

$$\left\{ \begin{array}{l} \rho_0^l \left(\frac{\partial \langle \vec{v}^l \rangle}{\partial t} + \frac{1}{g^l} \vec{\nabla} \cdot (\langle \vec{v}^l \rangle \times \langle \vec{v}^l \rangle) \right) = \\ - g^l \vec{\nabla} p^l - \vec{\nabla} \cdot (2\mu^l \langle \vec{\varepsilon}^l \rangle) - g^l \mu^l \mathbb{K}^{-1} \langle \vec{v}^l \rangle + g^l \langle \rho \rangle^l \vec{g} \\ \nabla \cdot \langle \vec{v}^l \rangle = 0 \end{array} \right. \quad (3.3)$$

The strong solution consists of finding the pair $(\langle \vec{v}^l \rangle, p^l)$ of the previous system, when the following essential (Dirichlet type) and natural (Neumann type) boundary conditions are applied :

$$\langle \vec{v}^l \rangle = \vec{v}_0 \text{ on } \partial\Omega_{\text{Dirichlet}} \quad (3.4)$$

$$\langle \vec{\sigma}^l \rangle \cdot \vec{n} = \vec{N} \text{ on } \partial\Omega_{\text{Neumann}} \quad (3.5)$$

$$\text{with } \partial\Omega_{\text{Dirichlet}} \cup \partial\Omega_{\text{Neumann}} = \partial\Omega \quad (3.6)$$

We can comment on the strong form with the following recap points:

1. the liquid metal is Newtonian with a dynamic viscosity denoted μ^l
2. the metal is incompressible, therefore the liquid and solid densities are constant and equal (hence ρ_0^l in the inertial term) and the mass balance reduces to $\nabla \cdot \langle \vec{v}^l \rangle = 0$
3. the Boussinesq approximation is used to compute the thermosolutal buoyancy force in the melt via the term $g^l \langle \rho \rangle^l \vec{g} = g^l \langle \rho \rangle^l (T, \langle w_i \rangle^l) \vec{g}$, where $\langle \rho \rangle^l (T, \langle w_i \rangle^l)$ can be either tabulated as a function of temperature and liquid composition for each solute i , or directly approximated by:

$$\langle \rho \rangle^l = \rho_0^l \left(1 - \beta_T (T - T_0) - \sum_{i=1}^{\text{nb species}} \beta_{w_i^l} (\langle w_i \rangle^l - \langle w_i \rangle_0^l) \right) \quad (3.7)$$

where β_T and $\beta_{w_i^l}$ are respectively the thermal and solutal expansion coefficients, while T_0 and $\langle w_i \rangle_0^l$ represent a reference temperature and a reference liquid composition for each chemical species, respectively.

The weak form treated by the VMS solver derives from the strong form by multiplying

by test functions for velocity and pressure belonging to these functional spaces:

$$\begin{aligned} v &= \left\{ \vec{u}, \quad \vec{u} \in (\mathcal{H}^1(\Omega))^d \mid \vec{u} = \vec{v}_0 \text{ on } \partial\Omega \right\} \\ v^0 &= \left\{ \vec{u}, \quad \vec{u} \in (\mathcal{H}^1(\Omega))^d \mid \vec{u} = \vec{0} \text{ on } \partial\Omega \right\} \\ \varrho &= \{q, \quad q \in L^2(\Omega)\} \end{aligned}$$

where d stands for the space dimension. Then, based on these definitions, we write the advective upwinding stabilised test function for the velocity, \vec{U} :

$$\vec{U} = \vec{u} + \tau_{\text{SUPG}} \bar{\nabla} \vec{u} \cdot \left\langle \vec{v}^l \right\rangle_{\Omega_E} \quad (3.8)$$

τ_{SUPG} is an elemental stabilising parameter for advection-dominated terms and $\left\langle \vec{v}^l \right\rangle_{\Omega_E}$ is the superficial velocity in the element Ω_E , calculated by regular P1 interpolation:

$$\left\langle \vec{v}^l \right\rangle_{\Omega_E} = \frac{\sum_{i=1}^D \left\langle \vec{v}^l \right\rangle_i}{D} \quad (3.9)$$

Moreover, we need the following operators in order to simplify the notation of element-based variational integrals:

$$[a, b] = \int_{\Omega_E} ab \, d\Omega \quad (3.10)$$

$$[c, d]^* = \int_{\partial\Omega_E} cd \, d\Gamma \quad (3.11)$$

Chapter 3. Macrosegregation with liquid metal motion

Finally, the SUPG-PSPG-LSIC stabilised weak formulation writes:

$$\left\{ \begin{array}{l} \forall \vec{u} \in v^0 \\ \left[\left(\frac{\rho_0^l}{g^l} \frac{\partial \langle \vec{v}^l \rangle}{\partial t} \right), \vec{U} \right] + \left[\left(\frac{\rho_0^l}{g^{l2}} (\bar{\nabla} \langle \vec{v}^l \rangle) \langle \vec{v}^l \rangle \right), \vec{U} \right] + \left[\left(\frac{2\mu^l}{g^l} \right), \bar{\bar{\varepsilon}}(\langle \vec{v}^l \rangle) : \bar{\bar{\varepsilon}}(\vec{U}) \right] \\ + \left[(\mu^l \mathbb{K}^{-1} \langle \vec{v}^l \rangle), \vec{U} \right] - \left[(\langle \rho \rangle^l \vec{g}), \vec{U} \right] - [p, \nabla \cdot \vec{U}] - \left[\frac{\vec{N}}{g^l}, \vec{U} \right]^* \\ + [\tau_{\text{LSIC}}, (\rho_0^l \nabla \cdot \langle \vec{v}^l \rangle \nabla \cdot \vec{u})] = 0 \\ \\ \forall q \in \varrho \\ \left[\nabla \cdot \langle \vec{v}^l \rangle, q \right] + \left[\tau_{\text{PSPG}} \frac{\vec{\nabla} q}{\rho_0^l}, \left(\frac{\rho_0^l}{g^l} \frac{\partial \langle \vec{v}^l \rangle}{\partial t} + \frac{\rho_0^l}{g^{l2}} (\bar{\nabla} \langle \vec{v}^l \rangle) \langle \vec{v}^l \rangle + \mu^l \mathbb{K}^{-1} \langle \vec{v}^l \rangle - \langle \rho \rangle^l \vec{g} \right) \right] = 0 \end{array} \right. \quad (3.12)$$

Replacing eq. (3.8) in eq. (3.12), we get the final weak form:

$$\left\{ \begin{array}{l} \forall \vec{u} \in v^0 \\ \left[\left(\frac{\rho_0^l}{g^l} \frac{\partial \langle \vec{v}^l \rangle}{\partial t} \right), \vec{u} \right] + \left[\left(\frac{\rho_0^l}{g^{l2}} (\bar{\nabla} \langle \vec{v}^l \rangle) \langle \vec{v}^l \rangle \right), \vec{u} \right] + \left[\left(\frac{2\mu^l}{g^l} \right), \bar{\bar{\varepsilon}}(\langle \vec{v}^l \rangle) : \bar{\bar{\varepsilon}}(\vec{u}) \right] \\ + \left[(\mu^l \mathbb{K}^{-1} \langle \vec{v}^l \rangle), \vec{u} \right] - \left[(\langle \rho \rangle^l \vec{g}), \vec{u} \right] - [p, \nabla \cdot \vec{u}] - \left[\frac{\vec{N}}{g^l}, \vec{u} \right]^* \\ + \left[\tau_{\text{SUPG}} \bar{\bar{\nabla}} \vec{u} \cdot \langle \vec{v}^l \rangle_{\Omega_E}, \left(\frac{\rho_0^l}{g^l} \frac{\partial \langle \vec{v}^l \rangle}{\partial t} + \frac{\rho_0^l}{g^{l2}} (\bar{\nabla} \langle \vec{v}^l \rangle) \langle \vec{v}^l \rangle + \mu^l \mathbb{K}^{-1} \langle \vec{v}^l \rangle + \vec{\nabla} p^l - \langle \rho \rangle^l \vec{g} \right) \right] \\ + [\tau_{\text{LSIC}}, (\rho_0^l \nabla \cdot \langle \vec{v}^l \rangle \nabla \cdot \vec{u})] = 0 \\ \\ \forall q \in \varrho \\ \left[\nabla \cdot \langle \vec{v}^l \rangle, q \right] + \left[\tau_{\text{PSPG}} \frac{\vec{\nabla} q}{\rho_0^l}, \left(\frac{\rho_0^l}{g^l} \frac{\partial \langle \vec{v}^l \rangle}{\partial t} + \frac{\rho_0^l}{g^{l2}} (\bar{\nabla} \langle \vec{v}^l \rangle) \langle \vec{v}^l \rangle + \mu^l \mathbb{K}^{-1} \langle \vec{v}^l \rangle + \vec{\nabla} p^l - \langle \rho \rangle^l \vec{g} \right) \right] = 0 \end{array} \right. \quad (3.13)$$

3.3.2 Stabilisation parameters

Several expressions for τ_{SUPG} were derived by Tezduyar et al. [1992] and Tezduyar and Osawa [2000], from which we retain the following:

$$\tau_{\text{SUPG}} = \left(\frac{1}{\tau_{\text{advec}}^2} + \frac{1}{\tau_{\text{diff}}^2} + \frac{1}{\tau_{\text{trans}}^2} \right)^{-1/2} \quad (3.14)$$

where we use three parameters τ_{advec} , τ_{diff} and τ_{trans} having time as unit (*s*) that stabilise respectively advection-dominated, diffusion-dominated and transient-dominated regimes, given by:

$$\tau_{\text{advec}} = \frac{h_{\text{stream}}}{2\|\langle \vec{v}^l \rangle_{\Omega_E}\|} \quad (3.15)$$

$$\tau_{\text{diff}} = \frac{h_{\text{stream}}^2}{4\nu^l} \quad (3.16)$$

$$\tau_{\text{trans}} = \frac{\Delta t}{2} \quad (3.17)$$

where $h_{\text{stream}} = 2\|\langle \vec{v}^l \rangle_{\Omega_E}\| \left(\langle \vec{v}^l \rangle_{\Omega_E} \cdot \vec{\nabla} \mathcal{P} \right)$ is the element length in the stream direction, computed using the local superficial velocity and the interpolation functions \mathcal{P}_j relative to each local node j , ν^l is the liquid's kinematic viscosity ($\text{m}^2 \text{s}^{-1}$) and Δt is the time step. The transient term stabilisation was initially derived for Navier-Stokes equations without Darcy term. As the latter has a significant role in the weak form eq. (3.13), it needs to be stabilised. The current thesis is based on several past projects that either considered eq. (3.17) like Liu [2005] or modified it like Gouttebroze [2005] and Rivaux [2011] to take account the Darcy term, giving the term:

$$\tau_{\text{trans-darcy}} = \frac{\Delta t}{2 \left(1 + \Delta t \frac{\mu^l}{\rho_0^l \mathbb{K}} \right)} \quad (3.18)$$

In the literature, no substantial references were found to backup the formulation of eq. (3.18), it will be used in the current work though. It is worth mentioning that Zabaras and Samanta [2004] has invoked the necessity to stabilise Darcy terms in a generalised Navier-Stokes/Darcy P1/P1 formulation, and introduced what they call Darcy-Stabilising/Petrov-Galerkin (DSPG), using local non-dimensional numbers of Darcy (Da) and Prandtl (Pr) numbers expressing respectively the ratio of local permeability to a characteristic length L_c and the ratio of momentum diffusivity, ν^l , to heat

Chapter 3. Macrosegregation with liquid metal motion

diffusivity in the liquid, α^l :

$$\tau_{\text{darcy}} = \frac{Da}{Pr} \left(\frac{g^l}{1 - g^l} \right)^2 = \frac{\alpha^l \mathbb{K}}{\nu^l L_c^2} \left(\frac{g^l}{1 - g^l} \right)^2 \quad (3.19)$$

Last, the definitions of the remaining stabilisation parameters are given as follows:

$$\tau_{\text{PSPG}} = \tau_{\text{SUPG}} = \left(\left(\frac{2 \|\langle \vec{v}^l \rangle_{\Omega_E} \|}{h_{\text{stream}}} \right)^2 + \left(\frac{4 \nu^l}{h_{\text{stream}}^2} \right)^2 + \left(\frac{2 \left(1 + \Delta t \frac{\mu^l}{\rho_0^l \mathbb{K}} \right)}{\Delta t} \right)^2 \right) \quad (3.20)$$

$$\tau_{\text{LSIC}} = \frac{h_{\text{stream}}}{2} \|\langle \vec{v}^l \rangle_{\Omega_E} \| Z(Re_{\Omega_E}) \quad (3.21)$$

with $Z(Re_{\Omega_E})$ being a local Reynolds-dependant function that evaluates to:

$$Z(Re_{\Omega_E}) = \begin{cases} Re_{\Omega_E}/3 & \text{if } Re_{\Omega_E} \leq 3 \\ 1 & \text{if } Re_{\Omega_E} > 3 \end{cases} \quad (3.22)$$

and

$$Re_{\Omega_E} = \frac{\|\langle \vec{v}^l \rangle_{\Omega_E} \| h_{\text{stream}}}{2 \nu^l} \quad (3.23)$$

3.3.3 Implementation

The final matrix definition of the weak form of eq. (3.3) is given by:

$$\begin{pmatrix} A_{vv} & A_{vp} \\ A_{pv} & A_{pp} \end{pmatrix} \begin{pmatrix} \langle \vec{v}^l \rangle \\ p^l \end{pmatrix} = \begin{pmatrix} B_v \\ B_p \end{pmatrix} \quad (3.24)$$

CFL condition

Integration order

Using P1 linear elements implies a P2 integration ? what are the advantages (time) and limitations ?

3.4 Application to multicomponent alloys

3.4.1 *Tsolver* validation with fluid flow

To validate the *Tsolver* with fluid flow, we consider the following set of equations already defined in the flowchart of ???. Moreover, an assumption of a static and non deformable solid phase is made. Consequently, the mechanical model is reduced to the conservation of momentum in the liquid phase.

The *Tsolver*'s ability to be coupled with various physical phenomena like macrosegregation and fluid flow in porous medium is validated using an experimental solidification benchmark. The validation case consists of a 10 cm width \times 6 cm height \times 1 cm thick crucible containing a Sn-3 wt.% Pb melt. The alloy is cooled down from its two narrowest vertical sides using heat exchangers (LHE: left heat exchanger, RHE: right heat exchanger). The experiment, inspired by [Hebditch and Hunt \[1974\]](#) similar set up, has been revisited by [Hachani et al. \[2012\]](#) who performed the solidification with better controlled conditions and using an increased number of samples for composition analysis. Recently, a successful attempt to simulate the experiment was carried out by [Carozzani et al. \[2013\]](#) relying on an enthalpy resolution. All details regarding geometry, finite element discretization, material properties and boundary conditions can be found in the latter reference.

For this computation, solidification paths, phase compositions and phase enthalpies were determined by a thermodynamic module dedicated to equilibrium calculations for binary alloys. The 3D simulation results in [fig. 3.2](#) show a satisfactory agreement with the experimental temperature measurements recorded at mid-heights of the cavity and uniformly distributed along its width.

Furthermore, simulation results with the *Tsolver* and the *Hsolver* previously obtained by [Carozzani et al. \[2013\]](#) were found to be almost superimposed. This is confirmed by a comparison made between both solvers, as shows [fig. 3.3](#), where the average composition, liquid fraction and temperature fields are extracted from a cut plane halfway through the ingot. On the same figure, if we compare the composition, we notice that the solidified part on the RHE side has basically the same segregation pattern, while the convected liquid has a slightly different solute distribution.

As for the extent of the mushy zone, we observe that liquid fraction contours are very close, indicating that temperature distributions and interdendritic segregation are also close between both solvers predictions.

Regarding the computation, the *Tsolver* resolution proves to be faster than the *Hsolver* used by [Carozzani et al. \[2013\]](#): a process time of 7000 s required a computation time of 90 hours 13 minutes compared to 114 hours 21 minutes spent by the enthalpy

resolution with 32 cores on the same cluster. The gain factor is about 20%.

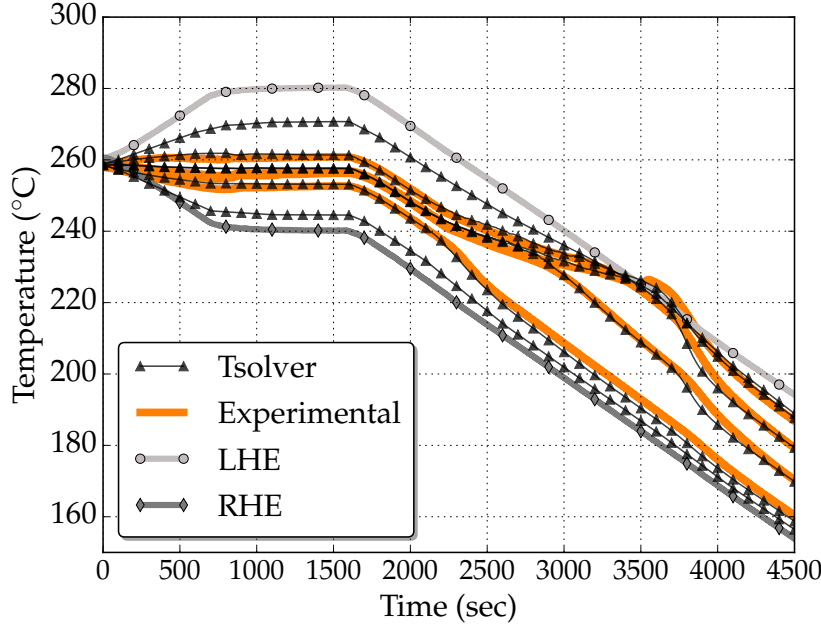


Fig. 3.2 – Results of the 3D FE convection-diffusion simulation, overlapping with the experimental cooling curves. The left (LHE) and right (RHE) heat exchangers impose the boundary temperature in the experiment.

In the previous chapter, we have considered a static melt upon solidification of multi-component alloy. The artificial consideration of a still flow is dropped in this chapter, hence taking into account solute transport caused by fluid motion, using realistic values of the expansion coefficients given in [table 2.3](#). In the real conditions, the melt is in constant motion and knowing that the carbon and chromium solutes have lightening effects on the liquid at nominal composition, the density inversion resulting from the composition gradient in the interdendritic liquid, may cause flow instability (segregation plumes) at the solidification front. While the selected alloy is a steel, this application is also representative of directional cooling in a single crystal casting, e.g. for nickel-base superalloys [[Beckermann et al. 2000](#)]. Solidification of this class of alloys is carefully controlled so as to prevent any freckle-type defect to exist in the as-cast state. In this section, we consider the same simulation parameters defined in [table 2.3](#) as well as the geometry and thermal boundary conditions previously defined in [fig. 2.6](#). Moreover, we solve the liquid momentum conservation equation, with non-slip boundary conditions on all external sides of the cylinder.

3.4. Application to multicomponent alloys

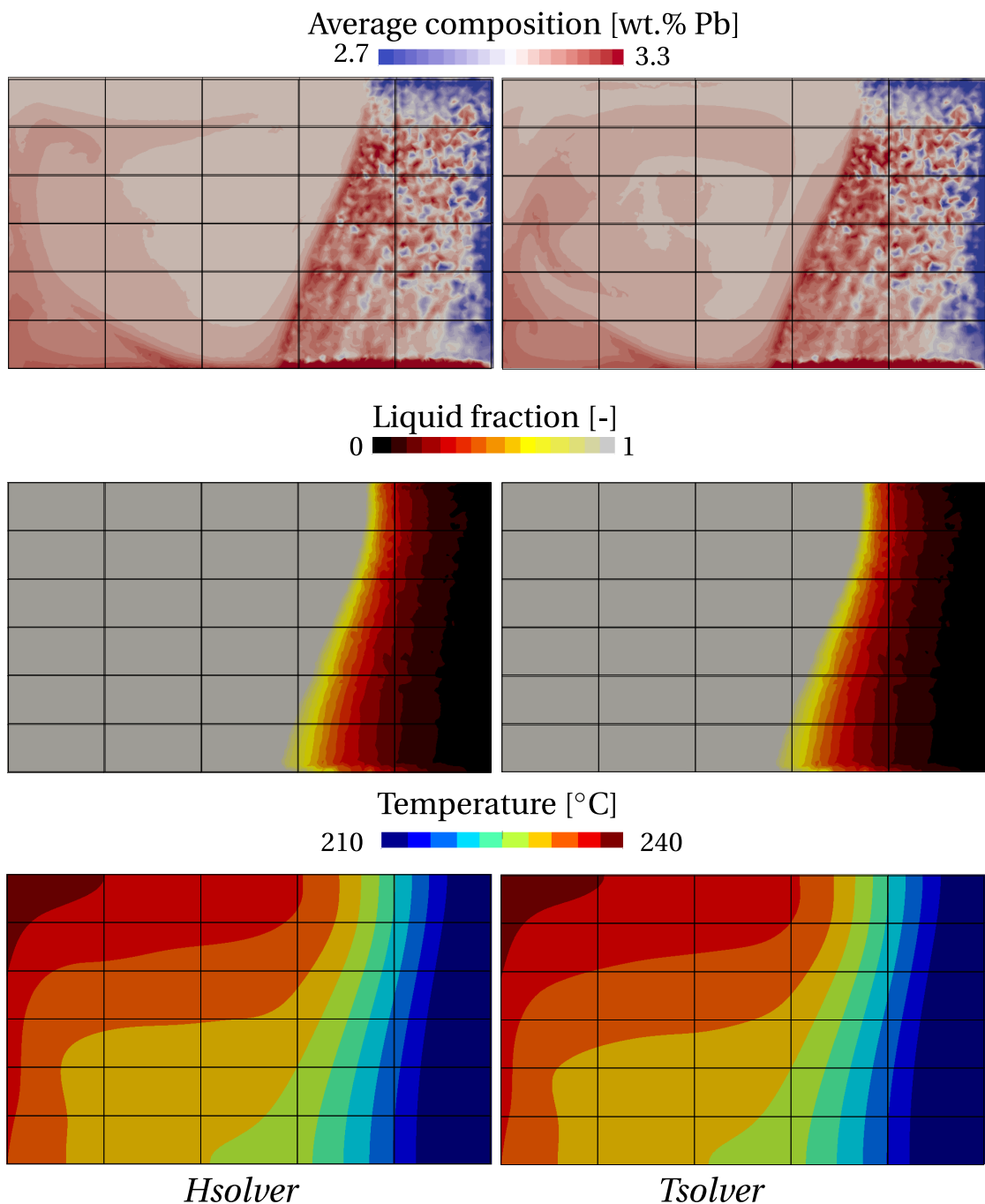


Fig. 3.3 – Comparison of 3D simulation results: average composition, liquid fraction and temperature at $t=3000$ s for *Tsolver* and *Hsolver*.

3.4.2 Results

Solidification starts at 407 s when the cylinder's bottom base temperature reaches the liquidus temperature of the alloy. In fact, the solidification onset is the same as in the pure diffusion case in [fig. 2.9](#), since the average composition remains unchanged for an entirely liquid domain (assuming an initially infinite solute mixing in the melt).

As shown in [fig. 3.4](#) at 600 s, the first solid phase to form remains ferrite. We can also see solute-rich channels forming in the mushy zone and solute plumes rising in the melt above the mushy zone due to a subsequent upward flow. It is actually caused by the thermosolutal buoyancy force created by the carbon and chromium solutes. Such phenomenon delays solidification inside the liquid-rich channels and could result in freckling defects [[Felicelli et al. 1991](#)] on the surface of the cylinder as well as inside, as shown later in this section. As solidification proceeds, the liquid becomes more enriched with solute and the peritectic reaction forming the austenite phase is reached. However, for very large enriched melt, it can also be observed that primary solidification proceeds with the austenite phase rather than the ferrite phase. The carbide phase can form with the austenite phase at some locations. These observations correspond to a simulation time of 2000 s in [fig. 3.4](#).

Solidification ends at around 2475 s, the last liquid solidifying at the cylinder's top surface, where the average composition reaches a maximum of Fe-2.151 wt.% C-30.633 wt.% Cr, i.e. a relative positive macrosegregation, $(\langle w_i \rangle - \langle w_i \rangle_0) / \langle w_i \rangle_0$, of 7.5% for carbon and 2.1% for chromium. The fact that the maximum average composition is observed at the top, is verified in [fig. 3.5a](#) which shows the composition map in a 2D vertical slice through the longitudinal axis of the cylinder. We can also see it in [fig. 3.5b](#) where the relative composition profile are plotted at the end of the cooling process along the longitudinal cylinder axis Z-Z' and along the axis of the segregated channel, F-F'. Segregation becomes more and more negative up to 1 cm from the chill, corresponding to solute depletion caused by the first solid formation. Subsequent solidification enriches further the liquid; hence the solid composition also increases.

The composition evolution trend for both solutes is similar: an overall rise until positive segregation is achieved above 5 cm from the chill on ZZ' in [fig. 3.5b](#). The positive macrosegregation intensifies when the profile is chosen at the center of the segregated channel, negative segregation then becoming less pronounced.

3.4. Application to multicomponent alloys

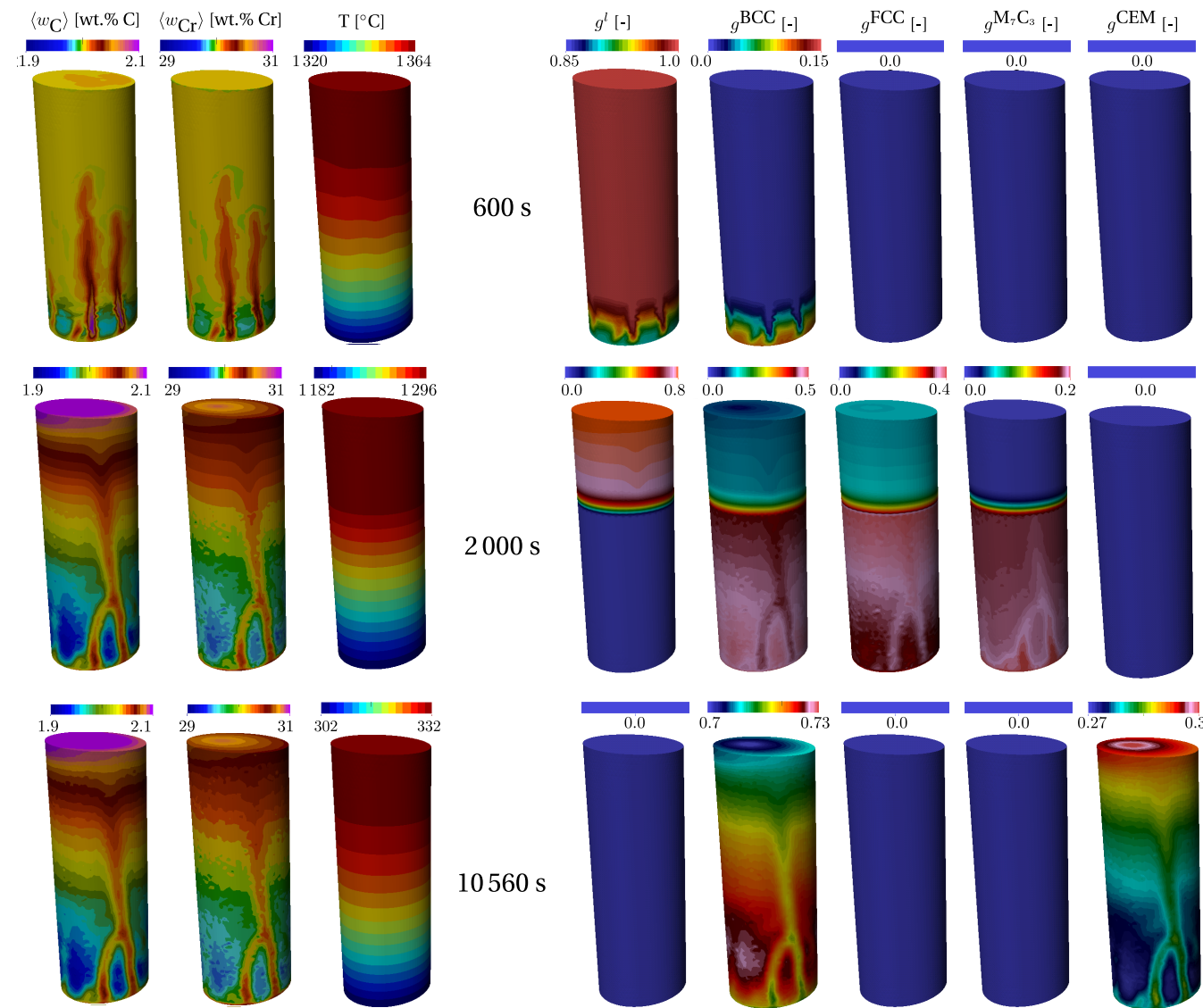


Fig. 3.4 – Upward solidification of a cylinder rod at 3 stages showing the metallurgical consequences of macrosegregation Fe-2 wt.% C-30 wt.% Cr. The left columns show the average composition and temperature distribution, while the right columns show the phase fractions.

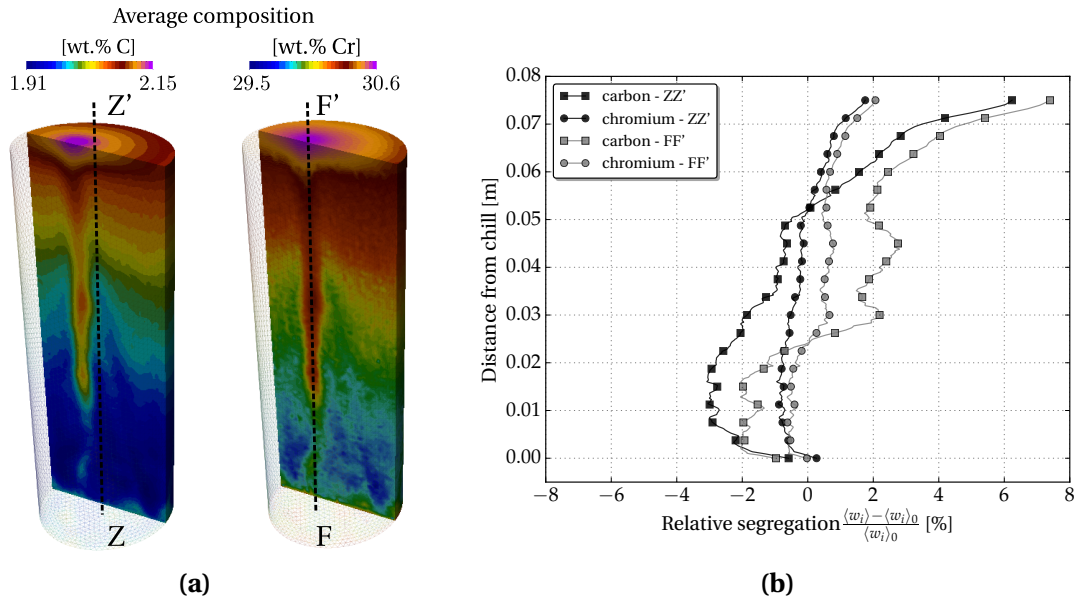


Fig. 3.5 – (a) average composition map on a vertical section inside the sample, with (b) relative macrosegregation profiles on the vertical revolution axis.

Beyond 2475 seconds, no variations of the average composition maps are observed since solidification is complete. Nonetheless, as temperature decreases, solid-state transformations are still possible as for the case with no macrosegregation. The formation of a cementite phase begins at the cylinder base at 8843 s with a temperature of 496.9 °C. At about 9293 s, the isotherm 488.5 °C reaches the top surface. This temperature value is the local cementite solvus temperature. The difference in the solvus temperature between the bottom and top surfaces is due macrosegregation. Macrosegregation also explains the variation in the cementite content. The solid state transformation ends shortly before 10 500 s. The influence of the solidification process is clear on the final macrosegregation pattern, hence the final phase distribution. This is better illustrated by drawing the time evolution of phase fractions at the center of the bottom and top surfaces of the cylinder in fig. 3.6. With no macrosegregation, in ??, the final distribution of the phases is the same at time 12 000 s, while with macrosegregation, in ??, variations of the cementite and ferrite are revealed. The segregated channels inside the cylinder and on the boundary, often lead to *freckles*, where they consist of visible equiaxed grains [Copley et al. 1970]. This defect is marked by a noticeable gradient of composition and phase fractions, possibly changing the mechanical properties in the channels, hence the overall mechanical behaviour of the cast part. The coupling of the *Tsolver* with thermodynamic tabulations is thus demonstrated. It shows the ability to predict complex transformation paths, even if only at equilibrium. As for the computation time, the *Tsolver* resolution performed better: 500 seconds of

3.4. Application to multicomponent alloys

solidification required 6 hours 14 minutes compared to 8 hours 6 minutes spent by the enthalpy resolution with 12 cores on the same machine. The gain factor is about 22%.

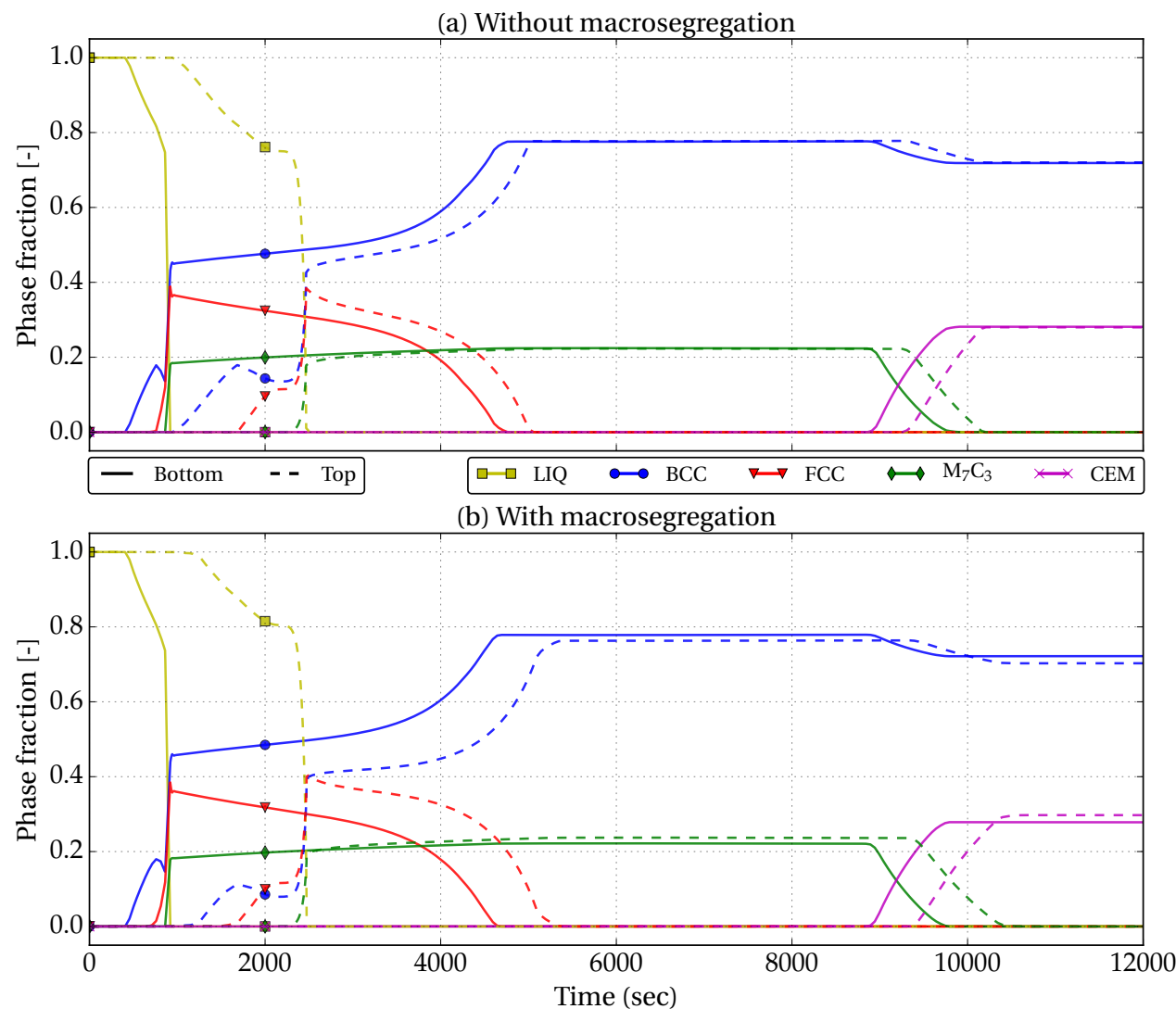


Fig. 3.6 – History of phase fraction (a) without macrosegregation and (b) with macrosegregation at the center of the bottom (solid lines) and top (dashed lines) of the cylinder surfaces. These plots are extracted from simulations displayed in (a) [fig. 2.9](#) and (b) [fig. 3.4](#).

3.5 Macroscopic prediction of channel segregates

3.5.1 Introduction

We have seen in the previous multicomponent solidification test case, a formation of segregated channels in the cylinder. This defect manifests itself as a composition inhomogeneity that is highly non-isotropic. A typical description of its morphology would consider a channel with a diameter proportional to few primary dendrite arm spacing and a length that could vary from millimeters to centimeters. These “worm”-like shapes could form during directional solidification of cast parts designed for engine applications, particularly in Nickel-base superalloys [Giamei and Kear 1970; Becker-mann et al. 2000; Genereux and Borg 2000; Schneider et al. 1997]. In the latter situation, the channels are filled with a chain of small equiaxed crystals, thus referring to the term “freckle”. In large steel ingots, these channel defects are also related to A- and V-segregates [Pickering 2013].

Considering a binary alloy with a partition coefficient less than unity and having a negative liquidus slope, channel segregates may form by the following mechanisms: i) solute partitioning occurs at the scale of dendrite arms and solute is rejected in the melt, ii) local composition gradients are intensified resulting in an increase of the solutal buoyancy force in the mushy zone, iii) solute-rich pools are formed, causing segregation chimneys and convective plumes in the melt, iv) which lead to partial remelting and transport of dendrites, continuous solute feeding and locally delayed solidification, and finally v) accumulation of fragments and/or equiaxed crystals in the chimneys before the end of solidification.

Because it is of prime importance to control the occurrence of channel segregation, several attempts have been made from the late 1960's [Flemings and Nereo 1967; Flemings et al. 1968; Flemings and Nereo 1968] to the early 2000's [Ramirez and Becker-mann 2003] to understand it and characterise it by deriving freckling criteria. These studies are summarized in [Auburtin 1998]. One of the reasons for only considering freckling criteria is that direct realistic simulations of the formation of freckles in a casting geometry are still difficult. Indeed, experimental observations show that it requires a satisfying description of the microstructure together with the 3D convective flow controlled by the cooling conditions of the complete cast part [Shevchenko et al. 2013]. Such information is not accessible yet. Only simulations in representative simple cuboid or cylindrical domains are usually achieved [Felicelli et al. 1991; Felicelli et al. 1998; Kohler 2008; Guo and Beckermann 2003], except when considering small volume casting [Desbiolles et al. 2003]. They are usually limited to unstable thermosolutal convection without or with little regard to the microstructural features.

Considering the spatial resolution of the defect, being for example of the order of the primary dendrite arm spacing, a fluid flow computation in the 3D casting part is also very demanding and not common in the literature. Among other criteria, the dimensionless Rayleigh number has been identified as a good indicator for the occurrence of segregation channels and freckle defects. The dependence of freckling tendency on the Rayleigh number has been studied numerically and compared to experimental observations, as done by [Ramirez and Beckermann 2003].

3.5.2 Experimental work

An interesting experimental work on directional solidification of In-75 wt.% Ga featuring in-situ X-ray monitoring has been recently carried out by Shevchenko et al. [2013]. The comparison with numerical modelling is paramount for two main reasons: firstly, the in-situ technique allows to follow solidification in real-time and offers visual description of the system behaviour: grain morphology, composition evolution, effect on fluid flow in the mushy zone and chimney initiation, as well as other modelling input data such as dendritic and eutectic nucleation undercooling; secondly, an indium-gallium system is more representative of metallic alloy solidification than the widely used organic systems, e.g. the succinonitrile-acetone mixture that exhibits alloy-like dendritic formation in its growth stage. Further information with respect to the experimental hardware, procedure and data analysis can be found in [Boden et al. 2008; Shevchenko et al. 2013].

3.5.3 Macroscopic scale simulations

Configuration

The focus of this section is on qualitative comparison between numerical simulation and the previously mentioned experiment. The experimental cell geometry shown in fig. 1.7c is hexagonal. With adiabatic lateral sides, it results in a bending of the isotherm surfaces as shown in the experiment. The metallic cooling plates shown in fig. 3.7a partly compensate for this effect. However, a residual horizontal component of the temperature gradient remains.

To qualitatively replicate this effect while simplifying the cell geometry, a $22\text{ mm} \times 22\text{ mm} \times 1\text{ mm}$ cuboid cell is considered with small cooling fluxes on its lateral vertical side surfaces computed using a constant heat transfer coefficient, h_{ext} , and a constant environment temperature, T_{ext} , as shown in fig. 3.8. On the same figure, temperatures at the bottom and top surfaces, respectively T_{Top} and T_{Bottom} , are imposed in a way to maintain a constant vertical gradient, \vec{G} , thus linearly decreasing over time with the same cooling

3.5. Macroscopic prediction of channel segregates

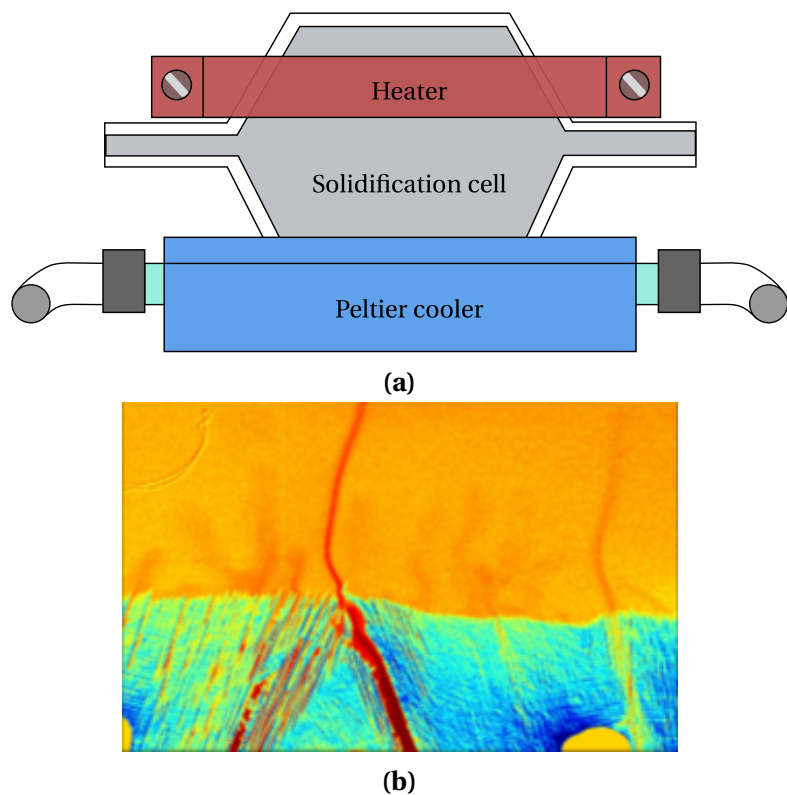


Fig. 3.7 – Illustration of the benchmark experiments for in-situ observation of segregated channels formation using X-Ray radiography with (a) a schematic of the cell and (b) a typical image of the microstructure formed during directional solidification of an In-75 wt.% Ga alloy.

Chapter 3. Macrosegregation with liquid metal motion

rate R . Both square faces of the geometry, having an area of $22\text{ mm} \times 22\text{ mm}$, are adiabatic. In spite of taking cell dimensions similar to benchmark experiments presented above, the cell thickness is increased from $150\text{ }\mu\text{m}$ to 1 mm . One of the main obstacles of simulating a $150\text{ }\mu\text{m}$ -thick cell is the number of elements in the thickness. An insufficient number may lead to incorrect velocity computation in the cell thickness, resulting in inaccurate channel segregation prediction. In general, a number around 5 to 8 elements is needed to get a better representation of the fluid motion. When the domain thickness is $150\text{ }\mu\text{m}$, imposing 8 elements in the thickness results in a huge homogeneous isotropic mesh containing about 10^9 elements, the mesh size being equal to 0.018 mm . For now, this would only lead to slower simulations and therefore more complicated analysis with the large data files. Instead, we choose to keep the same number of thickness elements, but increase the thickness instead. That way, the resulting isotropic mesh would reduce to 2.5×10^4 elements. Therefore, we keep the latter thickness as the current study is limited to qualitative comparisons, but the mesh size is imposed to about $2\lambda_2=140\text{ }\mu\text{m}$, and the fixed finite element grid contains around 2×10^6 elements and 3×10^5 degrees of freedom.

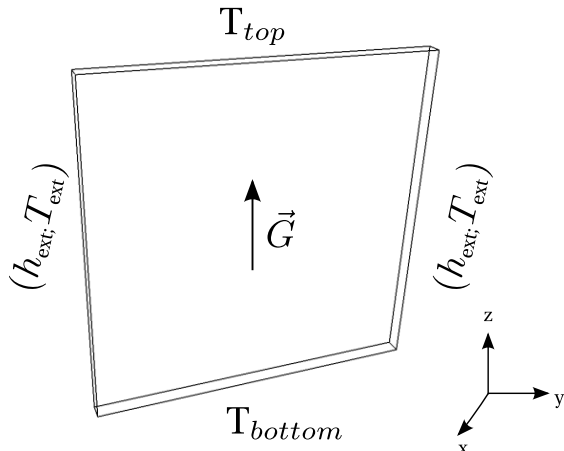


Fig. 3.8 – Computational geometry used for simulating channel segregation phenomena, along with top and bottom imposed boundary temperatures, T_{Top} and T_{Bottom} , and lateral Fourier cooling fluxes using a heat transfer coefficient and an external temperature, h_{ext} and T_{ext} . The resulting temperature gradient, \vec{G} , is parallel to the vertical z -axis.

Materials properties are provided in [table 3.2](#) while initial and boundary conditions are given in [table 3.1](#). A series of computations is performed to understand the influence of process parameters on the final macrosegregation pattern. In directional growth, the main parameters are the vertical temperature gradient, \vec{G} , and the cooling rate, R , since they control the isotherms speed. However, the effect of a higher lateral cooling is also considered below by increasing the heat transfer coefficient, h_{ext} . Finally, the grain structure is another crucial parameter that drastically changes the analysis inasmuch

3.5. Macroscopic prediction of channel segregates

Table 3.1 – Summary of the simulations and the corresponding parameters for the FE cases, where a purely macroscopic model is used. Parameters are varied from (G1) low to (G2) high gradient and (L0) no, to (L1) low lateral cooling.

Case	Vertical gradient	Cooling rate	Lateral cooling	Initial temperature
	$\ \vec{G}\ $ [K mm $^{-1}$]	R [K s $^{-1}$]	L ($h_{\text{ext}}, T_{\text{ext}}$) [W m $^{-2}$ K $^{-1}$, °C]	($T_{\text{top}}, T_{\text{bottom}}$) [°C]
FE-G1R1L0	G1:0.2	R1:-0.01	L0:(0,0)	(29.75, 25.25)
FE-G1R1L1	G1:0.2	R1:-0.01	L1:(20,0)	(29.75, 25.25)
FE-G2R1L1	G2:1.5	R1:-0.01	L1:(20,0)	(58.25, 25.25)

as growth undercooling is fundamental to determine the onset of solidification.

The computation cases used in this study are presented in [table 3.1](#). The label of each case allows direct access to the simulation parameters as explained in the caption. Values for these parameters are inspired from the above experiments ([section 3.5.2](#)). Initial conditions consider a quiescent liquid at uniform composition given by the nominal alloy composition $\langle w_0 \rangle$. The temperature field is also initially uniform at a temperature averaged between the top and bottom initial values provided in [table 3.1](#). It has been checked that a uniform temperature gradient is swiftly reached, and that the unsteady regime to settle a vertical temperature gradient does not affect the phenomena studied. For simulations with grain structures, boundary conditions for nucleation at the bottom horizontal 22 mm \times 1 mm surface are kept constant as given in [table 3.1](#).

The macroscale approach employs the finite element method to compute the temperature and composition fields at FE nodes. The liquid fraction is then determined directly from the former fields, assuming a linear phase diagram, i.e. linear liquidus with full thermodynamic equilibrium between phases or lever rule approximation. This linear approximation is made available by the dotted line provided in [fig. 3.9](#). Note that this line defines a phase diagram that seems very different from the correct one. However, this linear fit is only used in a composition region located around the nominal composition of the alloy. It is also worth noticing that the eutectic microstructure is expected to appear at 15.3 °C. Nevertheless, experimental observations revealed that large eutectic nucleation undercooling was reached, so the eutectic solidification was not reported in the experiments studied by [Shevchenko et al. \[2013\]](#). Consequently, the solidification path is computed without accounting for the eutectic microstructure in the present simulations, thus extending the liquidus and solidus lines below the eutectic temperature as sketched with the linear approximations in [fig. 3.9](#).

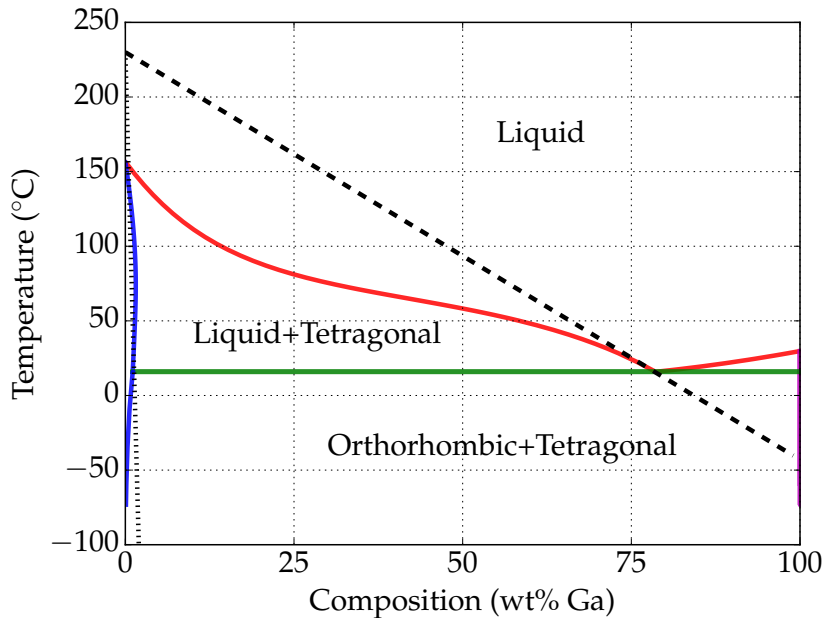


Fig. 3.9 – Binary phase diagram of the In-Ga system [Andersson et al. 2002; TCBIN 2006] and its approximation for solidification studies with an In-75 wt.% Ga alloy. The dashed and dotted lines are linear liquidus and solidus approximations near the nominal composition.

Results

The first case labeled FE-G1R1L0 is a reference case that features a low gradient (G1), low cooling rate (R1), and without any lateral cooling (L0), ensuring that isotherms retain a planar shape. These simulation parameters defined in [table 3.2](#), result in a negligible fluid flow reaching a maximum velocity of $4 \times 10^{-8} \text{ mm s}^{-1}$ in the bulk. Accordingly, the solidification front remains stable and follows the planar isotherms; no convective plumes are observed. The average composition field is thus only little modified in the mushy zone as shown in [fig. 3.10](#) (mind the values of the scale limits). It is concluded that velocity in the bulk is not high enough to initiate instabilities. In the next case, FE-G1R1L1, a cooling flux with a constant and very low value of the heat transfer coefficient is imposed on both vertical lateral surfaces to initiate a downward fluid flow due to thermal buoyancy. Once solidification starts, solute-rich regions start to appear on the sides of the domain. Despite the visible concentration difference between these lateral regions and the central mush seen in [fig. 3.10](#), their diffuse and uniform aspect indicates no resemblance to channel segregations. We keep the same configuration but increase the vertical gradient from 0.2 K mm^{-1} (G1) to 1.5 K mm^{-1} (G2) in the case FE-G2R1L1.

The isotherms become closer to each other hence reducing the depth of the mushy zone for the same time increment compared to the preceding case. The rejected gallium

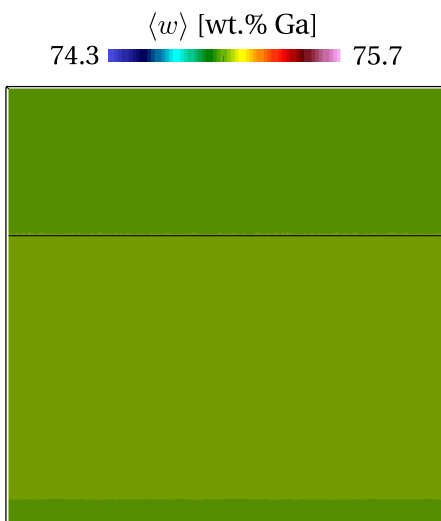
3.5. Macroscopic prediction of channel segregates

Table 3.2 – Material parameters for In-75 wt.% Ga and numerical parameters.

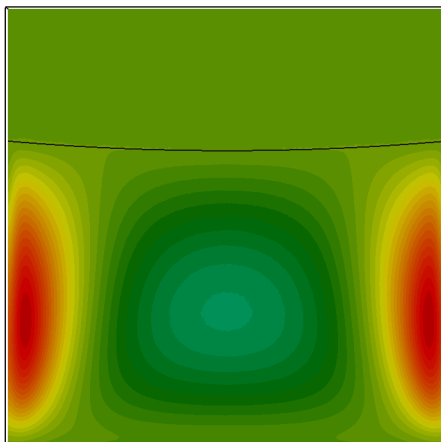
Parameter	Symbol	Value	Unit
Nominal composition	$\langle w_0 \rangle$	75	wt.%
Liquidus temperature	T_l	25.25	°C
Segregation coefficient	k	0.0165	wt.% wt.% ⁻¹
Liquidus slope	m_l	-2.73	K wt.% ⁻¹
Gibbs-Thomson coefficient	Γ_{GT}	2×10^{-7}	K m ⁻¹
Heat capacity (liquid and solid)	C_p	380.74	J kg ⁻¹ K ⁻¹
Enthalpy of fusion	L	8.02×10^{-4}	J kg ⁻¹
Diffusion coefficient of Ga in liquid In	D^l	1.525×10^{-9}	m ² s ⁻¹
Dynamic viscosity	μ^l	2×10^{-3}	Pas
Thermal expansion coefficient	β_T	0.0978×10^{-3}	K ⁻¹
Solutal expansion coefficient	$\beta_{\langle w \rangle^l}$	1.44×10^{-3}	wt.% ⁻¹
Thermal conductivity in the solid	$\langle \kappa \rangle^s$	40	W m ⁻¹ K ⁻¹
Thermal conductivity in the liquid	$\langle \kappa \rangle^l$	28	W m ⁻¹ K ⁻¹
Dendrite arm spacing	λ	60×10^{-6}	m
Density	ρ_0^l	6725	kg m ⁻³
Reference composition	w_0^l	75	wt.%
Reference temperature	T_0	25.25	°C
CA cell size		30×10^{-6}	m
FE mesh size		140×10^{-6}	m
Time step	Δt	0.1	s

solute locally accumulates at several different positions in the mushy zone, stemming from the base of the cell, with a maximum of 0.7 wt.%Ga above nominal composition. This is the consequence of segregation of gallium rich liquid being lighter than the above liquid bulk and creating an upward buoyancy force. A positive segregation and subsequent Ga-rich chimneys then rise up with an upward velocity component slightly greater than 1 mm s^{-1} .

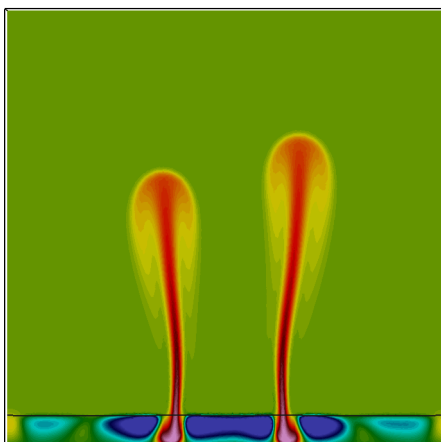
[Figure 3.11](#) gives a series of snapshots for case FE-G2R1L1 at three different times. Among the two clear distinct plumes that are visible at 250 s in [fig. 3.10](#), only one has led to the formation of a segregated channel that remains in [fig. 3.11](#) at 500 s. In fact, an animation between 250 s and 500 s (not shown here) reveals that one plume vanishes, thus permitting the first one to further develop. A second segregated channel is also seen on the left hand side of the cell. These two channels are stable for a long time since they remain at time 1000 s. However, the left side channel develops further to become the main one at 1500 s, while the mid-width channel decreases in intensity, changes orientation and subsequently disappears (not shown here). Thus, the birth



(a) FE-G1R1L0



(b) FE-G1R1L1



(c) FE-G2R1L1

Fig. 3.10 – Average Ga composition field at 250 s for the 3 FE cases showing the influence of process parameters on the freckling tendency. The black line represents the liquidus isotherm given in [table 3.2](#).

3.5. Macroscopic prediction of channel segregates

and death of very few channels is observed in this simulation, mainly due to solutal instability, as the temperature field shown in [fig. 3.11](#) clearly remains stable despite the low lateral heat flux. As shown in [fig. 3.10](#), instability is yet required to create these chemical plumes and channels. Here, it is created by a very small lateral heat flow but other sources of instability could be involved, as shown with the grain structure in the next section.

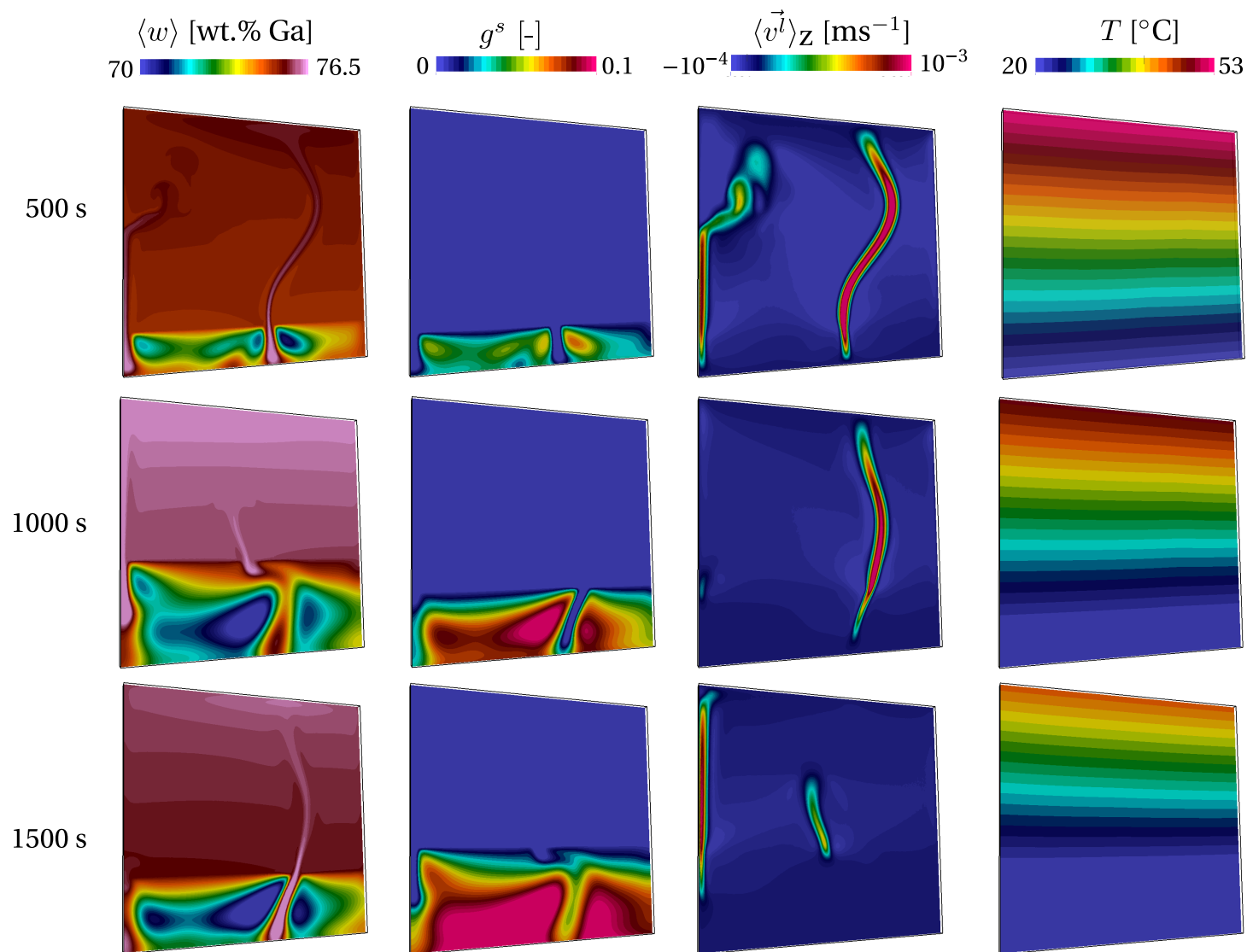


Fig. 3.11 – Simulation results for case FE-G2R1L1 showing maps of the average composition in gallium, the solid fraction, the vertical component (z-axis) of the superficial velocity field and the temperature, on a cut plane at the center of the cell at 500 s, 1000 s and 1500 s.

Discussion

In section 3.5.1, we have introduced some successful attempts of freckle predictions. The authors tackled the problem from an qualitative perspective. To our knowledge, the closest work to quantitative freckling analysis in solidification literature was done by Ramirez and Beckermann [2003]. They attempted to draw a correlation (freckling criterion) between the process parameters and the occurrence of freckles, without any size or shape constraints, i.e. any flow instability that may appear and form the smallest freckle is considered.

To accomplish this, they took a number of experiments done independently by Pollock and Murphy [1996] and Auburtin et al. [2000] where the casting parameters vary one at a time: casting speed (R), thermal gradient (\vec{G}), angle (θ) with respect to vertical orientation and nominal composition ($\langle w_0 \rangle$), giving a database for 6 different superalloys. The experimental results were compared to a modified Rayleigh number that accounts for the various parameters. It allowed them to define a threshold for freckle formation in Nickel-base superalloys, as well as Pb-Sn alloys.

Other contributions by Yuan and Lee [2012] (Pb-Sn alloy) and Karagadde et al. [2014] (In-Ga alloy) relied on a Cellular Automata Finite Difference (CAFD) model developed by Lee et al. [2002], which solves the dendrite tip growth kinetics at the solid-liquid interface together with macroscopic conservation equations. The authors compared the simulated formation of freckles with the results obtained by Shevchenko et al. [2013]. However, these simulations follow solidification in a small volume that contains a few dendrites with interdendritic liquid, therefore limited as far as to predict the liquid behaviour outside the mushy zone. On another hand, experimental observations reveal a great deal of information regarding solute redistribution, first in the chimneys that wash the dendrites in their way and then convective plumes that expel chemical species outside the mush, resulting in a global complex phenomenon.

In order to capture simultaneously the interaction between the mushy zone and the free liquid, we use the Cellular Automata Finite Element (CAFE) method to combine the macroscopic and mesoscopic length scales and predict more realistic channel segregation.

3.6 Meso-Macro prediction of channel segregates

3.6.1 Numerical method

Microscopic scale

The CAFE model introduces a grid of regular and structured cubic cells, with a constant size in all space directions, referred to as the cellular automaton (CA) grid. It is different from the unstructured finite element mesh previously mentioned for the solution of the average conservation equations. A typical CA step dimension is smaller than the smallest FE mesh size. The CA grid serves to represent solidification phenomena including nucleation, growth and remelting of the envelope of the primary dendritic grains. Details about the CAFE model can be found in [Carozzani et al. 2012; Carozzani et al. 2013; Carozzani et al. 2014]. Cell information, such as the temperature, the average composition or the velocity of the liquid phase, is interpolated from the nodes of the FE mesh. State indices are also defined for each CA cell, providing the presence of liquid or solid phases.

Nucleation

Initially, cells are in a fully liquid state. In the present situation, random nucleation sites are chosen based on a nucleation density, n_{\max} (expressed in surface density inverse m⁻²), at the bottom surface of the geometry in contact with the cooler. Nucleation occurs in a cell only if the latter contains a nucleation site, and when the local undercooling of the cell reaches the critical nucleation undercooling given as input by a Gaussian distribution of mean undercooling ΔT_N with a standard deviation ΔT_σ . The crystallographic orientation of each grain newly nucleated is also randomly chosen using values of the Euler angles to fully define the three rotations that transform the reference frame to the $\langle 100 \rangle$ directions that define the main growth axes of the dendrite trunks and arms. Grain selection is therefore solely controlled by growth competition.

Growth

Dendrite growth is driven by the chemical supersaturation $\Omega_{\text{saturation}}$, which is a dimensionless number proportional to the difference between the liquid composition at the dendrite tip and the melt composition far away from the tip. The higher the supersaturation, the faster the dendrite tip velocity. However, in the presence of a convective fluid, the chemical supersaturation is highly influenced by the intensity

and the direction of the flow with respect to the growth direction of the dendrites. In the current model, convection is central in studying the formation of channel segregation. Therefore, the purely diffusive Ivantsov relation used to determine the Peclet number Pe as function of the supersaturation, is replaced by a modified relation using a boundary layer correlation model that accounts for both the intensity and the mis-orientation of the liquid velocity with respect to the growth direction of the dendrites [Gandin et al. 2003]. The main parameters for this growth kinetics models are the Gibbs Thomson coefficient, Γ_{GT} , and the diffusion coefficient for Ga in In, D^l .

Solidification path

The CA model gives the presence of the grains in the liquid as well as its growth undercooling. For coupling with macroscopic scale modelling, the fraction of phases needs to be fed back to the FE model. This is now done by accounting for the information provided by the CA model. Thus, the fraction of solid is no longer the consequence of a simple conversion of the temperature and composition assuming thermodynamic equilibrium. It also includes the solidification delay due to the kinetics of the development of the grains as detailed elsewhere in the work of Carozzani et al. [2013].

Numerical method

Both the finite element mesh and the cellular automaton grid play a role in predicting channel segregation inasmuch as this type of defect originate from interplays between hydrodynamic instabilities on the scale of the dendrites and macroscopic flows defined by the geometry of the experimental cell [Shevchenko et al. 2013]. One has to respect a small maximum FE mesh size, comparable to the dendrite arm spacing. With such an element size, composition gradients giving rise to solutal buoyancy forces can be captured. This limits consequently the CA cell size, as a minimum number of cells is required in each finite element. In the array of simulations that will be presented in the next section, the value of λ_2 was considered. We have chosen a fixed mesh element size of $2\lambda_2$ and a CA cell size of $\lambda_2/2$. An average of 4 CA cells per unit length of a finite element is enough to accurately compute the development of the grain envelopes together with the solutal, thermal and mechanical interactions.

3.6.2 Configuration

Knowing that the configuration in FE-G2R1L1 produces segregated channels, the same set of parameters is first used for case CAFE-G2R1L1 by adding the effect of the grain structure using the CAFE model. Results are accessible in fig. 3.13 for comparison with

[fig. 3.11](#). A striking difference is seen: the composition maps become more perturbed as shown by the formation of numerous plumes when coupling with grain structure is active. The growing front displayed on the grain structure at the right most column of [fig. 3.13](#) dictates the leading position of the mushy zone shown in the third column. Note that each color corresponds to one grain, with 17 grains having nucleated at the cell's bottom surface. However, comparison of the solid fraction maps between [fig. 3.11](#) and [fig. 3.13](#) at the same times reveals a delay in the growing front position. Values of the nucleation parameters in [table 3.3](#) are such that few grains rapidly form below the nominal liquidus isotherm. The delay is therefore not due to the nucleation undercooling but to the growth undercooling of the dendrite tips. It should be noticed that, the growth front driven by undercooling in [fig. 3.13](#) also forms with a higher initial solid fraction and hence larger solute segregation occurs at the front. This effect, together with instabilities of the composition field, is caused by a more perturbed fluid flow and more plumes as observed in CAFE-G2R1L1 compared to FE-G2R1L1. Such observations fit to the complicated fluid and solute flow patterns typically occurring in the experiments as shown in [fig. 3.14](#). It becomes obvious that the consideration of grain structure and growth undercooling are vital to accurately simulate chimney formation in these experiments. The reasons for the instabilities are discussed hereinafter.

In the present 3D CAFE simulation, each grain shown in [fig. 3.12](#) is associated with a crystallographic orientation. The growth kinetics is only given for the $\langle 100 \rangle$ crystallographic directions at the grain boundaries with the liquid. The CA growth model is based on the hypothesis that, in a quiescent liquid of uniform temperature distribution and composition, the grain envelop should reproduce an octahedral grain shape with main directions given by the six $\langle 100 \rangle$ directions.

In the present situation where complicated fields are present for temperature, composition and liquid velocity, each grain envelope with different crystallographic orientation adapts differently to its local environment. Thus, the local undercooling of the front varies everywhere. Such variations are within few degrees here, but this is sufficient to create irregularities on the growth front, as seen on the grain structure in [fig. 3.12](#). Apart from that, these variations are linked to the position of the instabilities for the chemical and liquid velocity fields, thus demonstrating the full coupling between the CA and FE models.

3.6. Meso-Macro prediction of channel segregates

Table 3.3 – Summary of the simulations and the corresponding parameters for the CAFE cases, coupling macroscopic model with the grain structure model. Parameters are varied from (G1) low to (G2) high gradient, (R1) low to (R2) high cooling rate and (L0) no, (L1) low and (L2) high lateral cooling.

Case	Vertical gradient $\ \vec{G}\ $ [K mm $^{-1}$]	Cooling rate R [K s $^{-1}$]	Lateral cooling L (h $_{ext}$, T $_{ext}$) [W m $^{-2}$ K $^{-1}$, °C]	Initial temperature (T $_{top}$, T $_{bottom}$) [°C]	Nucleation (n $_{max}$, ΔT $_N$, ΔT $_\sigma$) [m $^{-2}$, °C, °C]
CAFE-G2R1L1	G2:1.5	R1:-0.01	L1:(20,0)	(58.25, 25.25)	(10 6 , 1, 0.2)
CAFE-G1R1L1	G1:0.2	R1:-0.01	L1:(20,0)	(29.75, 25.25)	(10 6 , 1, 0.2)
CAFE-G1R1L2	G1:0.2	R1:-0.01	L2:(500,0)	(29.75, 25.25)	(10 6 , 1, 0.2)
CAFE-G2R2L1	G1:0.2	R2:-0.05	L1:(20,0)	(29.75, 25.25)	(10 6 , 1, 0.2)

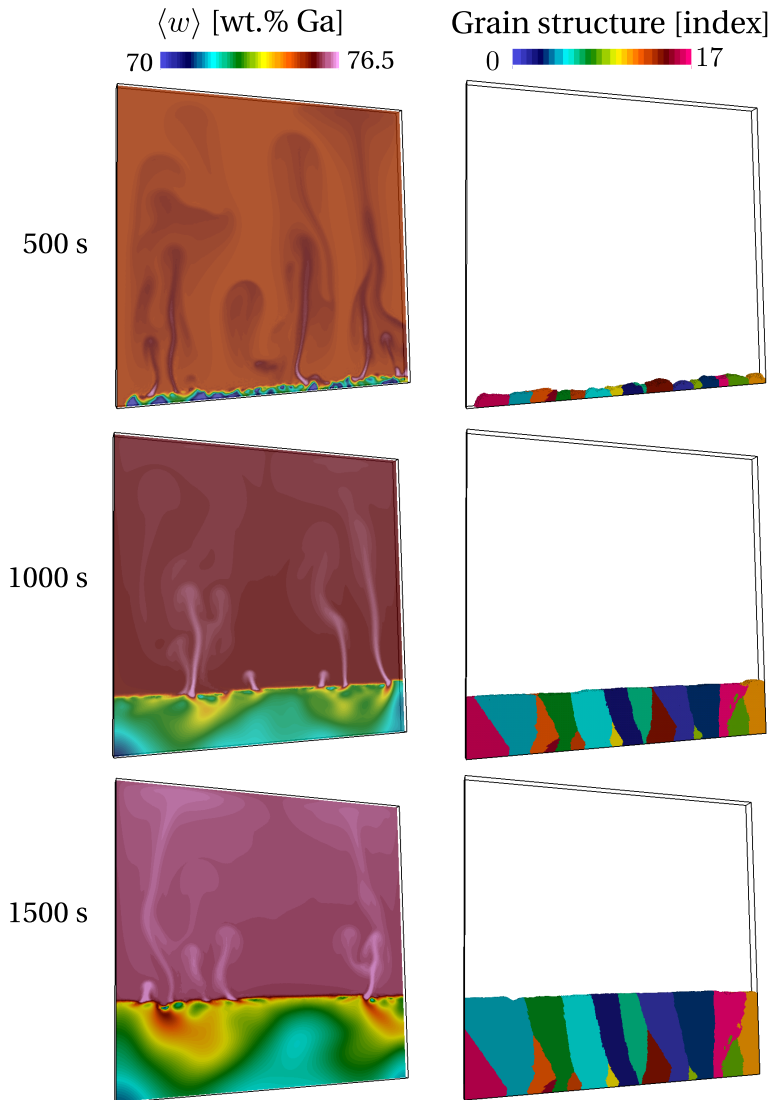


Fig. 3.12 – Simulation results the predicted of mushy grain structure with the corresponding composition maps, at 500 s, 1000 s and 1500 s.

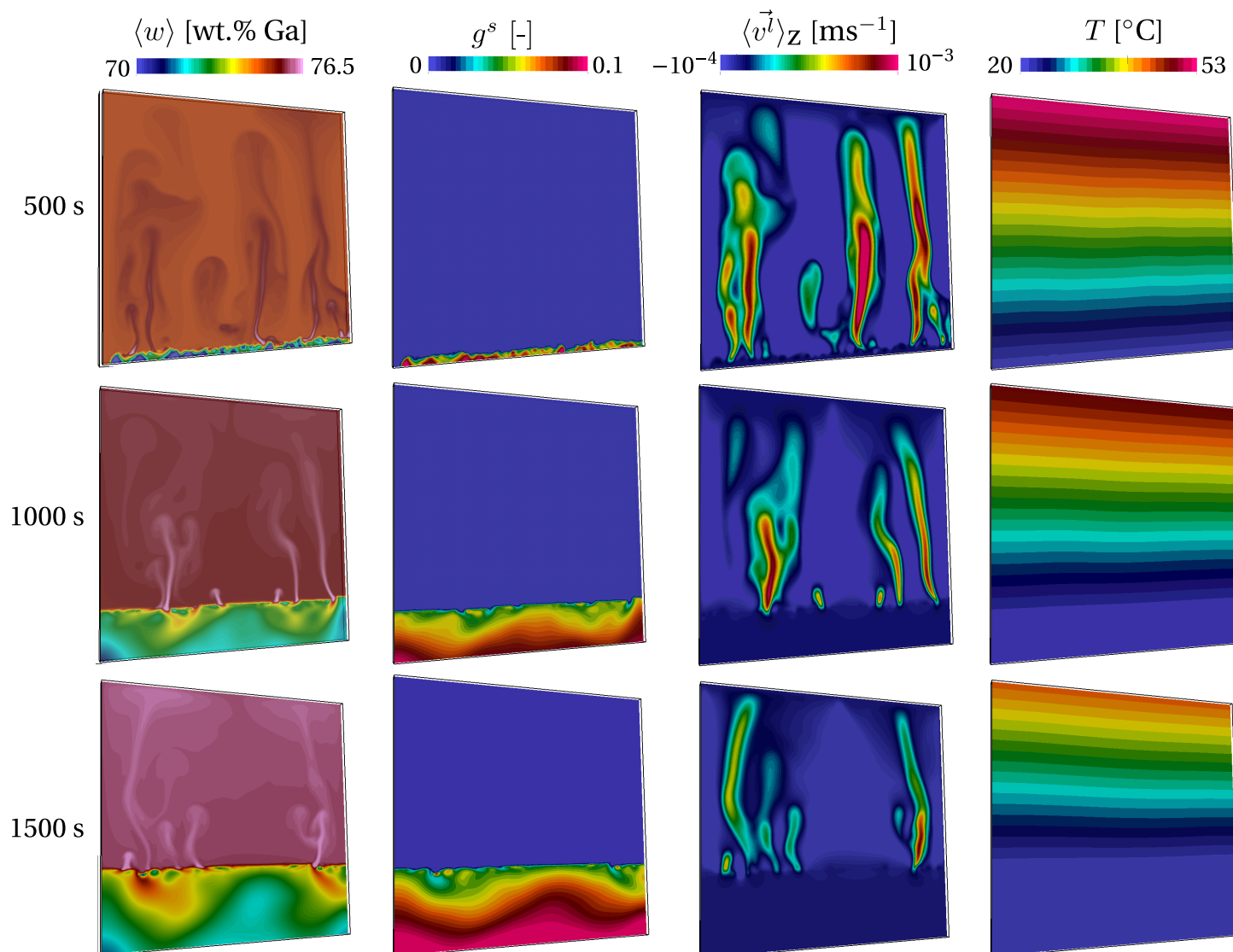


Fig. 3.13 – Simulation results for case CAFE-G2R1L1 showing maps of the average composition in gallium, the solid fraction, the vertical component (z-axis) of the superficial velocity field and the temperature, on a cut plane at the center of the cell at 500 s, 1000 s and 1500 s.

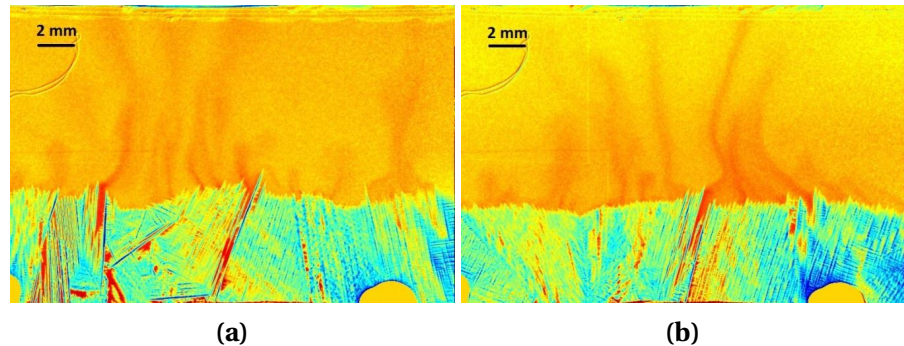


Fig. 3.14 – Snapshots of dendritic structure and composition field obtained from two solidification experiments at a cooling rate $R=-0.01 \text{ K s}^{-1}$ and temperature gradients of (a) $\|\vec{G}\|=1.1 \text{ K mm}^{-1}$ and (b) $\|\vec{G}\|=1.3 \text{ K mm}^{-1}$.

3.6.3 Effect of vertical temperature gradient

The influence of diverse process parameters can now be considered in context of the grain structure. The effect of the vertical temperature gradient is shown by comparing the previous case CAFE-G2R1L1 with case CAFE-G1R1L1. The temperature gradient is decreased about 7 times here, from $G_2=1.5 \text{ K mm}^{-1}$ to $G_1=0.2 \text{ K mm}^{-1}$. In fact, both cases share almost all traits with respect to flow patterns and velocity magnitude in the bulk. Main differences are yet seen regarding the dynamics of the plumes shown in fig. 3.15.

In the case of a low temperature gradient (G_1), the solidification front cannot maintain a shape as smooth as for the case of a large temperature gradient (G_2): the solute gradient in the liquid of the mushy zone (basically following the lever rule approximation for a given temperature) decreases, leading to a lower gradient of the solutal buoyancy force. In turn, more solute accumulates close to the front and locally reduces the growth velocity, thus creating larger “valleys” or steps with higher solute content. The irregular geometry of the front is also influenced by the dendrite tip growth kinetics model. The velocity of the isotherms is the ratio of the cooling rate, R , to the temperature gradient, \vec{G} . Consequently, the isotherm velocity in case G1 is larger than in G2, since cooling rate, R_1 , is the same in both cases. Moreover, because the dendrite tip velocity is a monotonously increasing function with the undercooling [Gandin et al. 2003], the latter for CAFE-G1R1L1 is larger than for CAFE-G2R1L1. Height differences of the growth front are proportional to the variations of the undercooling by the temperature gradient. Therefore, this forms larger steps on the growth front for case G1 compared to G2.

The chimney extends deeper in the mushy zone when the temperature gradient in-

Chapter 3. Macrosegregation with liquid metal motion

creases. This is confirmed by both the simulation results shown in [fig. 3.15](#) as well as the experimental observations. Another remarkable phenomenon is also observed in the low gradient case: a “pulsing” mechanism in CAFE-G1R1L1 where a series of solute rich liquid pockets are observed one above the other. This corresponds to a repeated and localized strong spatial variation of the liquid velocity field outside the mushy zone, regularly thrusting away small plumes. These pulses are roughly similar to each other in size and exit speed, creating thus a very regular pattern during some time.

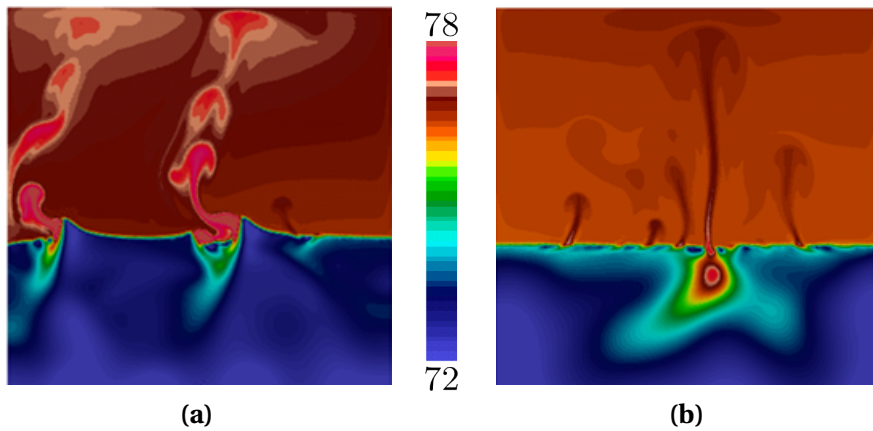


Fig. 3.15 – Average composition maps for CAFE-G1R1L1 at time 1060 s and CAFE-G2R1L1 at time 1845 s.



Fig. 3.16 – Snapshot of the pulsing mechanism coming from a groove shape in the mushy (check animation in the PDF file).

In the case of a high temperature gradient (case CAFE-G2R1L1) this phenomenon is barely seen. In fact, the pattern shown in [fig. 3.15](#) is more typical, with continuous plume rising from the mushy zone and reaching the top of the domain. However, such regular plume is the initial and final pattern seen for low gradient before the pulsing regime. Similar observations have been made in the experiments too. [Figure 3.17a](#)

displays the phenomenon of the “pulsing” plumes, which could be explained by the following mechanisms. The permeability of the mushy zone and the narrow gap of the solidification cell obstruct the feeding of the plumes by solute. A critical solute concentration has to be accumulated at a specific location in order to trigger the formation of a rising plume. An interim drop of the solute concentration below such a threshold would interrupt the plume. Flow instabilities can be another reason for the peculiar shape of the plumes. [Figure 3.17b](#) shows a pronounced continuous plume. The same plume can be seen a few seconds later in [fig. 3.17c](#). The plume structure becomes unstable; one can observe an indentation of streamlines followed by a mixing of rising solute-rich liquid with descending In-rich fluid. This mechanism also causes a non-continuous structure of the plumes.

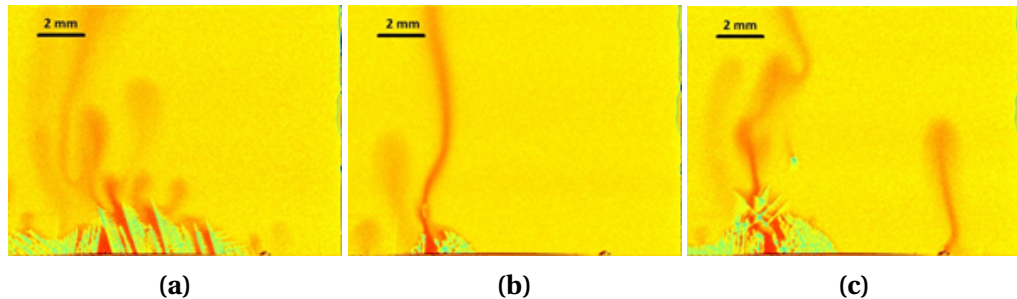


Fig. 3.17 – Snapshots of dendrite structure and composition field from two solidification experiments conducted at a cooling rate $R=-0.01 \text{ K s}^{-1}$ and a temperature gradient $\|\vec{G}\|=1 \text{ K mm}^{-1}$: (a) “pulsing” plumes, (b) continuous plume, (c) upcoming plume instability.

3.6.4 Effect of cooling rate

The next parameter studied is the cooling rate, corresponding to case CAFE-G1R2L1. A snapshot of the composition map and the corresponding vertical component of the velocity field are given in [fig. 3.18](#). We see a similarity with case CAFE-G1R1L1 in [fig. 3.15a](#) with respect to the buckled interface between the liquid and the mushy zone as well a plume pulsing effect when a low temperature gradient is applied. On the other hand, segregation inside the mush is more irregular with more pronounced patterns reaching a larger depth.

One could distinguish alternating V and A shapes patterns in the mushy zone. As for case CAFE-G1R1L1, these patterns are created by a network of pulsing plumes formed by the steps created on the delocalized growth front due to the low temperature gradient. However, these considerations are not sufficient to explain the shape of the growth front. The reason for the protuberances created at the tips of the V shape is the presence of a descending bulk liquid with a low composition seen by the growth

front. It infers that favorable growth conditions are created for a higher working temperature since the dendrite tip undercooling decreases for facing liquid flow and a lower composition; the growth rate is given by the isotherm velocity. The growth front thus adjusts its position to catch up with the corresponding isotherm, the latter being located at the tips of the V shape, i.e. the outmost advanced position of the growth front. It also means that the V shape angle depends on the size and intensity of the convection loops above the front. When the steps are formed on the growth front, the plumes exiting the mushy zone follow a direction normal to the front. They are inclined towards each other above the V shape. As a result, they may join and form a larger plume as seen in CAFE-G1R1L1 ([fig. 3.15a](#)), thus forming larger and more stable chimneys. The other observation in [fig. 3.18](#) is the existence of stable regions of the growth front. For instance, this is seen in between the two V shape forming or on the right hand side of the cell.

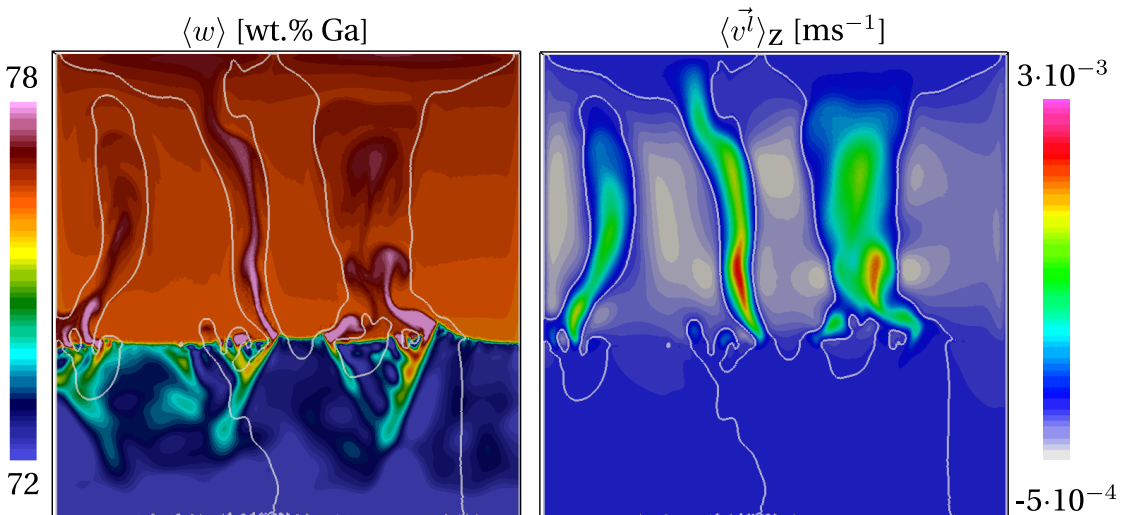


Fig. 3.18 – Average fields inside the cell for case CAFE-G1R2L1 at 350 s. The white contour identifies the zero velocity limit for the vertical component (z-axis) of the velocity field .

The reason for this stability is the inversion of the composition gradient located ahead. Animation shows that solute coming from the top of the cell is responsible for this accumulation, creating a layering that provides a stabilization effect above the mushy zone. This is verified by the vertical component of the average velocity also made available in [fig. 3.18](#). It is negative outside the path of the plumes. A resulting concurrent effect is the formation of the A shape segregates in between the V shape patterns seen in [fig. 3.18](#). Finally, it can be observed that these patterns are sustained longer compared to [fig. 3.15](#) CAFE-G1R1L1 because, at high cooling rate, the flow in the mushy zone is decreased due to a faster solidification. This is the same effect as described for

the large gradient configuration in CAFE-G2R1L1 ([fig. 3.15b](#)).

It is not clear how these observations could be compared with the A and V shapes segregates reported for steel ingots [Pickering 2013]. Despite the fact that macrosegregation is the main phenomenon leading to these patterns, there has not been a clear explanation yet in the literature for their formation. However, for steel casting, the A and V patterns are believed to form concomitantly. Further investigations would thus be required to quantify the consequences of thermosolutal instabilities simulated here for an In-75 wt.% Ga alloy and check their possible correlation with experimental observations in steel casting.

3.6.5 Effect of lateral temperature gradient

The previous simulations show the effect of cooling rate and temperature gradient on the survival of segregation patterns deep in the mushy zone. Another simulation is performed by increasing the cooling rate using higher heat flux extracted from the vertical side boundaries. This is achieved in case CAFE-G1R1L2 where the heat transfer coefficient reaches $500 \text{ W m}^{-2} \text{ K}^{-1}$. As a consequence of the large cooling from the sides, the temperature gradient is no longer vertical. A distinct flow due to thermal buoyancy is created, driving a cold liquid downwards near the sides of the cell. Under the influence of these two main convection loops, all segregation plumes tend to regroup in the middle of the domain, forming a larger central plume, as seen in the composition map at 450 s in [fig. 3.19](#). However, this regime occurs at times earlier than 500 s, where the effect of thermally induced buoyancy forces is prevailing, feeding the convection loops. Approximately 500 s later, the mushy zone has extended, favouring the segregation mechanical forces i.e. $\rho_{\text{ref}} \left(1 - \beta_{\langle w \rangle^l} \Delta \langle w \rangle^l\right) \vec{g}$, rather than the thermal mechanical forces, $\rho_{\text{ref}} (1 - \beta_T \Delta T) \vec{g}$.

[Figure 3.19](#) shows the corresponding composition maps with stable segregated channels at about 1000 s that also remain at 1500 s. The solidification front then tends to form a concave shape at the center of the cell, thus partially revealing the form of the isotherms toward the cell center. The stable pattern in the center is similar to the plateau seen at the center, between the A-shapes in [fig. 3.15](#) and [fig. 3.18](#). As stated before, it is an inactive region with respect to plume initiation due to the inversion of the solute composition gradient. In other words, the high gallium concentration at the top of cell causes indium, which is the heavier species, to accumulate and be partially trapped between the mushy walls, thus creating a stable flow configuration.

Outside of the plateau, two plumes are observed from the prominent instabilities of the growth front, adopting diverging directions. This is also observed at the center of the cell in [fig. 3.18](#) on each side of the A-shape segregate. These plumes in [fig. 3.19](#)

lead to the formation of two stable channels. The corresponding situation in the experiment is shown in [fig. 3.20](#). The chimneys on both sides and the plateau in between can be clearly recognised.

The additional cooling at the side walls produces two flow vortices between the side wall and the strong convective plumes above the chimneys. The central part of the sample remains almost unaffected by the additionally driven thermal convection. This area is characterised by the occurrence of a number of smaller convective plumes.

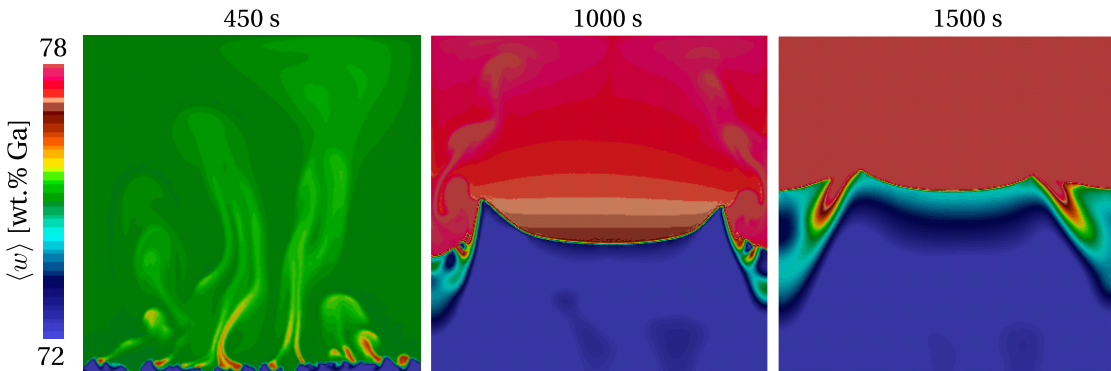


Fig. 3.19 – 2D cut plane of the average composition inside the cell for case CAFE-G1R1L2 at the following time increments: 450 s, 1000 s and 1500 s.

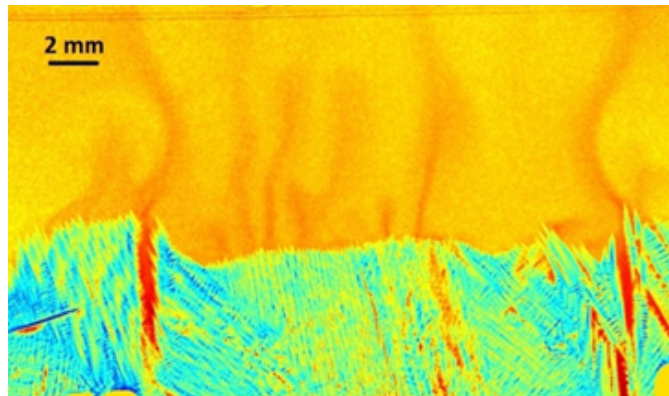


Fig. 3.20 – Snapshot of dendritic structure and composition field from a solidification experiment recorded at 1000 s for a cooling rate $R = -0.01 \text{ K s}^{-1}$ and a temperature gradient $\|\vec{G}\| = -1 \text{ K mm}^{-1}$.

3.6.6 Mono-grain freckles

All CAFE simulations were performed considering a normal classic heterogeneous nucleation at the surface of the mould where the metal is cooled down. However, as the number of grains is not negligible, the subsequent fluid-structure interaction between

dendrites, simply represented by an isotropic permeability and the interdendritic flow cannot be easily interpreted. Therefore, one may consider simpler solidification cases like a mono-grain growth. This ideal situation is not always experimentally viable: either the mould surface is not perfectly smooth, and therefore nucleation can be triggered by a wetting mechanism, or the metal contains a certain level of impurity which can trigger nucleation heterogeneously in the liquid bulk. Regardless of this experimental limitation, this type of simulations allows simpler understanding as the grain growth is not disturbed by another neighbouring grain, it grows while exclusively interacting with the liquid phase.

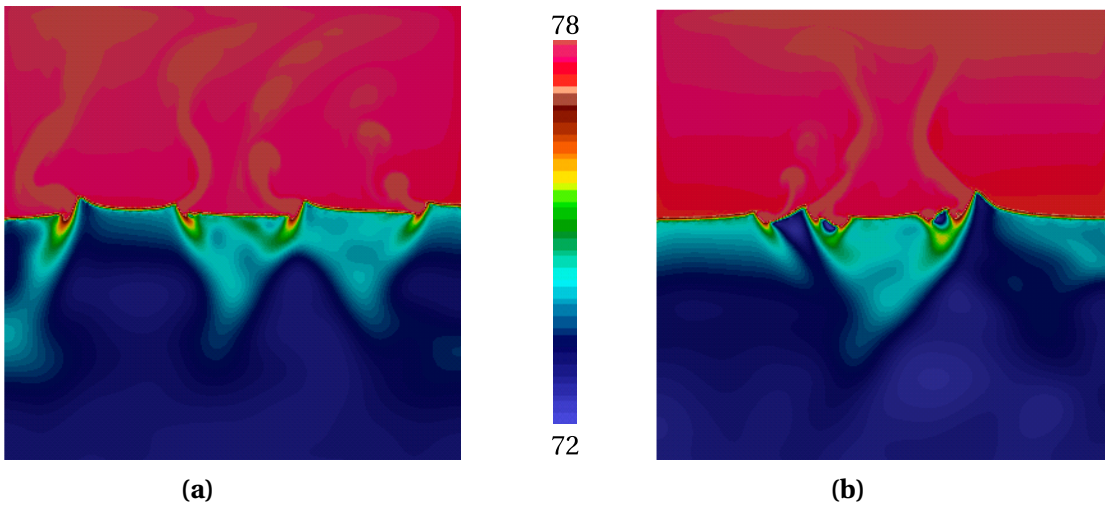


Fig. 3.21 – Snapshots of mono-grain solidification showing the average composition in gallium predicted by the CAFE approach. Two orientation scenarios are considered where a) the grain is upright with a Euler angle of $(90^\circ, 0^\circ, 0^\circ)$ or b) the grain is tilted with a Euler angle of $(90^\circ, 30^\circ, 0^\circ)$ (check animation in the PDF file).

Résumé chapitre 4

Ce 4^e chapitre est dédié à la macroségrégation induite par le mouvement de la phase liquide par convection thermosolutale, à solide fixe et en absence de retrait à la solidification ($\langle \rho \rangle^s = \langle \rho \rangle^l$). Pour cela, nous introduisons dans un premier temps les principaux schémas de résolution des équations Navier-Stokes selon la façon dont ils répondent aux critères de stabilité de Babuška-Brezzi: les éléments finis mixtes et la méthode multi-échelles variationnelle (Variational MultiScale).

En choisissant la seconde méthode, nous donnons les détails de la formulation éléments finis correspondante qui régit les écoulements dans la phase liquide loin du front de solidification, ainsi qu'au sein de la zone dendritique pâteuse. Le principal moteur de mouvement liquide est la convection thermosolutale. Celle-ci est générée par la densité du liquide qui varie à la fois avec la température et la composition intrinsèque de la phase liquide, contribuant ainsi à la redistribution des éléments d'alliage. On s'intéresse à ce type de méso-macroségrégation en montrant une application de solidification dirigée, traitée dans le chapitre 3 en diffusion pure. Nous montrons qu'en fin de solidification, les écoulements créent des canaux à forte ségrégation positive en peau et dans le cœur de la pièce.

L'investigation de ce défaut fait ensuite l'objet d'une confrontation qualitative entre la simulation et une expérience de solidification. Cette dernière consiste en un banc de solidification dirigée d'un alliage d'indium-gallium à bas point de fusion. Un suivi en caméra rapide permet de suivre la formation de la microstructure en fonction du temps. Par le biais de la simulation, on teste d'abord la performance du modèle purement macroscopique, i.e. avec suivi indirect des structures et phases via leur fraction volumique. Les résultats montrent que les canaux de ségrégation sont visibles mais sont moins nombreux et moins stables que l'on prédit expérimentalement.

Ensuite, on rajoute au modèle précédent une couche de modélisation à l'échelle méssoscopique pour suivre directement les enveloppes des grains. Cette fois, la comparaison avec l'expérience montre que nous prédisons mieux qualitativement l'interaction complexe entre structure de solidification, l'écoulement au sein de la zone pâteuse et la ségrégation conséquente. Une étude paramétrique permet après d'étudier la sensibilité de l'occurrence et la forme des canaux ségrégés par rapport aux différents paramètres de contrôle du procédé.

Bibliography

[Andersson et al. 2002]

Andersson, J.-O., Helander, T., Höglund, L., Shi, P., and Sundman, B. (2002). “Thermo-Calc & DICTRA, computational tools for materials science”. *Calphad*, 26 (2), pp. 273–312. URL: <http://www.sciencedirect.com/science/article/pii/S0364591602000378> (cited on pages 35, 37, 38, 68).

[Arnold et al. 1984]

Arnold, D. N., Brezzi, F., and Fortin, M. (1984). “A stable finite element for the stokes equations”. *CALCOLO*, 21 (4), pp. 337–344. URL: <http://link.springer.com/article/10.1007/BF02576171> (cited on page 47).

[Auburtin et al. 2000]

Auburtin, P., Wang, T., Cockcroft, S. L., and Mitchell, A. (2000). “Freckle formation and freckle criterion in superalloy castings”. *Metallurgical and Materials Transactions B*, 31 (4), pp. 801–811. URL: <http://link.springer.com/article/10.1007/s11663-000-0117-9> (cited on page 73).

[Auburtin 1998]

Auburtin, P. B. L. (1998). “Determination of the influence of growth front angle on freckle formation in superalloys”. PhD thesis. Vancouver, BC, Canada: University of British Columbia. URL: https://circle.ubc.ca/bitstream/handle/2429/8676/ubc_1998-345084.pdf?sequence=1 (cited on page 63).

[Babuška 1971]

Babuška, I. (1971). “Error-bounds for finite element method”. *Numerische Mathematik*, 16 (4), pp. 322–333. URL: <http://link.springer.com/article/10.1007/BF02165003> (cited on page 47).

[Barbosa and Hughes 1991]

Barbosa, H. J. C. and Hughes, T. J. R. (1991). “The finite element method with Lagrange multipliers on the boundary: circumventing the Babuška-Brezzi condition”. *Computer Methods in Applied Mechanics and Engineering*, 85 (1), pp. 109–128. URL: <http://www.sciencedirect.com/science/article/pii/004578259190125P> (cited on page 47).

[Beckermann 2002]

Beckermann, C. (2002). “Modelling of macrosegregation: applications and future needs”. *International Materials Reviews*, 47 (5), pp. 243–261. URL: <http://www.maneyonline.com/doi/abs/10.1179/095066002225006557> (cited on page 9).

[Beckermann et al. 2000]

Beckermann, C., Gu, J. P., and Boettinger, W. J. (2000). “Development of a freckle predictor via

Bibliography

rayleigh number method for single-crystal nickel-base superalloy castings". *Metallurgical and Materials Transactions A*, 31 (10), pp. 2545–2557. URL: <http://link.springer.com/article/10.1007/s11661-000-0199-7> (cited on pages 56, 63).

[Bellet et al. 2009]

Bellet, M., Combeau, H., Fautrelle, Y., Gobin, D., Rady, M., Arquis, E., Budenkova, O., Dussoubs, B., Duterrail, Y., Kumar, A., Gandin, C. A., Goyeau, B., Mosbah, S., and Založník, M. (2009). "Call for contributions to a numerical benchmark problem for 2D columnar solidification of binary alloys". *International Journal of Thermal Sciences*, 48 (11), pp. 2013–2016. URL: <http://www.sciencedirect.com/science/article/pii/S129007290900177X> (cited on page 20).

[Boden et al. 2008]

Boden, S., Eckert, S., Willers, B., and Gerbeth, G. (2008). "X-Ray Radioscopic Visualization of the Solutal Convection during Solidification of a Ga-30 Wt Pct In Alloy". *Metallurgical and Materials Transactions A*, 39 (3), pp. 613–623. URL: <http://link.springer.com/article/10.1007/s11661-007-9462-5> (cited on page 64).

[Bogno et al. 2013]

Bogno, A., Nguyen-Thi, H., Reinhart, G., Billia, B., and Baruchel, J. (2013). "Growth and interaction of dendritic equiaxed grains: In situ characterization by synchrotron X-ray radiography". *Acta Materialia*, 61 (4), pp. 1303–1315. URL: <http://www.sciencedirect.com/science/article/pii/S1359645412008026> (cited on page 6).

[Brezzi 1974]

Brezzi, F. (1974). "On the existence, uniqueness and approximation of saddle-point problems arising from lagrangian multipliers". *ESAIM: Mathematical Modelling and Numerical Analysis - Modélisation Mathématique et Analyse Numérique*, 8 (R2), pp. 129–151. URL: <https://eudml.org/doc/193255> (cited on page 47).

[Buffet et al. 2010]

Buffet, A., Nguyen-Thi, H., Bogno, A., Schenk, T., Mangelinck-Noël, N., Reinhart, G., Bergeon, N., Billia, B., and Baruchel, J. (2010). "Measurement of Solute Profiles by Means of Synchrotron X-Ray Radiography during Directional Solidification of Al-4 wt% Cu Alloys". *Materials Science Forum*, 649, pp. 331–336. URL: <http://www.scientific.net/MSF.649.331> (cited on pages 5, 6).

[Carlson et al. 2002]

Carlson, K. D., Lin, Z., Hardin, R. A., and Beckermann, C. (2002). "Modeling Of Porosity Formation And Feeding Flow In Steel Casting". *Proceedings of the 56th SFSA Technical and Operating Conference*. Steel Founders' Society of America. URL: <http://goo.gl/p9ftCp> (cited on page 10).

[Carozzani et al. 2012]

Carozzani, T., Digonnet, H., and Gandin, C.-A. (2012). "3D CAFE modeling of grain structures: application to primary dendritic and secondary eutectic solidification". *Modelling and Simulation in Materials Science and Engineering*, 20 (1), p. 015010. URL: <http://iopscience.iop.org/0965-0393/20/1/015010> (cited on page 74).

[Carozzani et al. 2014]

Carozzani, T., Gandin, C.-A., and Digonnet, H. (2014). "Optimized parallel computing for cellular automaton-finite element modeling of solidification grain structures". *Modelling and Simulation*

Bibliography

- in Materials Science and Engineering*, 22 (1), p. 015012. URL: <http://iopscience.iop.org/0965-0393/22/1/015012> (cited on page 74).
- [Carozzani 2012]**
Carozzani, T. (2012). “Développement d'un modèle 3D Automate Cellulaire-Éléments Finis (CAFE) parallèle pour la prédiction de structures de grains lors de la solidification d'alliages métalliques”. PhD Thesis. Ecole Nationale Supérieure des Mines de Paris. URL: <http://pastel.archives-ouvertes.fr/pastel-00803282> (cited on page 14).
- [Carozzani et al. 2013]**
Carozzani, T., Gandin, C.-A., Digonnet, H., Bellet, M., Zaidat, K., and Fautrelle, Y. (2013). “Direct Simulation of a Solidification Benchmark Experiment”. *Metallurgical and Materials Transactions A*, 44 (2), pp. 873–887. URL: <http://link.springer.com/article/10.1007/s11661-012-1465-1> (cited on pages 20, 55, 74, 75).
- [Choudhary and Ganguly 2007]**
Choudhary, S. K. and Ganguly, S. (2007). “Morphology and Segregation in Continuously Cast High Carbon Steel Billets”. *ISIJ International*, 47 (12), pp. 1759–1766 (cited on page 3).
- [Combeau et al. 2009]**
Combeau, H., Založník, M., Hans, S., and Richy, P. E. (2009). “Prediction of Macrosegregation in Steel Ingots: Influence of the Motion and the Morphology of Equiaxed Grains”. *Metallurgical and Materials Transactions B*, 40 (3), pp. 289–304. URL: <http://link.springer.com/article/10.1007/s11663-008-9178-y> (cited on page 2).
- [Copley et al. 1970]**
Copley, S. M., Giamei, A. F., Johnson, S. M., and Hornbecker, M. F. (1970). “The origin of freckles in unidirectionally solidified castings”. *Metallurgical Transactions*, 1 (8), pp. 2193–2204. URL: <http://link.springer.com/article/10.1007/BF02643435> (cited on page 60).
- [Dantzig and Rappaz 2009]**
Dantzig, J. A. and Rappaz, M. (2009). *Solidification*. EPFL Press (cited on pages 6, 10).
- [Darcy 1856]**
Darcy, H. (1856). *Les fontaines publiques de la ville de Dijon : exposition et application des principes à suivre et des formules à employer dans les questions de distribution d'eau*. V. Dalmont (Paris). URL: <http://gallica.bnf.fr/ark:/12148/bpt6k624312> (cited on page 7).
- [Desbiolles et al. 2003]**
Desbiolles, J.-L., Thévoz, P., Rappaz, M., and Stefanescu, D. (2003). “Micro-Macrosegregation Modeling in Casting: A Fully Coupled 3D Model”. TMS Publ., pp. 245–252 (cited on page 63).
- [Digonnet et al. 2007]**
Digonnet, H., Silva, L., and Coupez, T. (2007). “Cimlib: A Fully Parallel Application For Numerical Simulations Based On Components Assembly”. *AIP Conference Proceedings*. Vol. 908. AIP Publishing, pp. 269–274. URL: <http://scitation.aip.org/content/aip/proceeding/aipcp/10.1063/1.2740823> (cited on page 14).
- [DLR 2014]**
DLR (2014). *ElectroMagnetic Levitation*. <http://goo.gl/e5JhiA> (cited on page 14).

Bibliography

[Doré et al. 2000]

Doré, X., Combeau, H., and Rappaz, M. (2000). "Modelling of microsegregation in ternary alloys: Application to the solidification of Al–Mg–Si". *Acta Materialia*, 48 (15), pp. 3951–3962. URL: <http://www.sciencedirect.com/science/article/pii/S1359645400001774> (cited on page 20).

[Du et al. 2007]

Du, Q., Eskin, D. G., and Katgerman, L. (2007). "Modeling Macrosegregation during Direct-Chill Casting of Multicomponent Aluminum Alloys". *Metallurgical and Materials Transactions A*, 38 (1), pp. 180–189. URL: <http://link.springer.com/article/10.1007/s11661-006-9042-0> (cited on page 20).

[Easton et al. 2011]

Easton, M., Davidson, C., and StJohn, D. (2011). "Grain Morphology of As-Cast Wrought Aluminium Alloys". *Materials Transactions*, 52 (5), pp. 842–847 (cited on page 6).

[Felicelli et al. 1991]

Felicelli, S. D., Heinrich, J. C., and Poirier, D. R. (1991). "Simulation of freckles during vertical solidification of binary alloys". *Metallurgical Transactions B*, 22 (6), pp. 847–859. URL: <http://link.springer.com/article/10.1007/BF02651162> (cited on pages 7, 58, 63).

[Felicelli et al. 1998]

Felicelli, S. D., Poirier, D. R., and Heinrich, J. C. (1998). "Modeling freckle formation in three dimensions during solidification of multicomponent alloys". *Metallurgical and Materials Transactions B*, 29 (4), pp. 847–855. URL: <http://link.springer.com/article/10.1007/s11663-998-0144-5> (cited on page 63).

[Ferreira et al. 2004]

Ferreira, I. L., Garcia, A., and Nestler, B. (2004). "On macrosegregation in ternary Al–Cu–Si alloys: numerical and experimental analysis". *Scripta Materialia*, 50 (4), pp. 407–411. URL: <http://www.sciencedirect.com/science/article/pii/S1359646203007346> (cited on page 8).

[Ferreira et al. 2009]

Ferreira, I., Moutinho, D., Gomes, L., Rocha, O., and Garcia, A. (2009). "Modeling and experimental analysis of macrosegregation during transient solidification of a ternary Al–6wt%Cu–1wt%Si alloy". *Philosophical Magazine Letters*, 89 (12), pp. 769–777. URL: <http://dx.doi.org/10.1080/09500830903292320> (cited on page 8).

[Flemings and Nereo 1967]

Flemings, M. C. and Nereo, G. E. (1967). "Macrosegregation: Part I". *Transactions of the Metallurgical Society of AIME*, 239, pp. 1449–1461 (cited on pages 7, 63).

[Flemings and Nereo 1968]

Flemings, M. C. and Nereo, G. E. (1968). "Macrosegregation: Part III". *Transactions of the Metallurgical Society of AIME*, 242, pp. 50–55 (cited on pages 7, 63).

[Flemings et al. 1968]

Flemings, M. C., Mehrabian, R., and Nereo, G. E. (1968). "Macrosegregation: Part II". *Transactions of the Metallurgical Society of AIME*, 242, pp. 41–49 (cited on pages 7, 63).

[Gandin 2000]

Gandin, C. A. (2000). "From constrained to unconstrained growth during directional solidifica-

- tion". *Acta Materialia*, 48 (10), pp. 2483–2501. URL: <http://www.sciencedirect.com/science/article/pii/S1359645400000707> (cited on pages 30, 43).
- [Gandin et al. 2003]**
Gandin, C. A., Guillemot, G., Appolaire, B., and Niane, N. T. (2003). "Boundary layer correlation for dendrite tip growth with fluid flow". *Materials Science and Engineering: A*, 342 (1–2), pp. 44–50. URL: <http://www.sciencedirect.com/science/article/pii/S0921509302002617> (cited on pages 75, 79).
- [Genereux and Borg 2000]**
Genereux, P. D. and Borg, C. A. (2000). "Characterization of Freckles in a High Strength Wrought Nickel Superalloy". Warrendale, PA: K.A. Green, M. McLean, S. Olson, J.J. Schirra, TMS (The Minerals, Metals, and Materials Society), pp. 19–27. URL: http://www.tms.org/superalloys/10.7449/2000/Superalloys_2000_19_27.pdf (cited on page 63).
- [Giamei and Kear 1970]**
Giamei, A. F. and Kear, B. H. (1970). "On the nature of freckles in nickel base superalloys". *Metalurgical Transactions*, 1 (8), pp. 2185–2192. URL: <http://link.springer.com/article/10.1007/BF02643434> (cited on pages 10, 63).
- [Gouttebroze 2005]**
Gouttebroze, S. (2005). "Modélisation 3d par éléments finis de la macroségrégation lors de la solidification d'alliages binaires". PhD thesis. École Nationale Supérieure des Mines de Paris. URL: <https://pastel.archives-ouvertes.fr/pastel-00001885/document> (cited on pages 14, 53).
- [Guo and Beckermann 2003]**
Guo, J. and Beckermann, C. (2003). "Three-Dimensional Simulation of Freckle Formation During Binary Alloy Solidification: Effect of Mesh Spacing". *Numerical Heat Transfer, Part A: Applications*, 44 (6). <http://dx.doi.org/10.1080/716100512>, pp. 559–576. URL: <http://user.engineering.uiowa.edu/~becker/documents.dir/GuoFreckle.pdf> (cited on page 63).
- [Hachani et al. 2012]**
Hachani, L., Saadi, B., Wang, X. D., Nouri, A., Zaidat, K., Belgacem-Bouzida, A., Ayouni-Derouiche, L., Raimondi, G., and Fautrelle, Y. (2012). "Experimental analysis of the solidification of Sn–3 wt.%Pb alloy under natural convection". *International Journal of Heat and Mass Transfer*, 55 (7–8), pp. 1986–1996. URL: <http://www.sciencedirect.com/science/article/pii/S0017931011007009> (cited on pages 8, 55).
- [Hachem et al. 2010]**
Hachem, E., Rivaux, B., Kloczko, T., Digonnet, H., and Coupez, T. (2010). "Stabilized finite element method for incompressible flows with high Reynolds number". *Journal of Computational Physics*, 229 (23), pp. 8643–8665. URL: <http://www.sciencedirect.com/science/article/pii/S0021999110004237> (cited on page 49).
- [Hachem 2009]**
Hachem, E. (2009). "Stabilized finite element method for heat transfer and turbulent flows inside industrial furnaces". PhD Thesis. École Nationale Supérieure des Mines de Paris. URL: <https://tel.archives-ouvertes.fr/tel-00443532> (cited on page 49).
- [Hebditch and Hunt 1974]**
Hebditch, D. J. and Hunt, J. D. (1974). "Observations of ingot macrosegregation on model systems".

Bibliography

Metallurgical Transactions, 5 (7), pp. 1557–1564. URL: <http://link.springer.com/article/10.1007/BF02646326> (cited on pages 8, 55).

[Karagadde et al. 2014]

Karagadde, S., Yuan, L., Shevchenko, N., Eckert, S., and Lee, P. D. (2014). “3-D microstructural model of freckle formation validated using in situ experiments”. *Acta Materialia*, 79, pp. 168–180. URL: <http://www.sciencedirect.com/science/article/pii/S1359645414004984> (cited on page 73).

[Kohler 2008]

Kohler, F. (2008). “Peritectic solidification of Cu-Sn alloys: microstructure competition at low speed”. PhD Thesis. EPFL (cited on page 63).

[Koshikawa et al. 2014]

Koshikawa, T., Gandin, C.-A., Bellet, M., Yamamura, H., and Bobadilla, M. (2014). “Computation of Phase Transformation Paths in Steels by a Combination of the Partial- and Para-equilibrium Thermodynamic Approximations”. *ISIJ International*, 54 (6), pp. 1274–1282 (cited on page 42).

[Lee et al. 2002]

Lee, P. D., Atwood, R. C., Dashwood, R. J., and Nagaumi, H. (2002). “Modeling of porosity formation in direct chill cast aluminum–magnesium alloys”. *Materials Science and Engineering: A*, 328 (1–2), pp. 213–222. URL: <http://www.sciencedirect.com/science/article/pii/S0921509301016872> (cited on page 73).

[Lesoult 2005]

Lesoult, G. (2005). “Macrosegregation in steel strands and ingots: Characterisation, formation and consequences”. *Materials Science and Engineering: A*, International Conference on Advances in Solidification Processes 413–414, pp. 19–29. URL: <http://www.sciencedirect.com/science/article/pii/S0921509305010063> (cited on pages 3, 8).

[Lesoult et al. 2001]

Lesoult, G., Albert, V., Appolaire, B., Combeau, H., Daloz, D., Joly, A., Stomp, C., Grün, G. U., and Jarry, P. (2001). “Equi-axed growth and related segregations in cast metallic alloys”. *Science and Technology of Advanced Materials*, 2 (1), p. 285. URL: <http://iopscience.iop.org/1468-6996/2/1/A55> (cited on page 8).

[Liu 2005]

Liu, W. (2005). “Finite Element Modelling of Macrosegregation and Thermomechanical Phenomena in Solidification Processes”. PhD thesis. École Nationale Supérieure des Mines de Paris. URL: <http://pastel.archives-ouvertes.fr/pastel-00001339> (cited on pages 14, 53).

[Ludwig et al. 2012]

Ludwig, A., Mogeritsch, J., Kolbe, M., Zimmermann, G., Sturz, L., Bergeon, N., Billia, B., Faivre, G., Akamatsu, S., Bottin-Rousseau, S., and Voss, D. (2012). “Advanced Solidification Studies on Transparent Alloy Systems: A New European Solidification Insert for Material Science Glovebox on Board the International Space Station”. *JOM*, 64 (9), pp. 1097–1101. URL: <http://link.springer.com/article/10.1007/s11837-012-0403-4> (cited on page 8).

[Mesri et al. 2009]

Mesri, Y., Digonnet, H., and Coupez, T. (2009). “Advanced parallel computing in material forming with CIMLib”. *European Journal of Computational Mechanics/Revue Européenne de Mécanique*

- Numérique*, 18 (7-8), pp. 669–694. URL: <http://www.tandfonline.com/doi/abs/10.3166/ejcm.18.669-694> (cited on page 14).
- [Mosbah 2008]**
Mosbah, S. (2008). “Multiple scales modeling of solidification grain structures and segregation in metallic alloys”. PhD thesis. École Nationale Supérieure des Mines de Paris. URL: <https://tel.archives-ouvertes.fr/tel-00349885/document> (cited on page 14).
- [Pickering 2013]**
Pickering, E. J. (2013). “Macrosegregation in Steel Ingots: The Applicability of Modelling and Characterisation Techniques”. *ISIJ International*, 53 (6), pp. 935–949 (cited on pages 63, 83).
- [Poirier 1987]**
Poirier, D. R. (1987). “Permeability for flow of interdendritic liquid in columnar-dendritic alloys”. *Metallurgical Transactions B*, 18 (1), pp. 245–255. URL: <http://link.springer.com/article/10.1007/BF02658450> (cited on page 7).
- [Pollock and Murphy 1996]**
Pollock, T. M. and Murphy, W. H. (1996). “The breakdown of single-crystal solidification in high refractory nickel-base alloys”. *Metallurgical and Materials Transactions A*, 27 (4), pp. 1081–1094. URL: <http://link.springer.com/article/10.1007/BF02649777> (cited on page 73).
- [Prescott et al. 1994]**
Prescott, P. J., Incropera, F. P., and Gaskell, D. R. (1994). “Convective Transport Phenomena and Macrosegregation During Solidification of a Binary Metal Alloy: II—Experiments and Comparisons With Numerical Predictions”. *Journal of Heat Transfer*, 116 (3), pp. 742–749. URL: <http://dx.doi.org/10.1115/1.2910930> (cited on page 8).
- [Ramirez and Beckermann 2003]**
Ramirez, J. C. and Beckermann, C. (2003). “Evaluation of a rayleigh-number-based freckle criterion for Pb-Sn alloys and Ni-base superalloys”. *Metallurgical and Materials Transactions A*, 34 (7), pp. 1525–1536. URL: <http://link.springer.com/article/10.1007/s11661-003-0264-0> (cited on pages 7, 63, 64, 73).
- [Rappaz et al. 2003]**
Rappaz, M., Bellet, M., and Deville, M. (2003). *Numerical Modeling in Materials Science and Engineering*. Springer Series in Computational Mathematics. Springer Berlin Heidelberg (cited on pages 7, 21, 26).
- [Rivaux 2011]**
Rivaux, B. (2011). “Simulation 3D éléments finis des macroségrégations en peau induites par déformations thermomécaniques lors de la solidification d'alliages métalliques”. PhD Thesis. École Nationale Supérieure des Mines de Paris. URL: <http://pastel.archives-ouvertes.fr/pastel-00637168> (cited on pages 13, 14, 49, 53).
- [Saad et al. 2015]**
Saad, A., Gandin, C.-A., Bellet, M., Shevchenko, N., and Eckert, S. (2015). “Simulation of Channel Segregation during Directional Solidification of In – 75 wt.% Ga – Qualitative Comparison with In-Situ Observations”. accepted in *Metallurgical Transactions A*, (cited on page 11).

Bibliography

[Sarazin and Hellawell 1992]

Sarazin, J. R. and Hellawell, A. (1992). "Studies of Channel-Plume Convection during Solidification". *Interactive Dynamics of Convection and Solidification*. Ed. by S. H. Davis, H. E. Huppert, U. Müller, and M. G. Worster. NATO ASI Series 219. Springer Netherlands, pp. 143–145. URL: http://link.springer.com/chapter/10.1007/978-94-011-2809-4_22 (cited on pages 8, 11).

[Schneider et al. 1997]

Schneider, M. C., Gu, J. P., Beckermann, C., Boettinger, W. J., and Kattner, U. R. (1997). "Modeling of micro- and macrosegregation and freckle formation in single-crystal nickel-base superalloy directional solidification". *Metallurgical and Materials Transactions A*, 28 (7), pp. 1517–1531. URL: <http://link.springer.com/article/10.1007/s11661-997-0214-3> (cited on pages 11, 63).

[Shah and Moore 1989]

Shah, N. A. and Moore, J. J. (1989). "Effect of thermal conditions and alloying constituents (Ni, Cr) on macrosegregation in continuously cast high-carbon (0.8 Pct), low-alloy steel". *Metallurgical Transactions B*, 20 (6), pp. 893–910. URL: <http://link.springer.com/article/10.1007/BF02670195> (cited on page 8).

[Shevchenko et al. 2013]

Shevchenko, N., Boden, S., Gerbeth, G., and Eckert, S. (2013). "Chimney Formation in Solidifying Ga-25wt pct In Alloys Under the Influence of Thermosolutal Melt Convection". *Metallurgical and Materials Transactions A*, 44 (8), pp. 3797–3808. URL: <http://link.springer.com/article/10.1007/s11661-013-1711-1> (cited on pages 63, 64, 67, 73, 75).

[Süli 2000]

Süli, E. (2000). *Lecture Notes on Finite Element Methods for Partial Differential Equations* (cited on page 24).

[Suzuki and Miyamoto 1973]

Suzuki, K. and Miyamoto, T. (1973). "The Mechanism of Formation of the V Segregation in Steel Ingots". *Tetsu-to-Hagane*, 59 (3), pp. 431–445 (cited on page 8).

[Swaminathan and Voller 1993]

Swaminathan, C. R. and Voller, V. R. (1993). "On The Enthalpy Method". *International Journal of Numerical Methods for Heat & Fluid Flow*, 3 (3), pp. 233–244. URL: <http://www.emeraldinsight.com/journals.htm?articleid=1665561&show=abstract> (cited on page 20).

[TCBIN 2006]

TCBIN (2006). *TCBIN: TC Binary Solutions Database*. Stockholm, SE (cited on page 68).

[TCFE6 2010]

TCFE6 (2010). *TCFE6: a thermodynamic database for different kinds of steels and Fe-based alloys*. Stockholm, SE. URL: <http://goo.gl/qiD3kE> (cited on pages 35, 37, 38).

[Tezduyar et al. 1992]

Tezduyar, T. E., Mittal, S., Ray, S. E., and Shih, R. (1992). "Incompressible flow computations with stabilized bilinear and linear equal-order-interpolation velocity-pressure elements". *Computer Methods in Applied Mechanics and Engineering*, 95 (2), pp. 221–242. URL: <http://www.sciencedirect.com/science/article/pii/0045782592901416> (cited on pages 49, 53).

[Tezduyar and Osawa 2000]

Tezduyar, T. E. and Osawa, Y. (2000). "Finite element stabilization parameters computed from element matrices and vectors". *Computer Methods in Applied Mechanics and Engineering*, 190 (3–4), pp. 411–430. URL: <http://www.sciencedirect.com/science/article/pii/S0045782500002115> (cited on page 53).

[Thuin et al. 2004]

Thuinet, L. and Combeau, H. (2004). "Prediction of macrosegregation during the solidification involving a peritectic transformation for multicomponent steels". *Journal of Materials Science*, 39 (24), pp. 7213–7219. URL: <http://link.springer.com/article/10.1023/B%3AJMSC.0000048734.34597.1e> (cited on page 20).

[Tiller et al. 1953]

Tiller, W. A, Jackson, K. A, Rutter, J. W, and Chalmers, B (1953). "The redistribution of solute atoms during the solidification of metals". *Acta Metallurgica*, 1 (4), pp. 428–437. URL: <http://www.sciencedirect.com/science/article/pii/0001616053901266> (cited on page 6).

[Wanqi and Yaohe 1989]

Wanqi, J. I. E. and Yaohe, Z. (1989). "Formation of hot-top segregation in steel ingot and effect of steel compositions". *Metallurgical Transactions B*, 20 (5), pp. 723–730. URL: <http://link.springer.com/article/10.1007/BF02655930> (cited on page 8).

[WSA 2014]

WSA (2014). *World Steel Association: Statistics archive*. URL: <http://www.worldsteel.org/statistics/statistics-archive.html> (cited on page 12).

[Xu and Li 1991]

Xu, D. and Li, Q. (1991). "Gravity- and Solidification-Shrinkage-Induced Liquid Flow in a Horizontally Solidified Alloy Ingot". *Numerical Heat Transfer, Part A: Applications*, 20 (2), pp. 203–221. URL: <http://dx.doi.org/10.1080/10407789108944817> (cited on page 7).

[Yuan and Lee 2012]

Yuan, L. and Lee, P. D. (2012). "A new mechanism for freckle initiation based on microstructural level simulation". *Acta Materialia*, 60 (12), pp. 4917–4926. URL: <http://www.sciencedirect.com/science/article/pii/S1359645412003205> (cited on page 73).

[Zabaras and Samanta 2004]

Zabaras, N. and Samanta, D. (2004). "A stabilized volume-averaging finite element method for flow in porous media and binary alloy solidification processes". *International Journal for Numerical Methods in Engineering*, 60 (6), pp. 1103–1138. URL: <http://onlinelibrary.wiley.com/doi/10.1002/nme.998/abstract> (cited on page 53).